11-7-2007

Life Cycle of Deccan Trap Magma Chambers: A Crystal Scale Elemental and Strontium Isotopic Investigation

Melroy R. Borges
Florida International University, melroy.borges@gmail.com

FLORIDA INTERNATIONAL UNIVERSITY

Miami, Florida

LIFE CYCLE OF DECCAN TRAP MAGMA CHAMBERS: A CRYSTAL SCALE

ELEMENTAL AND STRONTIUM ISOTOPIC INVESTIGATION

A dissertation submitted in partial fulfillment of the

requirements for the degree of

DOCTOR OF PHILOSOPHY

in

GEOSCIENCES

by

Melroy R. Borges

2008

To: Dean Kenneth Furton
    College of Arts and Sciences

This dissertation, written by Melroy R. Borges, and entitled Life Cycle of Deccan Trap Magma Chambers: A Crystal Scale Elemental and Strontium Isotopic Investigation, having been approved in respect to style and intellectual content, is referred to you for judgment.

We have read this dissertation and recommend that it be approved.

_____
Grenville Draper

_____
Stephen Haggerty

_____
Andrew Macfarlane

_____
Surendra Saxena

_____
Michael Sukop

_____
Gautam Sen, Major Professor

Date of Defense: November 7, 2007

The dissertation of Melroy R. Borges is approved.

_____
Dean Kenneth Furton
College of Arts and Sciences

_____
Dean George Walker
University Graduate School

Florida International University, 2008

ACKNOWLEDGMENTS

I would like to thank my dear friends Jehangir Bhadha, Rahul Chopra and Maya Dodd for their constant friendship, advice and home improvement tips. I would like to thank my parents and sister for all their love and support.

Finally, I owe a deep debt of gratitude to Dr. S. Viladkar and Dr. R. K. Avasia of St. Xavier's College, Mumbai, India, for setting me on an intellectual journey that has culminated in this degree; a journey that I hope to continue in my career as a geoscientist.

ABSTRACT OF THE DISSERTATION

LIFE CYCLE OF DECCAN TRAP MAGMA CHAMBERS: A CRYSTAL SCALE

ELEMENTAL AND STRONTIUM ISOTOPIC INVESTIGATION

by

Melroy R. Borges

Florida International University, 2008

Miami, Florida

Professor Gautam Sen, Major Professor

The Deccan Trap basalts are the remnants of a massive series of lava flows that erupted at the K/T boundary and covered 1-2 million km^2 of west-central India. This eruptive event is of global interest because of its possible link to the major mass extinction event, and there is much debate about the duration of this massive volcanic event. In contrast to isotopic or paleomagnetic dating methods, I explore an alternative approach to determine the lifecycle of the magma chambers that supplied the lavas, and extend the concept to obtain a tighter constraint on Deccan's duration. My method relies on extracting time information from elemental and isotopic diffusion across zone boundaries in individual crystals.

I determined elemental and Sr-isotopic variations across abnormally large (2-5 cm) plagioclase crystals from the Thalghat and Kashele "Giant Plagioclase Basalts" from the lowermost Jawhar and Igatpuri Formations respectively in the thickest Western Ghats section near Mumbai. I also obtained bulk rock major, trace and rare earth element chemistry of each lava flow from the two formations. Thalghat flows contain only 12% zoned crystals, with $^{87}Sr/^{86}Sr$ ratios of 0.7096 in the core and 0.7106 in the rim, separated

by a sharp boundary. In contrast, all Kashele crystals have a wider range of $^{87}Sr/^{86}Sr$ values, with multiple zones. Geochemical modeling of the data suggests that the two types of crystals grew in distinct magmatic environments. Modeling intracrystalline diffusive equilibration between the core and rim of Thalghat crystals led me to obtain a crystal growth rate of $2.03x10^{-10}$ cm/s and a residence time of 780 years for the crystals in the magma chamber(s). Employing some assumptions based on field and geochronologic evidence, I extrapolated this residence time to the entire Western Ghats and obtained an estimate of 25,000 – 35,000 years for the duration of Western Ghats volcanism. This gave an eruptive rate of 30 – 40 km^3/yr, which is much higher than any presently erupting volcano. This result will remain speculative until a similarly detailed analytical-modeling study is performed for the rest of the Western Ghats formations.

TABLE OF CONTENTS

LIST OF FIGURES

CHAPTER I

INTRODUCTION

Large Igneous Provinces

Large volume basaltic eruptions, variously called Flood Basalts, Continental Flood Basalts (CFBs) or Large Igneous Provinces (LIPs), have occurred sporadically on Earth over geologic time. Such eruptions create volcanic provinces consisting of flow upon flow of mostly tholeiitic lava and the erupted volumes of lava are on the order of millions of cubic km with some reaching as much as 40 million cubic km (the Ontong Java Plateau in the western Pacific ocean). LIPs vary greatly in present-day areal extent, but most are thought to have covered areas larger than a million square km when originally erupted (Eldholm and Coffin, 2000; Courtillot and Renne). Many CFBs are found on continent margins, coinciding with the initiation of rifting – for example, the Parana-Etendeka province, the Deccan Province (Courtillot et al., 1999). Others occur in the middle of continents and oceanic basins, like the Ontong Jawa Plateau and the Siberian Traps. Figure 1.1 shows the current location and extent of LIPs on Earth's surface (from Jerram and Widdowson, 2005). In spite of very large volumes of such provinces, the eruptive durations are short, in the order of a few million years, and ~75-90% of the final volume seems to have erupted within a single pulse that did not last more than 1 Ma. (e.g. Courtillot and Renne, 2003). Flood basalt eruptions have been associated with extinction events due to the coincidence of many of the eruptive events with mass extinction or oceanic anoxia events (Rampino and Stothers, 1988; Courtillot and Renne, 2003).

Flood basalts represent the products of magma generation in the mantle by the action of a melting anomaly or "hot spot" that impinges on the lithosphere. Such hot spots are thought to originate by rising mantle plumes, which are temperature and chemical anomalies that form deep in the Earth's mantle and rise towards the surface. The exact origin of mantle plumes is still a point of contention: some authors suggest that they originate from the transition zone between the upper and lower mantle, whereas most others feel that these plumes rise from the D" layer between the mantle and the outer core (Hart et al., 1992; Walker et al., 1995; Brandon et al., 1998). According to the classical model of plume induced flood basalt magmatism, a mantle plume has a head-tail structure, where due to fluid dynamic processes operating on the rising plume, it forms a large mushroom shaped volume that caps the rising jet of material. The "root" of the plume is then the much narrower plume tail, which is presumably anchored to the source region. When the plume impinges upon the lithosphere, the plume head flattens into a pancake shape and causes large scale melting, giving rise to LIPs. Subsequent to LIP formation, the plume tail persists over time and causes smaller scale volcanism (Richards et al., 1989; Campbell and Griffiths, 1990). Movement of the overriding plate during the period of plume tail derived volcanism causes a chain of small volcanoes that in many cases trace the present location of the hot spot to the LIP created in the early stages of hot spot activity (e.g. Richards et al., 1989). In recent years, this model has been challenged, and LIPs are said to be a result of decompression melting due to the onset of small scale convection under cratonic margins aided by rifting (King and Anderson, 1995) The convection results from the juxtaposition of thick, hot cratonic lithosphere with thin, cooler oceanic lithosphere.

The Deccan Trap Basalts

The Large Igneous Province known as the Deccan Traps covers a significant portion of the Indian subcontinent (Figures 1.1 and 1.2). This province has been the subject of much study, owing to the K-T boundary age of the bulk of the lavas (Hofmann et al., 2000), the possible role of the eruptive event in the splitting of the Seychelles microcontinent from India (Devey and Stephens, 1991; Collier et al., 2004), and the effect of the eruption on global ocean geochemistry (Ravizza and Peucker-Ehrenbrink, 2003). In the west-central portion of the Indian Peninsula, the Deccan Traps cover almost the entire state of Maharashtra, of which Mumbai (Bombay) is the capital. A linear structural feature called the Panvel Flexure demarcates the western boundary of the main central portion of the Traps, resulting in a steep escarpment called the Western Ghats (ghat being the local term for a mountain pass). The lavas of the west-central Deccan extending eastward from the ghats at the coast east up to central India are called the Western Ghat lavas. The escarpments allow for spectacular exposures of the lava flows, with mountains showing the typical step-like outline of an eroded stack of lava flows (Figure 1.3), which presumably led to the name "Deccan Trap"; trap or "trapp" being Swedish for step. Because of the well exposed sections in the Western Ghats, this area is the best studied part of the Deccan Lava pile, especially the southern section near the Mahabaleshwar area.

The Deccan Traps today cover around 500,000 square kilometers, forming the Deccan Plateau in India (e.g. Hooper, 1999; Sen, 2001). The pre-erosional volume is estimated at around 1-2 million km^3 which would make the Deccan one of the largest volcanic eruptions on Earth. Dikes and flows studied in Seychelles (Devey and Stephens,

1991) have been related to the Indian Deccan, suggesting that the original flow volume could have been much greater.

Deccan Trap lavas can be divided into three main types of geographic sections: the Western Ghats, the north-west and the north-east section (Figure 1.2). Amongst them the Western Ghats is the type section, as it is the most voluminous section and is composed of tholeiitic flows that are typical of flood basalt provinces (Najafi et al., 1981; Mahoney et al., 1982; Cox and Hawkesworth, 1985; Beane et al., 1986; Sen, 1986; Mahoney, 1988; Hooper, 1999). The north-west section outcrops ~600 km away from the Western Ghats, and is composed of older alkali basalts, picrites and silica-undersaturated alkalic complexes with carbonatite and nephelinite flows and intrusives (e.g. Viladkar, 1981; Gwalani et al., 1993; Simonetti et al., 1995; Mahoney et al., 2000). Whereas the Western Ghats flows are dated at 65 Ma, the flows of the north-west section are older with ~68 Ma ages (Basu et al., 1993). The north-east section has flows that show broad similarity in age and composition with the main Western Ghats lavas (e.g Peng et al., 1998; Mahoney et al., 2000; Melluso et al., 2004). The youngest flows in the Deccan are represented by 62 Ma silicic flows around Bombay (Sheth et al., 2001) and 62 Ma feeder dikes south of the Western Ghats (Widdowson et al., 2000).

Interest in the Deccan acquired a tremendous boost when age dating suggested that the Western Ghats flows were synchronous with the 65 Ma K-T extinction event (Courtillot et al., 1986). The Western Ghat lava pile is nearly 3000 metres thick, exposing stratigraphically older flows near Bombay and Nasik, and the youngest flows near Mahabaleshwar, close to the southern limit of the Deccan. However, ages of most of the Deccan Western Ghats flows are indistinguishable from each other, and suggest a very

4

short duration (<1 Ma) for the eruption of the Western Ghats (Courtillot et al., 1986; Courtillot et al., 1988; Duncan and Pyle, 1988; Gallet et al., 1989; Hofmann et al., 2000; Pande, 2002; Chenet et al., 2007). The synchronicity of the Deccan with the K-T extinction led to a debate over the cause of this extinction event. It had famously been suggested that the extinction was caused by catastrophic climatic disturbance by a meteorite impact (Alvarez et al., 1980). But the temporal coincidence of the Deccan eruption with the event, the short eruptive duration of the Deccan led others to suggest climatic effects of volcanism and volcanic gases as an alternative cause of the K-T extinction. This debate has continued and has not been unequivocally resolved as of today.

Self et al (2006) note that the Deccan eruption would have pumped massive amounts of SO_2 into the atmosphere, while the release of CO_2 was insufficient to affect the climate. Recently, Self et al. (2008) measured S and Cl in Deccan melt inclusions and calculate a yield of 3.5 teragrams (10^{12} gm) of SO_2 and 1 teragram of HCl per cubic km of Deccan lava erupted. Since the Deccan had between 1-2 million km^3 erupted volume, the tremendous amount of poisonous gases released into the atmosphere would have a marked effect on climate and biota. The exact mechanism by which eruptive events would cause extinction is still not well defined, however it should be noted that the climatic effects of volcanism would be of a longer duration than those of a meteorite impact. A study of oceanic sediment cores has shown that the $^{187}Os/^{188}Os$ content of global seawater suffered a gradual change towards mantle-like ratios at around 65 Ma, and this change commenced some time before the impact-related Ir rich layer of the K-T boundary were deposited (Ravizza and Peucker-Ehrenbrink, 2003). The Deccan eruption

therefore did have an impact on global chemistry and could have had the potential to impact global climate. Of course, the shorter the Deccan timescale, the more pronounced would be the climatic effects of the eruption. A 1 Ma timescale of the Deccan means that the average eruptive rate was 1-2 km^3/yr, which is higher than the average 0.4 km^3/yr value of currently erupting Hawaiian lavas at Kilauea (calculated with data from the University of Hawaii's Hawaiian Center for Volcanology website: http://www.soest.hawaii.edu/GG/HCV/kil-hist.html). The 1783 Laki eruption in Iceland had a very high eruption rate of 271 km^3/yr (Thordarson and Self, 1993), although when combined with the 900 AD Eldja eruption, a lower average rate of 0.03 km^3/yr is obtained.

It must be noted that the duration limit of 1 Ma mentioned above for the Deccan Western Ghats activity is not an independently measured limit, i.e. the lowermost flows are not 1 Ma older than the uppermost flows. Most of the age dating on the Deccan was done using the K-Ar or Ar-Ar methods (Courtillot et al., 1986; Duncan and Pyle, 1988; Vandamme et al., 1991; Hofmann et al., 2000; Pande, 2002; Chenet et al., 2007) and this method has an error of ±1 Ma. Re-Os ages on the Deccan (Allegre et al., 1999) also show a 65.6±0.3 Ma age. It has been suggested that the upper formations of the Western Ghats have a younger age of 64.5 Ma (Pande, 2002). However, the true duration of the Deccan could have been orders of magnitude lesser than 1 Ma. A better estimate of duration is needed, in order to provide realistic eruptive rates for the Deccan.

Previous studies (Sen, 2001; Sen et al., 2006) have attempted to apply crystal growth rates to calculating a timescale for Deccan eruption. Sen (2001) singled out the group of Deccan lavas called "Giant Plagioclase Basalts (GPB)", which are evolved lavas

carrying very large (upto 5 cm long) tabular plagioclase phenocrysts (Figure 1.4).

Because of the large size of GPB phenocrysts, Sen (2001) speculated that the giant

plagioclase grew throughout the life cycle of a magma chamber and different zones of the

crystal would carry geochemical signatures of different flows originating from the same

magma chamber. Sen (2001) assumed a crystal growth rate from studies of Hawaiian lava

lakes (Cashman and Marsh, 1988) and calculated a timescale of 3200 years for the

growth of plagioclase crystals in the GPBs. Assuming that this growth time would be

related to the eruption timescale of the formation, Sen (2001) extrapolated the calculated

time to the GPB-bearing formations, and then to the entire Deccan, arriving at a timescale

of just 55,000 years for the Deccan eruption. In a subsequent study, this technique was

refined by using a better estimate of crystal size, and using the Johnson-Mehl-Avrami

equation to model crystal growth times (Sen et al. 2006). This study yielded an estimate

of 22800 years for the Deccan eruptive duration.

The crystal growth technique does have the potential to obtain a tighter constraint

on eruptive timescales. The method outlined by Sen (2001, 2006) is based on some

testable assumptions that need to be verified. For example, the rate of growth of a GPB

crystal is unlikely to be constant, and in particular, such a crystal may have undergone

episodes of partial dissolution of during its life-time. Second, whether a single GPB

crystal represents the entire life cycle of a magma chamber (i.e., formation) needs to be

verified by correlating Sr-isotope ratios within individual zones within the GPB crystal

with phenocryst or whole rock isotopic composition of older lavas from the same

formation. The present study was initiated with these goals in mind.

Crystal Isotope Stratigraphy

In this study I have applied a relatively new technique to the problem of Deccan eruptive duration. Recent advances in mass spectrometry have made it easier to couple a laser to a multi-collector inductively coupled plasma mass spectrometer (MC-ICPMS) in order to measure trace element and isotopic variations on the micron scale in thick petrographic sections. This technique has been applied to the measurement of isotopic ratios of Sr in single plagioclase crystals. With a reasonably sized laser beam (~100 microns), one can sample individual zones within a crystal, thus obtaining a trace elemental or isotopic zoning profile across the crystal. Such a profile would record the changes in magmatic conditions during the growth time of the crystal; much like tree rings or glacial ice layers record earth's climate over time. This technique, dubbed "Crystal Isotope Stratigraphy", has been used mainly in the study of lavas from convergent plate boundaries, many of which contain strongly zoned plagioclase crystals (e.g. Tepley et al., 1997; Zellmer et al., 1999; Tepley et al., 2000; Davidson et al., 2001; Costa et al., 2003; Tepley and Davidson, 2003). In a recent study (Ramos et al., 2005) this technique has been used on plagioclase crystals from another flood basalt terrain, the Columbia River Basalts, to decipher the relationship between plagioclase phenocrysts to the host lava. This study is the only application of such a technique to large basaltic terranes, and the authors have successfully shown that the plagioclase crystals were mostly out of equilibrium with the host lava. They reached this conclusion based on the observation that the $^{87}Sr/^{86}Sr$ composition of plagioclase groundmass of the host lava is not the same as that of the phenocryst cores and in some cases the phenocryst rims. Using diffusive modeling of the rim-core $^{87}Sr/^{86}Sr$ profiles in the phenocrysts, they arrived at a

timescale for the residence time of the phenocryst in the magma that erupted. Such information would not be available by any other method.

I used crystal scale measurements of major, trace elements and Sr isotope ratios to decipher magmatic events recorded by the plagioclase crystals in Deccan lavas. I focus on the Jawhar and Igatpuri Formations of the Kalsubai Subgroup. These formations are capped by GPB flows called the Thalghat GPB and Kashele GPB respectively. The primary objective is to refine the methods of the previous studies to arrive at a timescale of Deccan eruption. The procedure is two-fold. I use the zoning profiles in the phenocrysts to evaluate the relationship of the GPB crystals to the host lava, and evaluate whether the phenocrysts have been in equilibrium with previously erupted lava flows as suggested by Sen (2001). I then use diffusion modeling where applicable to constrain residence timescales of the crystals within the Deccan magmatic system. Diffusion modeling allows for a better constraint on residence times. These residence times are then related to crystal growth times, allowing the calculation of an independent crystal growth rate for the Deccan plagioclase. Hence this study is not dependent on crystal growth rates from Hawaiian lavas, which may not necessarily be applicable to the Deccan system. The calculated crystal growth rate is then used in a similar manner as the previous studies (Sen, 2001; 2006), and a timeframe of eruption of lava is obtained. However the eruption rate depends on what proportion of the lava flows can be related using Sr isotopes to the crystal zones within GPB crystals. Implications for the total Deccan eruptive duration are discussed, along with caveats related to the diffusion modeling.

Apart from crystal scale studies, I have also collected whole rock XRF and trace element data and $^{87}Sr/^{86}Sr$ ratios from the other flows of these two formations to model the mixing processes prevalent in the origin of these lavas.
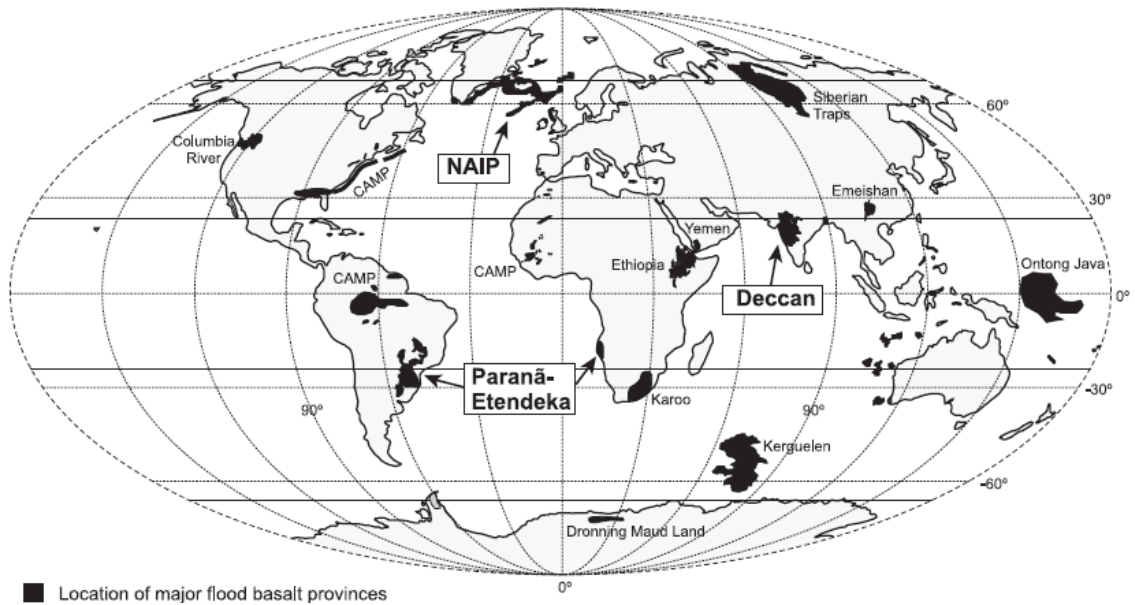
Figure 1.1. Geographical distribution of Large Igneous Provinces on Earth. Figure from Jerram and Widdowson (2005). Large flood basalts are shown as black areas. Such provinces occur on continents as well as ocean basins. Note the location of the Deccan basalt province just south of the Tropic of Cancer 23°N latitude and ~75°E longitude.
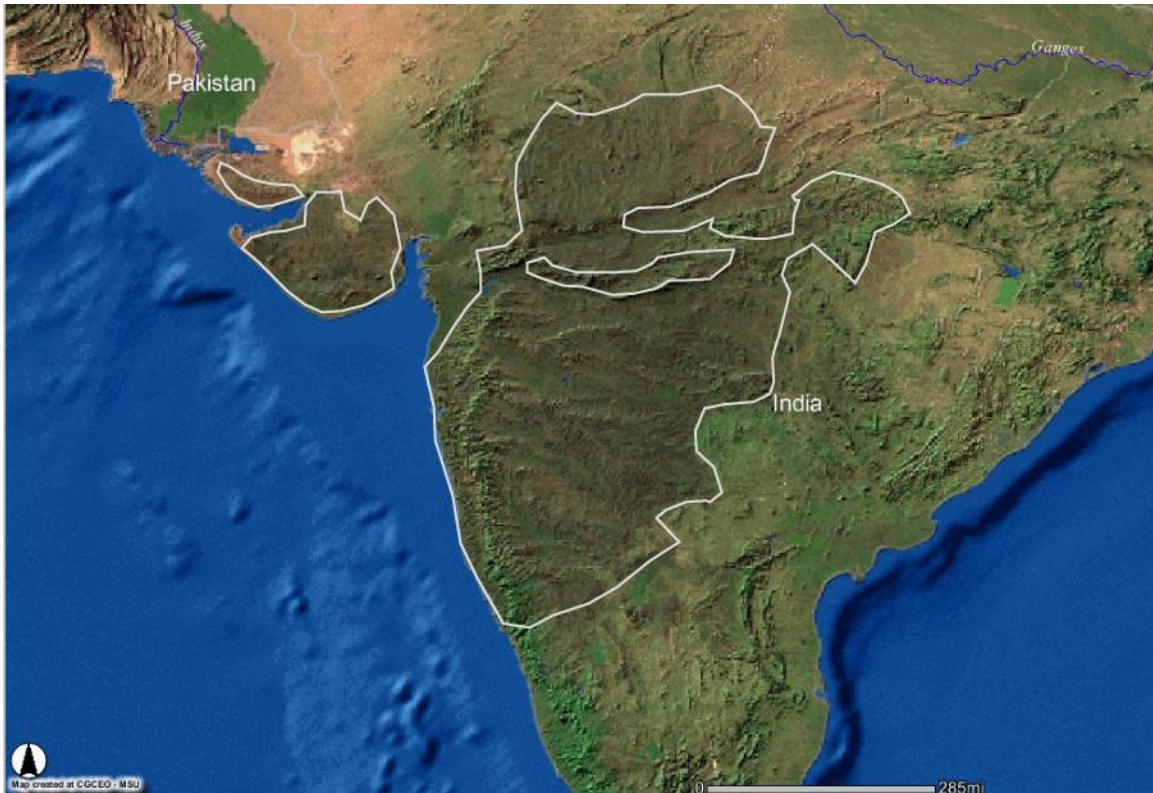
Figure 1.2. Landsat Image of the Indian subcontinent showing the extent of the Deccan Basalts. The Deccan Basalt Province is darker brown in color in this false color Landsat image, and is outlined in white. This image was collected from the website http://www.landsat.org. Scale bar at the bottom of the screen represents a length of 285 miles or 458 km. The flows cover around 500,000 km^2 of land over central India towards the west coast. The area of high topography along the western coast is called the Western Ghats, and it is along this section that the best exposures of Deccan basalts are found.

Figure 1.3. Exposure of Deccan lava flows in the Western Ghats. Note the horizontal disposition of flows stacked one atop the other. This exposure is near the northern part of the Deccan Western Ghats. Photo courtesy of Aditya Paranjpe through Google Earth.

Figure 1.4. Field photograph of a Giant Plagioclase Basalt from the Deccan traps.
The white card is 15 cm long. Large whitish plagioclase crystals are clearly visible in the
rock. Most crystals are visible in cross section, showing an elongate profile. A few
crystals have been sectioned across the broad direction showing an equant to slightly
elongate profile. Many of the grains are 3 cm or more in length, and most are ~2 cm. On
the whole, there is no apparent layering arrangement. Also note that the crystals are rarely
intergrown and occur as isolated "islands".

CHAPTER II

ANALYTICAL METHODS

Sample collection and preparation

Samples were collected for this study during a 5 day field trip in the Bombay –

Nasik – Pune area of Western India in January 2004. This area has the best exposures of

the lower formations of the Deccan Western Ghats section. The two oldest formations

were sampled, viz. the Jawhar and Igatpuri Formations. Flows were identified on field

and correlated between transects based on elevation. Thin-section (4.5 x 2.5 cm) sized

blocks were cut from the fresh parts of the samples, and both thin sections and thick

sections were prepared for electron microprobe (EPMA) analyses and Laser Ablation

ICP-MS (LAICPMS) analyses. Chips were also prepared for whole rock X-Ray

Fluorescence spectrometric (XRF) analyses. In the case of GPB flows, I took care to

avoid large plagioclase crystals in preparation of the rock chips for whole rock analyses.

Polished thin sections were studied under the polarized light microscope and the

Scanning Electron microscope (SEM).

Electron Microscopy

Following regular examination with a petrographic microscope, plagioclase

crystals in individual specimens were studied using a JEOL JSM 5900LV Scanning

Electron Microscope at the Florida Center for Analytical Electron Microscopy (FCAEM)

at FIU. Both back-scattered (BSE) and cathodoluminiscence (CL) imaging was used, as

plagioclase zoning was only visible in CL. The same samples were then analyzed for

major elements using a JEOL 8900 Superprobe at FCAEM. Plagioclase crystals were

analyzed for major elements as well as Mg and Fe. The JEOL 8900 was run at 15kv and a beam current of 20 nA. Count times were 10s for the major elements Si, Al, Ca. Due to the mobility of Na under the beam it was counted for 10s using a high-count spectrometer crystal, and was among the first elements analyzed during a run. K was analyzed for 20s and both Mg and Fe for 60-100 sec. Transects were measured across plagioclase crystals at 2-5 micron intervals to study zoning. The error in An content as measured on a plagioclase standard was always <0.8%.

LA-ICPMS

$^{87}Sr/^{86}Sr$ isotope ratios were measured on plagioclase crystals from the lavas from the Igatpuri and Jawhar formation using a LA-ICPMS housed in the GeoAnalytical Laboratory at Washington State University. Both phenocryst and groundmass plagioclase crystals were analyzed. Samples were cut into thick sections measuring 4.5 x 2.5 cm in width and length and 1-4 mm in thickness. Each sample was sectioned in a way so that large plagioclase crystals were sliced right down the middle of the crystal The sections were ground so that the two larger faces were parallel, and were then polished to a 1μm diamond finish. The samples were cleaned with ethanol during and after polishing. Laser ablation was performed using a NewWave UP213nm Nd-YAG laser (see Figure 2.1). We ablated and analyzed tracks rather than spots, since it allowed us to use a smaller beam size. The tracks were arranged parallel to zone boundaries in the crystals, and perpendicular to the direction of traverse (see images of analyzed crystals in the next chapter).

Prior to isotopic study, the samples were analyzed for trace element concentrations using a ThermoFinnigan Element2 High Resolution (HR) ICPMS (Figure 2.2). Each analysis was done in a single 350 µm pass of a 20 µm wide laser beam. USGS reference materials BCR-2 (Columbia River Basalt) and BIR (Icelandic Basalt) were used as standards. Data reduction was performed using the GLITTER program. Table 2.1 shows the measured composition of BCR-2 collected over a day in comparison to the recommended values for the standard. The measured data is in good agreement with the recommended standard data, and the errors for Sr and Ba were ~ 4 – 5 %.

^{87}Sr/^{86}Sr isotopes were analyzed using the Finnigan Neptune Multi Collector (MC) ICPMS (Figure 2.3). Count times were set at approximately 100 seconds to obtain 100 count cycles per analysis. The laser was set to a spot size of 80 µm. Laser tracks were typically 600 – 700 microns long. Each track was scanned around 10 times, with the first pass of the laser excluded from data collection. A plagioclase crystal from the Imnaha formation of the Columbia River Basalts, with ^{87}Sr/^{86}Sr ratio of 0.70405 was used as a standard. The standard was analyzed at the beginning of the day's analysis and every 2-3 hours thereafter. The standard data for the entire day was used to determine the analytical error, and the values were then corrected using the known standard ratio of 0.70405; which had been previously determined by micro-drilling (Ramos et al. 2004)..
The 100 measurements per data point were checked using an in-house spreadsheet that disregards outliers based on elevated ^{85}Rb/^{88}Sr ratios (also cf. Ramos et al. 2004). Errors on the measured ^{87}Sr/^{86}Sr of the standard varied day by day, but were always less than 0.00010. Typical errors were ~0.00008.

After data collection, CL images were collected once again, which enabled us to correlate the location of the laser troughs with zones in the crystal that were revealed in CL imaging. The distance of tracks from the edge of the crystal was measured from these images using the commercial image processing software Igor Pro, Adobe Photoshop and Adobe Acrobat.

Data Correction

The major or trace element data were did not require additional correction apart from what was done by the instrument. The $^{87}Sr/^{86}Sr$ data were not age corrected. All the analyses were performed on plagioclase, which has low Rb of ~1.2-2 ppm. Rb in groundmass crystals is generally higher, ranging from 1.2-5 ppm. $^{87}Sr/^{86}Sr$ age correction for most of the phenocrysts is around 0.00001, and the highest correction factor for a laser track that crosses a Rb-rich crack is 0.000035, which is smaller than our best standard error of 0.00004. Age correction is therefore not necessary for the measured ratios, and the collected data are can be directly compared to other age-corrected whole rock data from the literature.

Table 2.1. HR-ICPMS analyses of USGS standard BCR2 using the Element2.

Data measured on 15th Feb 2007

Element (ppm)*	^{29}Si	^{43}Ca	^{85}Rb	^{88}Sr	^{89}Y	^{138}Ba	^{139}La	^{140}Ce	^{208}Pb
BCR2-g1	257000.05	53088.65	45.76	354.74	40.41	699.25	26.70	53.68	10.95
BCR2-g2	257000.06	52778.20	46.36	356.98	40.27	696.35	26.31	54.11	10.88
BCR2-g3	257000.06	52853.71	46.23	359.12	40.07	701.87	25.86	53.44	10.69
BCR2-g4	257000.06	47554.04	49.00	325.55	32.02	651.19	22.70	53.48	11.34
BCR2-g5	257000.05	48341.62	49.47	329.86	32.38	652.01	23.08	54.13	11.49
BCR2-g6	257000.06	47726.81	49.04	325.87	32.19	649.44	22.61	53.20	11.25
average	**257000.06**	**50390.51**	**47.64**	**342.02**	**36.22**	**675.02**	**24.54**	**53.67**	**11.10**
% Measured error			**5.50**	**3.55**	**4.82**	**12.18**	**3.93**	**7.90**	**0.70**	**0.31**
Recommended values[#]			48.00	346.00	37.00	683.00	25.00	53.00	11.00
Error in recommended values			2.00	14.00	2.00	28.00	1.00	2.00	2.00

* Elemental species measured in this study; all values given in ppm. Analyses labeled BCR2-g1 to BCR2-g6 are individual analyses performed in two batches during a day-long analytical session. [#]The averaged values for the entire day are compared to recommended values for BCR2 taken from the USGS website. The average measured data compare well with the recommended values, within error. Si concentration was taken from previously measured data, and used to convert raw counts to ppm concentration values.
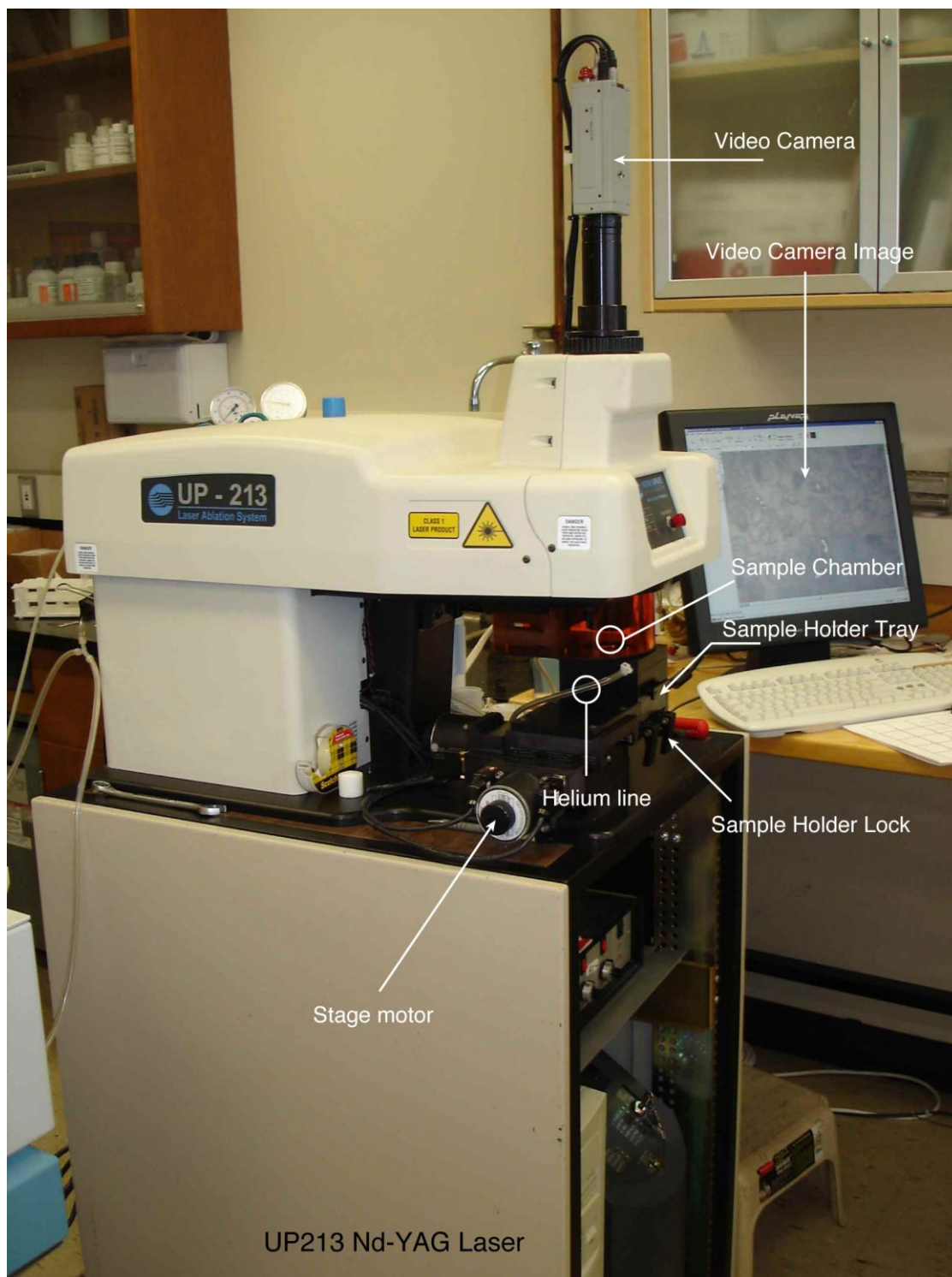
Figure 2.1. Photograph of the UP213 Nd-YAG laser used for Laser Ablation. The sample chamber is continuously flushed by He gas, which also acts as a carrier medium, carrying ablated material into the plasma. Use of He rather than Ar gas helps reduce many of the interferences from Ar compounds. The video camera is attached to a

microscope that provides reflected and transmitted light images of the sample. All stage processes and ablation processes are controlled by the adjacent computer using the New Wave / Mercantek software interface.

Figure 2.2. Photograph of the HR-ICPMS used for trace element analysis. The ThermoFinnigan Element2 was used to measure trace elements in plagioclase. Ablated material from the laser was carried out by a He gas stream and mixed into the Ar gas stream that feeds the plasma. Analysis was controlled by a dedicated computer and the final data was reduced using the Glitter program.
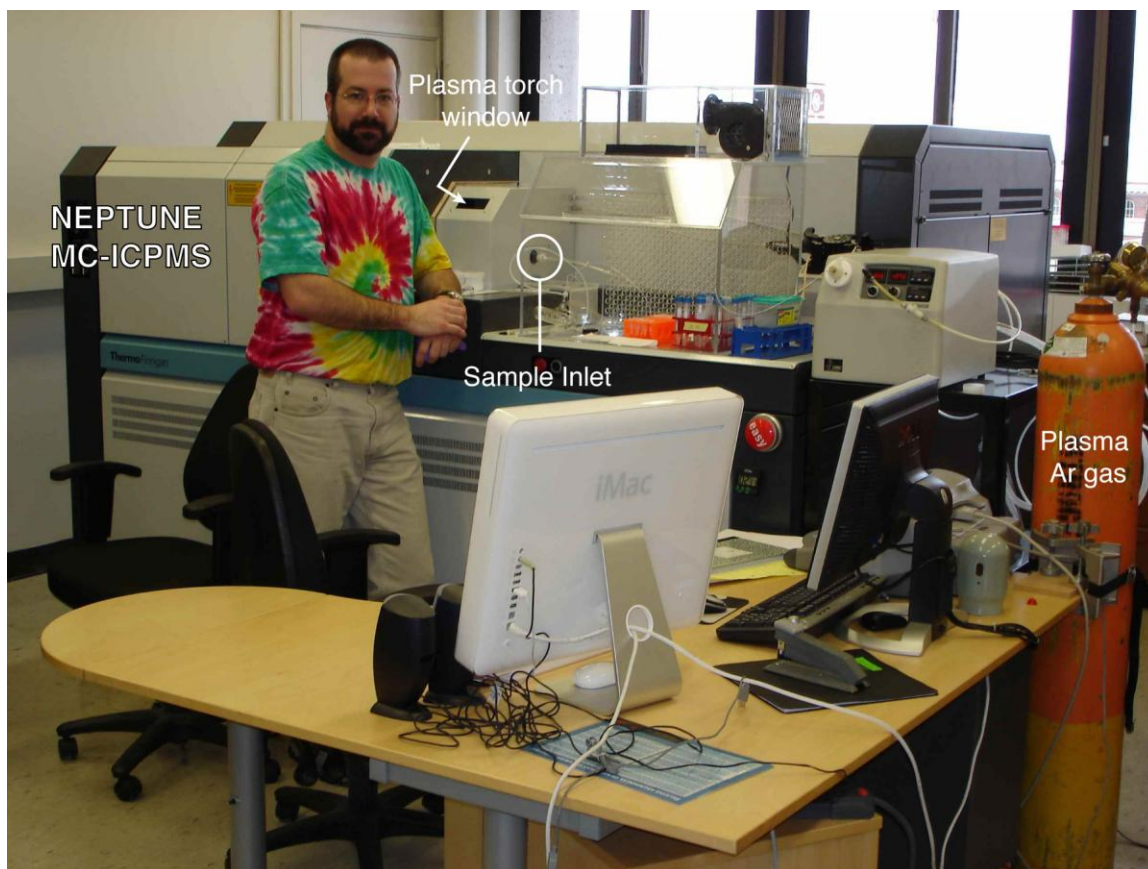
Figure 2.3. Photograph of the MC-ICPMS used for isotopic analyses. The machine is a ThermoFinnigan "Neptune" MC-ICPMS. Sample is fed into the plasma through a He line connected to the Ar gas input for the plasma. All data collection was controlled by a dedicated computer, and reduced using an in-house procedure created by Garret Hart (standing).

CHAPTER III

GEOCHEMISTRY OF THE JAWHAR AND IGATPURI FORMATIONS

Stratigraphy of the Western Ghats

The Western Ghats range represents the type section of Deccan Traps as 2.8 km of lava is exposed here. The Western Ghats lavas have been mapped and studied by numerous workers (e.g. Najafi et al., 1981; Mahoney et al., 1982; Cox and Hawkesworth, 1985; Beane et al., 1986; Lightfoot and Hawkesworth, 1988; Peng et al., 1994; Melluso et al., 2004). The flows are predominantly tholeiitic basalts. Picritic flows (MgO content ≥10%) are rare in the Western Ghats, but common in the Northwestern Deccan (Krishnamurthy and Cox, 1977; Krishnamurthy et al., 2000; Melluso et al., 2006), as are alkali basalts lamprophyres, nephelinites and carbonatites (Viladkar, 1981; Basu et al., 1993; Gwalani et al., 1993; Simonetti et al., 1995; Simonetti et al., 1998). The picritic flows from the Western Ghats have been interpreted to have originated by post-emplacement olivine accumulation on the basis of field evidence, petrography, and geochemistry (Beane et al., 1988).

The Western Ghats lava pile has been divided into three subgroups called Kalsubai, Lonavala, and Wai (oldest to youngest) on the basis of lava geochemistry (Cox and Hawkesworth, 1985; Beane et al., 1986; Beane, 1988; Peng et al., 1994). Each subgroup has in turn been subdivided into formations; and an individual formation consists of numerous flows grouped as members or chemical types (Table 3.1). Although there is some intraformational geochemical variation, those variations are generally small

relative to the differences between formations. In general, the bulk of the lavas are low in MgO (<8%) and are enriched in large-ion lithophile elements (LILE).

Most of the formations shown in Table 3.1 have elevated Sr-isotope ratios (0.709-0.712), except for the Ambenali Formation that has ratios of 0.7038-0.7044. The Ambenali flows have been generally thought to be least contaminated by the continental crust (e.g. Mahoney et al., 1982; Cox and Hawkesworth, 1985; Sen, 2001).The Bushe Formation exhibits the highest Sr isotopic ratios in all of Deccan. Interestingly, Bushe lavas are also higher in Mg# (defined as MgO/MgO+FeO on a molar basis) than most of the Western Ghats lavas. The relationship between the MgO content of flows and $^{87}Sr/^{86}Sr$ ratios is opposite to what would be expected in a normal crustal contamination process. DePaolo (1981) presented the assimilation – fractional crystallization model (AFC) where assimilation of crustal material is accompanied by loss of heat, which then causes crystallization and evolution of the magma body to less primitive compositions. AFC processes therefore result in a negative correlation between MgO and $^{87}Sr/^{86}Sr$ ratios. The Deccan, however, shows "anti-AFC" trends, high MgO flows tend to show evolved $^{87}Sr/^{86}Sr$ ratios. This trend is not limited to the Bushe Formation, but is seen throughout the Deccan (Devey and Cox, 1987).

Based on isotopic compositions, the origin of various Deccan formations have been modeled as mixing between various geochemical reservoirs (Mahoney et al., 1982; Cox and Hawkesworth, 1985; Peng et al., 1994). To explain the younger formations like the Ambenali and Mahabaleshwar, mixing of a Reunion plume member and a depleted MORB member is required. The Bushe Formation, which is the most contaminated, can form by mixing between a Reunion-like end member and a crustal end member. For the

lowermost formations of the Kalsubai Subgroup, three separate end members are required (Peng et al., 1994). The Deccan Traps therefore have a complicated mode of origin.

The Lowermost Deccan Formations

Most early Deccan studies concentrated on the younger formations of the Wai and Lonavla Subgroups that outcrop near the Mahabaleshwar area (Figure 3.1). The older formations outcrop further to the north near the Mumbai – Nasik area. Fewer studies have been done on the oldest Kalsubai Subgroup (Beane et al., 1986; Bodas et al., 1988; Peng et al., 1994). Peng et al. (1994) found that the six lowermost Western Ghats formations that make up the Kalsubai Subgroup have a unique mode of origin, completely separate from the upper formations like the Ambenali and Bushe. These formations define trends in Sr-Nd and Pb-isotopic space that are separate from each other and separate from the trends of the younger formations. The trends appear to diverge from a common composition which has been termed as the "common signature" of the lowermost formations. This common signature has been modeled as a mixture of mantle plume-type material with 40% amphibolite crust (Peng et al., 1994).

Giant Plagioclase Basalts

The lowermost Kalsubai Subgroup is host to a unique class of basaltic flows termed the "Giant Plagioclase Basalts" (GPB) (Hooper et al., 1988). Each of these flows is the last to erupt within a formation and is also chemically the most differentiated member of the formation. The "giant" plagioclase phenocrysts can reach up to 5 cm in length (previous chapter Figure 1.4); and crystals double that size have also been reported (Karmarkar et al., 1972). In general, plagioclase phenocrysts from "regular" lava flows in

the Deccan and other localities are usually less than 1 cm in length; and therefore, the growth of such large crystals and subsequent eruption of the host lava need a special mechanism.

Sen (2001) proposed a model where each formation represents lava extrusions fed by the same magma chamber. He suggested that the "giant phenocrysts" grew in the magma chamber while the magma chamber experienced multiple episodes of input of fresh magma and extrusion of basalts. In his view, the various compositional zones within each "giant" crystal chemically equilibrated with mixed melts, a part of which erupted as lava. Thus, a single crystal recorded the geochemical signature of the older lava flows within the same formation. The GPB flows are then the last product of a magma chamber, which was expelled when the magma chamber's roof collapsed. Using a plagioclase growth rate of 10^{-10} cm/s, Sen (2001) calculated an average time of 3200 years for residence of these crystals in the magma chamber. Recently, Higgins and Chandrasekharam (2007) have carried out a crystal size distribution (CSD) study of the Deccan GPBs. Using a growth rate of 10^{-11} cm/s the authors calculate residence times of 500-1500 years for such crystals. Higgins and Chandrasekharam (2007) postulate that such crystals grew in sub-volcanic magma chambers and plagioclase accumulated by flotation to the top of such chambers. Expulsion of the crystals took place by a new, aphyric magma that infiltrated the chamber and erupted.

Stratigraphy and Geochemistry of the Jawhar and Igatpuri Formations

The Jawhar and Igatpuri Formations were sampled along road cuts and stream valleys in the Mumbai – Nasik – Pune area (Figure 3.1) in January 2004. Bulk-rock

major and trace element data were collected by X-ray Fluorescence Spectrometery

(XRF), and REE and trace elements data by ICPMS. $^{87}Sr/^{86}Sr$ isotopes were measured by

LA-ICPMS on plagioclase crystals from the groundmass the lava flows sampled. In some

samples, the groundmass crystals were not of a sufficient size to allow for sampling with

the laser. In such cases, $^{87}Sr/^{86}Sr$ data were taken from the literature.

Based on flow chemistry and field observations, samples from this study can be

placed in the stratigraphic framework of Beane et al. (1986). In the total alkali – silica

diagram (Figure 3.2), flows from the Jawhar and Igatpuri Formations all plot in the basalt

field. Table 3.2 lists chemical data from the Jawhar and Igatpuri flows analyzed in this

study. Some flows are be directly correlated with flows sampled and named by Beane et

al. (1986) and Beane (1988), based on similarities in Mg#, Sr-isotope composition and

physical descriptions. Variation of Mg# and $^{87}Sr/^{86}Sr$ with elevation is shown in Figure

3.3. In the Jawhar Formation, Mg# tends to decrease with increasing elevation, except for

one high magnesian flow SS21. Igatpuri flows have the opposite tendency, with Mg#

increasing with increasing elevation, only to drop down at the very top of the pile because

of the eruption of the Kashele GPB.

Petrography

Petrographically, most of the flows in the Jawhar and Igatpuri Formations are

aphyric to sparsely porphyritic with exceptions being the GPB flows. The primary

phenocryst phase is plagioclase. Altered olivine phenocrysts are seen in some flows, and

have forsterite content (Fo) ranging from 76 – 62 (Table 3.2). Table 3.2 also shows the

calculated olivine compositions based on olivine-liquid equilibria, and the olivine

phenocrysts appear to be in equilibrium with the host lava. Fayalitic olivine crystals are

seen in the groundmass of these flows having Fo between 30 – 40, probably representing

post eruptive growth in a rapidly cooling lava. In the GPB flows, the large plagioclase

crystals have inclusions of olivine phenocrysts. Thalghat GPB crystals have inclusions of

both types of olivine phenocrysts, showing that these crystals were growing continuously

as magmatic conditions changed. Sample SS26 from the Igatpuri Formation is unique in

having clots of clinopyroxene + plagioclase phenocrysts. Otherwise, clinopyroxene is not

seen as a phenocryst phase. Sample SS27 from the Igatpuri Fm. has large plagioclase

phenocrysts comparable in size to the "giant" plagioclase of the GPB, with the important

difference that the plagioclase crystals occur as sub radiating glomerocrysts, as opposed

to the separate "islands" of plagioclase in the GPB flows. It differs from GPB flows in

other respects too: it is not the most evolved flow in the formation, nor does it occur as a

capping flow.

Major element data are plotted in Figures 3.4 and 3.5. Incompatible element data

and Rare Earth Element (REE) data are plotted in Figures 3.6 and 3.7 respectively. Figure

3.4 is a plot of incompatible major elements P_2O_5 and TiO_2. Lava compositions from the

Jawhar and Igatpuri Formations form a linear trend in incompatible elements, possibly a

result of the tapping of a continuously evolving magma body. The GPB flows have the

highest concentration of incompatible elements. Figure 3.5 compares CaO and MgO

compositions for the flows. Also shown are evolution trends calculated with the

COMAGMAT and MELTS programs (Ghiorso and Sack, 1995; Ariskin, 1999; Ghiorso

et al., 2002). Jawhar and Igatpuri flows could be related to each other by simple

fractionation as Figure 3.4 shows, so the three least evolved flows were used as starting

compositions for the liquid line of descent (LLD) calculations. The Jawhar high MgO

29

flow – the least evolved – does not seem to be parental, as the calculated compositions do not match the other flows. Igatpuri high MgO flows are better candidates as LLDs calculated with these compositions match the measured compositions closely. This result is in agreement with that of Subbarao et al. (1988).

Jawhar flows show a simultaneous decrease in MgO and CaO and show a closer match to the calculated evolution trend. Igatpuri flows appear to fall away from the calculated evolution trends. The evolved Igatpuri flows show abnormally high CaO concentrations, and the high MgO flows show low CaO concentrations. The high CaO in the evolved flows may be a result of plagioclase flotation in the magma chamber, locally increasing the CaO and Al_2O_3 content. The less evolved Igatpuri flows cannot result from fractional crystallization processes, as the compositions do not fall on or close to the calculated evolution lines.

The incompatible element plot (Figure 3.6) shows the lavas of these formations to have an OIB-like pattern with an enrichment of the less incompatible elements and large ion lithophile elements (LILE) like Ba, K, Rb. Sr shows a somewhat abnormal negative spike. Jawhar and Igatpuri flows do not show any differences in patterns, with the minor exception being a slightly wider range in values in the Jawhar flows. The two formations show light REE (LREE) enriched patterns, where once again there is no major difference in the Jawhar and Igatpuri data.

High magnesian flows

Figure 3.3 shows stratigraphic variations of Mg# and $^{87}Sr/^{86}Sr$ in the Igatpuri and Jawhar flows. Most Jawhar flows have low Mg# (<40), but flow SS21 is a high magnesian flow with Mg# 57. A large thickness of the Igatpuri Formation is composed of

high magnesian flows (Mg# > 45). These flows however have higher $^{87}Sr/^{86}Sr$ ratios than the more evolved flows, typical of the "anti-AFC" trend mentioned earlier. Figure 3.8 is a plot of Mg# v/s $^{87}Sr/^{86}Sr$, showing the anti-AFC trend. This trend has been reported for flows from the younger formations (Mahoney et al., 1982; Lightfoot et al., 1990), but to my knowledge this is the first time it has been recognized in the older formations. Figure 3.8 shows this "anti-AFC" trend and shows that the compositions of the magnesian flows of the Igatpuri Formation form a linear trend in Mg# - Sr-isotope space with high and low Mg# flows from the Jawhar Formation as end members.

Comparison with previous studies

Lava compositions measured in this study have been correlated with those of Beane et al. (1986, 1988) in Table 3.2. In Figure 3.4 and 3.5, data from this study are compared to those of Bodas et al (1988), and the two datasets show good agreement. Figure 3.9 compares TiO2 and Zr variations in the GPB flows from the lowermost formations. Hooper et al. (1988) separate GPB flows into separate fields in this plot, allowing them to be easily distinguished from each other. Data from this study fall within the fields of Thalghat and Kashele GPB.
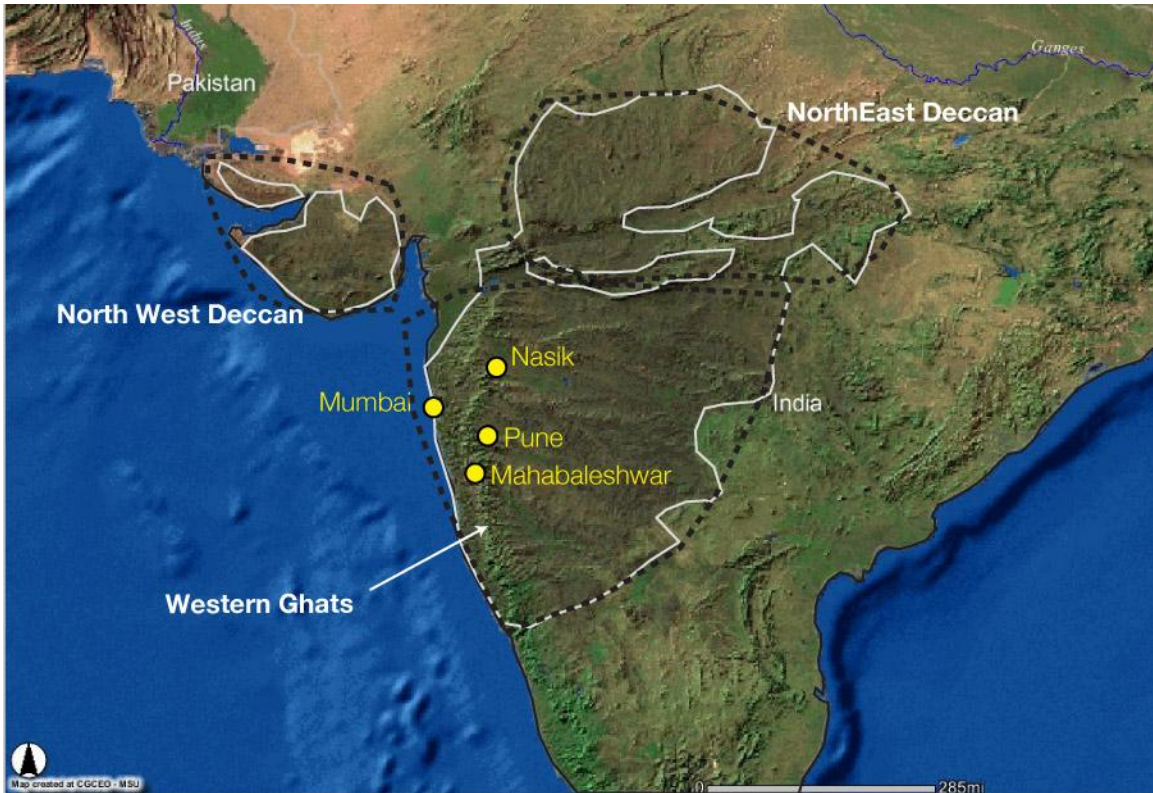
Figure 3.1. The three spatial subdivisions of the Deccan lavas. Landsat image showing the spatial extent of the Deccan (darker brown and outlined in white). The three subdivisions are demarcated by black dotted lines. Also shown in yellow are some cities in the area. For this study, samples were collected from the Mumbai – Nasik – Pune area. The well studied Ambenali and Mahabaleshwar Formations outcrop near the town of Mahabaleshwar. The Western Ghat lavas and the North-East Deccan lavas are contemporaneous in age, while the North-West Deccan has some flows that are older with ages of ~68 Ma.

Table 3.1. Stratigraphy of the Deccan Western Ghats section.

Subgroup	Formation	Member	Mg#	$^{87}Sr/^{86}Sr$	TiO_2	Ba/Zr	Zr/Nb
Wai	Desur (~100 m)		48	0.7072 - 0.708	1.6 - 1.9	1.2	11.4
	Panhala (>175 m)		52	0.7046 - 0.7055	1.6 - 2.3	0.5	14.8
	Mahabaleshwar (280 m)		47	0.704 - 0.7055	2.5 - 4.3	0.5	11.4
	Ambenali (500 m)	Ambenali CT	49	0.7038 - 0.7044	1.9 - 3.1	0.3	14.4
	Poladpur (375 m)	Upper	52	0.7061 - 0.7083	1.8 - 2.3	0.4	12.7
		Lower	56	0.7053 - 0.711	1.5 - 2	0.7	14
		Sambarkada	43	-	2.2 - 2.3	0.9	12.6
		Valvhan	42	0.7068	2.5 - 2.6	0.9	12.3
		Ambavne	45	-	2 - 2.1	0.4	14
Lonavla	Bushe (325 m)	Pingalvadi	61	-	1.1 - 1.2	0.8	17.2
		BusheCT	55	0.713 - 0.72	1 - 1.3	1.1	15.3
		Shingi Hill	49	0.718	1.3 - 1.4	2	16.2
		Hari	46	0.7078 - 0.7079	2 - 2.1	1	12.9
		Karla Picrite	68	0.7147	1.1 - 1.2	0.8	19.7
		Bhaja	58	0.712	1.3 - 1.5	0.6	18.2
	Khandala (140 m)	Rajmachi	44	0.7102	2.1 - 2.5	1.2	14.6
		Khandala Phyric CT	41	-	2.4 - 2.8	1.3	13.6
		KA3	49	0.7107	1.7	3.1	12.9
		Madh	58	-	1.6	2.8	14
		Boyhare	63	0.7102	1.2 - 1.3	2.1	13.7
		KA2	57	0.7124	1.2	3.9	13.5
		Khandala Phyric CT	41	0.7077	2.5 - 2.8	1.3	13.6
		KA1	61	0.7094	1 - 1.1	1.8	15.4
		Dhak Dongar	40	0.7071 - 0.7072	2.9 - 3.1	1	13.1
		KCG	48	0.7098	1.4 - 1.6	1.5	18.7
		Monkey Hill GPB	41	0.7073	3.1 - 3.4	1.1	12.2
		Giravalli GPB	45	0.7068 - 0.7074	2.8 - 3.1	0.8	12.1

Part (a)

33

Subgroup	Formation	Member		Mg#	$^{87}Sr/^{86}Sr$	TiO$_2$	Ba/Zr	Zr/Nb
Kalsubai	Bhimashankar (140m)	Bhimashankar CT		47	0.7067 - 0.7076	1.9 - 2.6	0.8	11.7
		Manchar GPB		42	-	2.9 - 3.1	0.5	13.2
	Thakurvadi (650 m)	Thakurvadi CT		58	0.7073 - 0.708	1.8 - 2.2	0.6	12
		Water Pipe Member		59	0.7099 - 0.7112	1.4 - 1.6	1.5	12.3
		Water Pipe Member		71	-	1 - 1.1	1.3	12
		Paten Basalt		58	-	1	1.3	15.2
		Thakurvadi CT		58	0.7067 - 0.707	1.8 - 2.2	0.8	12.4
		Ashane		62	0.7068	2 - 2.1	1.2	9.6
		Thakurvadi CT		58	0.708 - 0.7084	1.8 - 2.2	0.8	11.6
		Jammu	U	34	0.7112	2.7	1.6	9.8
		Patti	M	46	0.7099	2.2 - 2.3	1.5	8.4
		Member	L	56	0.7066 - 0.7067	1.7 - 2	1.1	11.2
	Neral (100 m)	Tunnel Five GPB		36	0.7082 - 0.7083	3.3 - 3.5	1	10.8
		Tembre Basalt		43	-	2.8 - 3	1.1	10.6
		Neral CT		62	0.7062 - 0.7073	1.5 - 1.7	1.2	12.3
		Ambivali Picrite		67	0.7104	1.4 - 1.5	1.7	18.6
	Igatpuri - Jawhar (>700 m)	Kashele GPB		40	0.7102 - 0.7122	2.6 - 3.1	1.1	11.5
		Mg rich Igatpuri		59	-	1.4 - 1.9	1	13.3
		lgatpuri Phyric		49	0.7107 - 0.7124	1.9 - 2.2	1.1	14.3
		Thalghat GPB		36	0.7108	3.6	0.9	10.7
		HFS-Poor Jawhar		51	-	1.3 - 1.6	1.5	13
		Plag. Phynic		38	0.7085	3	1	11.7
		Mg-Rich Jawhar		59	0.7128	1.4 - 1.9	1	12.7
		Kasara Phyric		39	0.7091	2.8 - 3	1	10.8

Part (b)

Part (a) shows chemical characteristics of flows from the younger Wai and Lonavla
Subgroups, while Part (b) shows chemical variations among flows belonging to the oldest

Kalsubai Subgroup. Table taken from Peng et al., (1994), data from Beane et al., (1986) and Peng et al., (1994). Divisions of subgroups into formations are shown along with the thickness of each formation in meters. Major chemical types (CT) and flow members within each formation are shown in column 3. There is wide variation in chemistry among flows, but most of them are tholeiitic and evolved with Mg# ~40 (Mg# = $MgO/MgO+Fe^{2+}O$). A few high Mg# flows are interspersed at various elevations within the lava pile. Flows in a single formation can have a range of chemical and isotopic compositions. The notable exceptions are the Ambenali, Mahabaleshwar and Bushe Formations, having flows with fairly limited compositional ranges. Most flows have slightly to highly elevated Sr-isotopic ratios, which at first order is a result of crustal contamination. The Ambenali Formation is the only formation showing little to no sign of such contamination, having Sr-isotope ratios close to bulk earth values. Part (b) shows the lowermost formations, with the capping GPB members. Note that in some cases the GPB flows have been included in the formations that overlie them rather than the formations that underlie them. Peng et al., (1994) also combine the Igatpuri and Jawhar into a single formation.
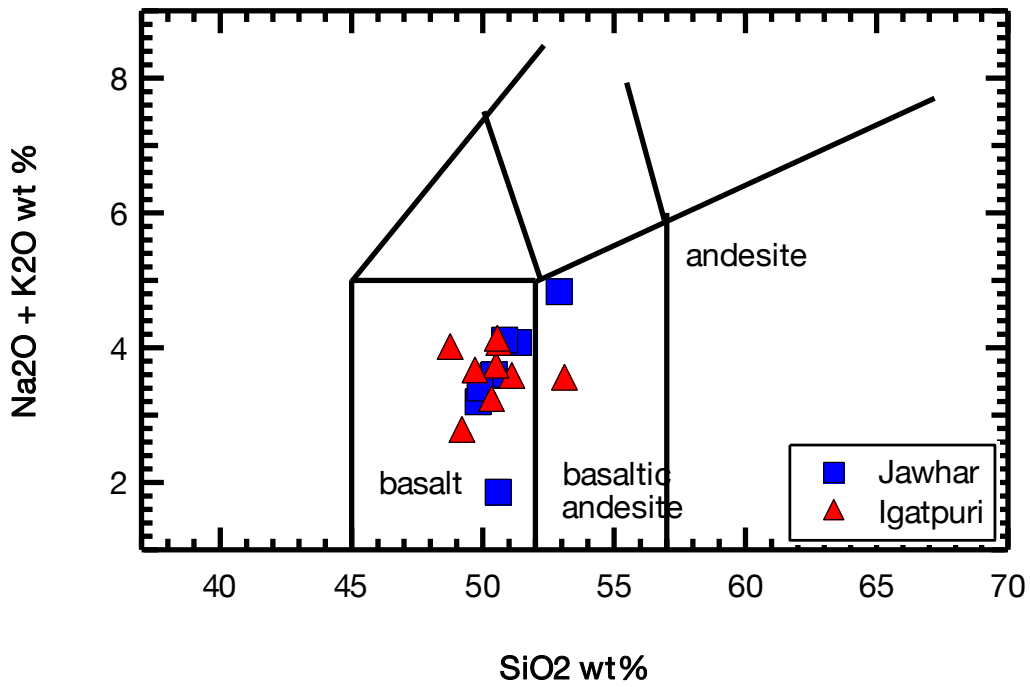
Figure 3.2. Le Maitre classification of lava flows from the Jawhar and Igatpuri Formations. Rocks from the oldest Jawhar Formation are plotted as squares and those from the Igatpuri Formation are plotted as triangles. All of the samples plot in the basaltic field. The two samples within the basaltic andesite field have suffered alteration.

Table 3.2. Geochemistry of Jawhar and Igatpuri Formations.

Formation	Member/Flow (Beane 1986)	Sample names	Elev (m)	Mg# WR	Fo Ol gmass	Fo Ol Pheno	Calc Ol	An% gmass	An% pheno	$^{87}Sr/^{86}Sr$ gmass plag
Igatpuri	Kashele GPB	SS11 SS16 SS14* SS13*	697 691 672 705	32 36 33 34			61 65 62 63	54	60 – 61	0.71061(27) 0.71070(18) NA NA
		SS211	683	53		70, 76	79	76.93	72 – 75	0.71174(12)
	Mg-rich Igatpuri	SS 29	616	53			79			NA
		SS28	535	48	46	72C, 66R	75	54.48	61 – 62	0.71103(11)
	Igatpuri Phyric	SS27	505	41		70	70	57.17	62 – 63	0.71041(16)
		SS26	481	39			68	57.06	61.8	0.71049(16)
Jawhar	Thalghat GPB	SS25 SS23 SS7*	480 423 408	34 36 37	32.4-33.7 29.2-42.1	$62^R – 67^C$ $37^R – 49^R$	63 65 66	57 57	60 60	0.71094(13) 0.71060(13) NA
	HFS-poor Jawhar									
	Plag Phyric	SS22	391	38	37-42.7		67	61	61	0.70891(15)
	Mg-rich Jawhar	SS21	377	57			81	67		0.7129†
	Kasara Phyric	SS5	360	40	32.5-35		69	61.7	67	0.70889(22)
		SS3,SS2	342	36			65	56.6	63	0.70907(12)

(continued)

† data from Beane et al. (1986)   * altered samples Elev = elevation, gmass = groundmass, pheno = phenocryst, plag = plagioclase

Mg# = 100*MgO/(Mgo+FeO); MgO and FeO counted on a molar basis, all Fe taken as Fe^{2+}.

C, R core and rim of olivine phenocryst

[R] Fo of olivine enclosed in rims of plagioclase phenocrysts

[C] Fo of olivine enclosed in cores of plagioclase phenocrysts

Calc Ol : Cacluated olivine compositions in equilibrium with the Mg# of the matrix. Based on an olivine - liquid (Fe/Mg) Kd of 0.3.

The table shows detailed geochemistry of flows from the Lowermost formations of the Western Ghats, analysed in this study. The last column shows the $^{87}Sr/^{86}Sr$ error in parentheses, corresponding to the last two digits. Olivine compositions were measured only in samples that had fresh olivine phenocrysts. Flows sampled in this study have been correlated to those named by Beane et al. (1986) and Beane (1988). Variations in Mg# and $^{87}Sr/^{86}Sr$ are plotted with respect to elevation in Figure 3.
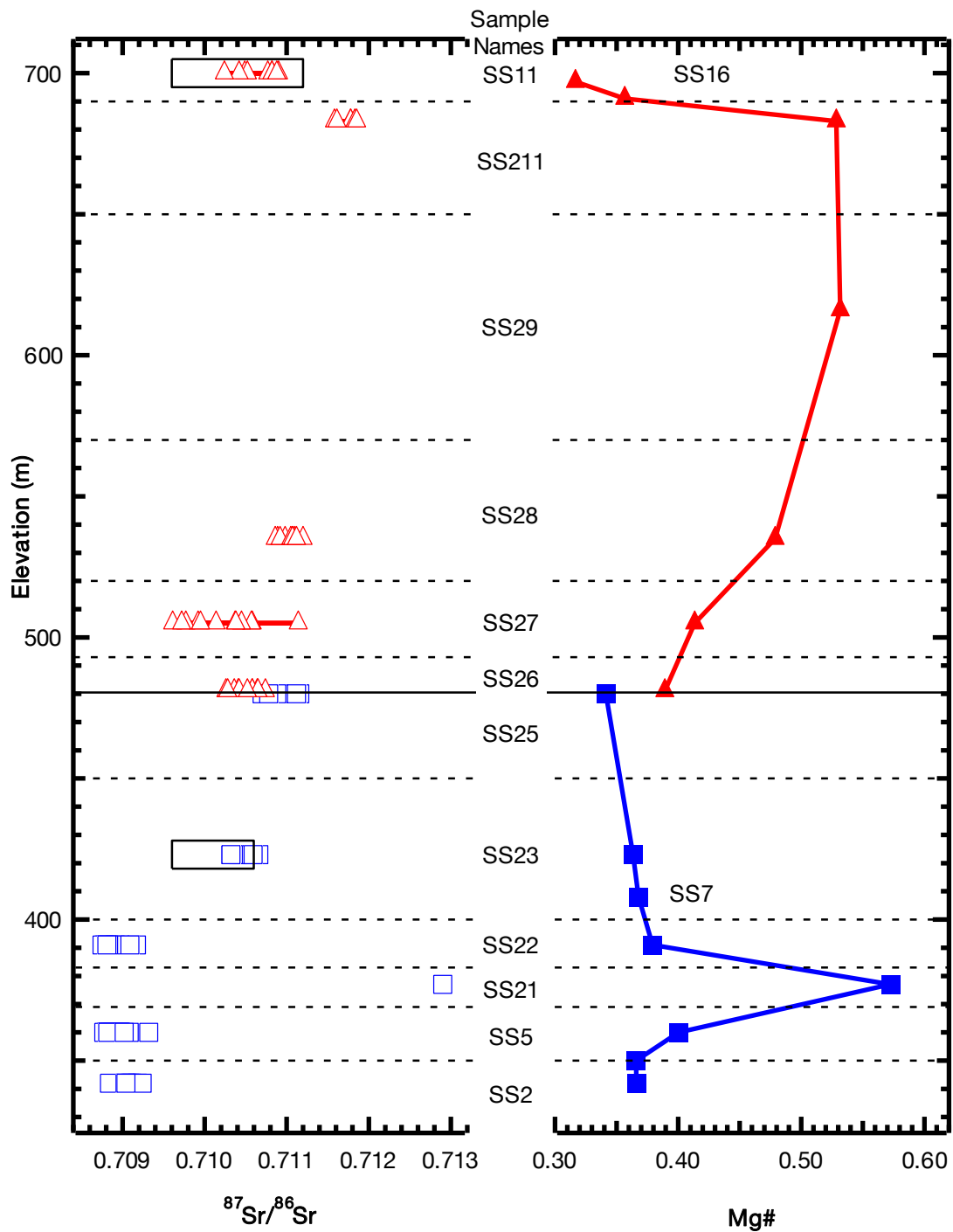
Figure 3.3 Stratigraphic variation of Mg# and $^{87}Sr/^{86}Sr$ in the Jawhar and Igatpuri Formations. Jawhar flows are denoted by blue squares and Igatpuri data by red triangles. Dotted horizontal lines are inferred flow boundaries, and the solid line is an observed flow boundary, which also separates the Igatpuri and Jawhar Formations. Sr- isotope values presented on the left are the range of measured groundmass values; except for

SS27, which is the range of phenocryst values. Black boxes outline the range of giant plagioclase phenocryst values. Some altered samples, which were not analyzed for Sr isotopes, have been omitted for clarity.
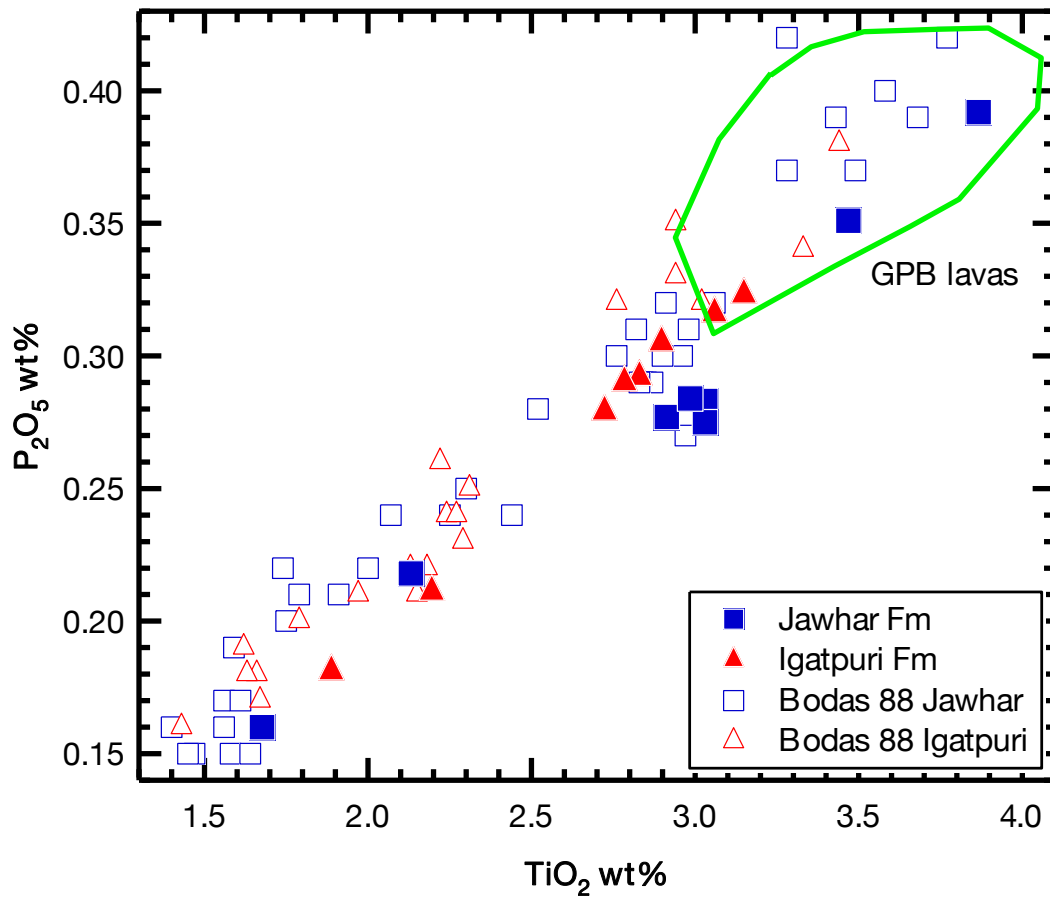
Figure 3.4. P_2O_5 vs TiO_2 variations in lavas from the Jawhar and Igatpuri Formations. Data from this study are shown as solid symbols, and data from the previous Bodas et al. (1988) study are plotted as open symbols (squares for Jawhar and triangles for Igatpuri). Incompatible element oxides TiO_2 and P_2O_5 show a positive correlation, with the more magnesian flows plotting at the lower range, and the evolved flows plotting at the upper range. This trend could result from progressively increasing incompatible element concentrations by fractional crystallization. The most evolved melts that have the highest concentrations of incompatible elements are the GPB flows (circled in green).
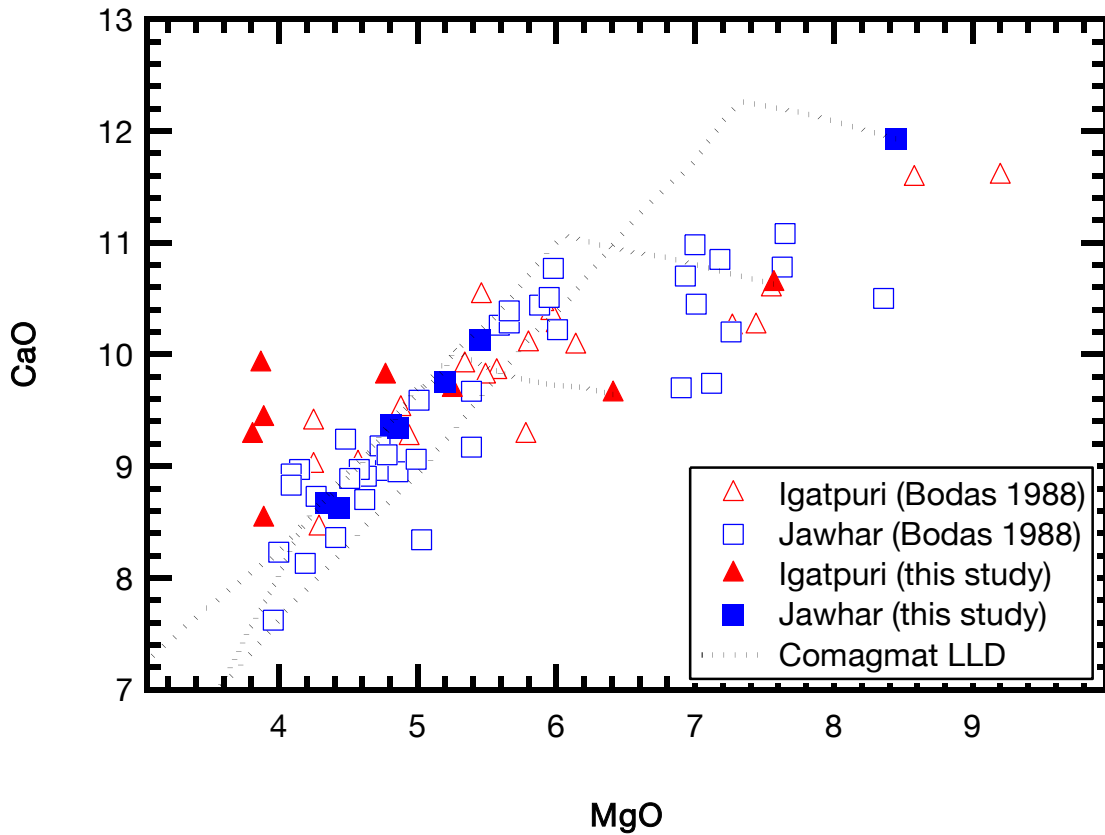
Figure 3.5. CaO vs MgO variations in lavas from the Jawhar and Igatpuri Formations. Solid symbols are data from this study, open symbols are data from Bodas et al. (1988). The dotted lines are liquid lines of descent calculated using the COMAGMAT and MELTS software. Three starting compositions are considered, and all three are flows with higher MgO content (>6%). The two Igatpuri starting compositions are better suited as parental compositions to the flows from the two formations. The selected high MgO flows do not themselves fall on calculated LLD lines, and so are not related to each other by fractionation.
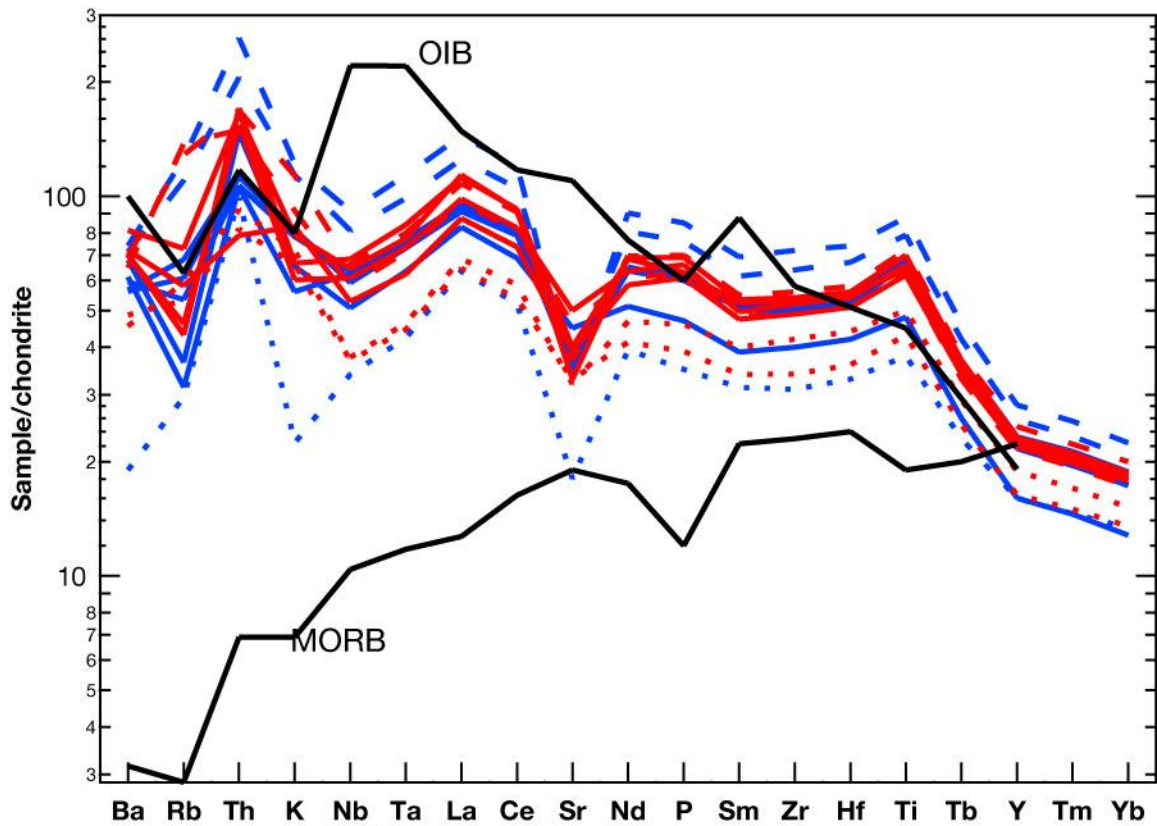
Figure 3.6. Incompatible element patterns in Jawhar and Igatpuri Formation lavas. Chondrite normalized trace element data for the Jawhar and Igatpuri Formations are shown in blue and red respectively. Dotted lines are the high MgO flows (MgO .> 6%) while dashed lines are the evolved flows which in this case are the GPB flows. Lines for n-MORB and OIB are shown in black for comparison. The patterns mimic OIB patterns for the most part, apart from depletion in Sr and Nb. (Chondrite data, MORB and OIB compositions from Sun, 1980; Sun and McDonough, 1989; McDonough and Sun, 1995).
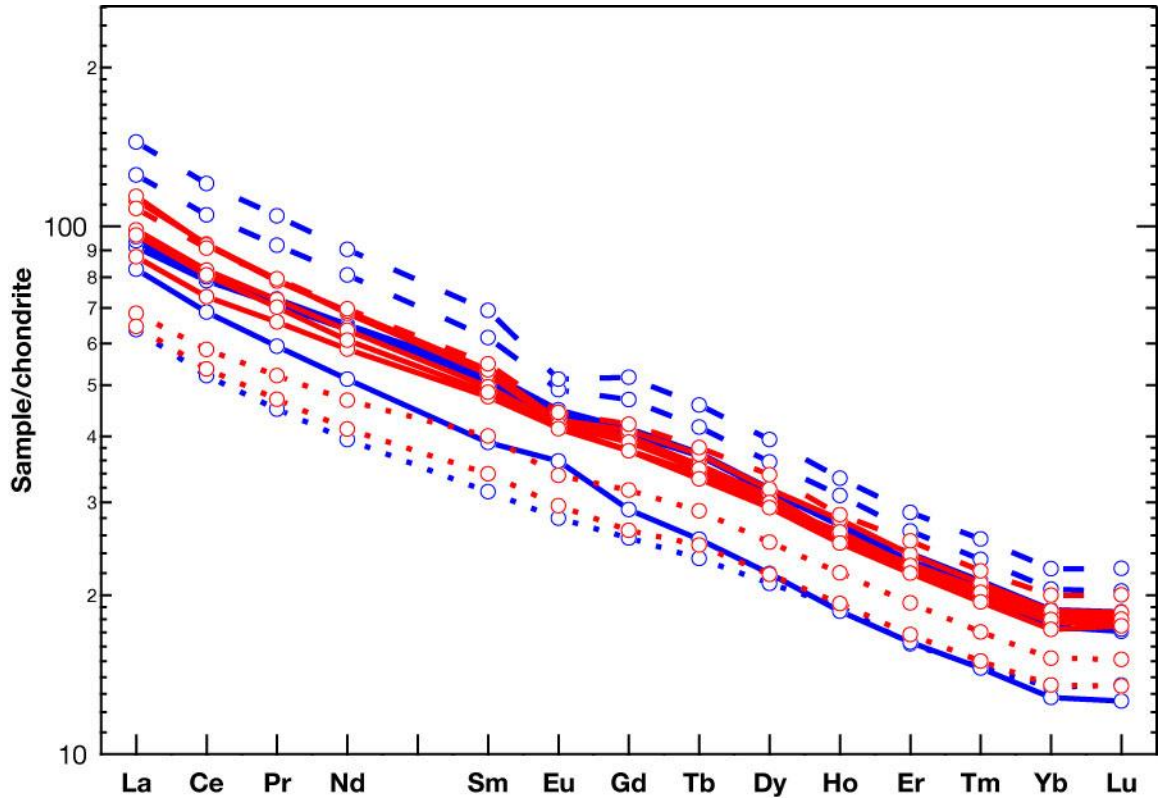
Figure 3.7. Chondrite normalized REE patterns for the Igatpuri and Jawhar flows. Igatpuri flows are shown in red and Jawhar flows in blue. All samples have LREE enriched profiles. Dotted lines are high-MgO flows while dashed lines are the most evolved flows in the two formations, which in this case are the GPB flows. The slight negative Eu anomaly in the GPB flows are a result of Eu partitioning into plagioclase crystals. The patterns are all parallel to each other; the source for the two formations appears to be similar. The single blue line that cuts across the other trends and shows higher LREE/HREE is the highly altered SS7 sample.
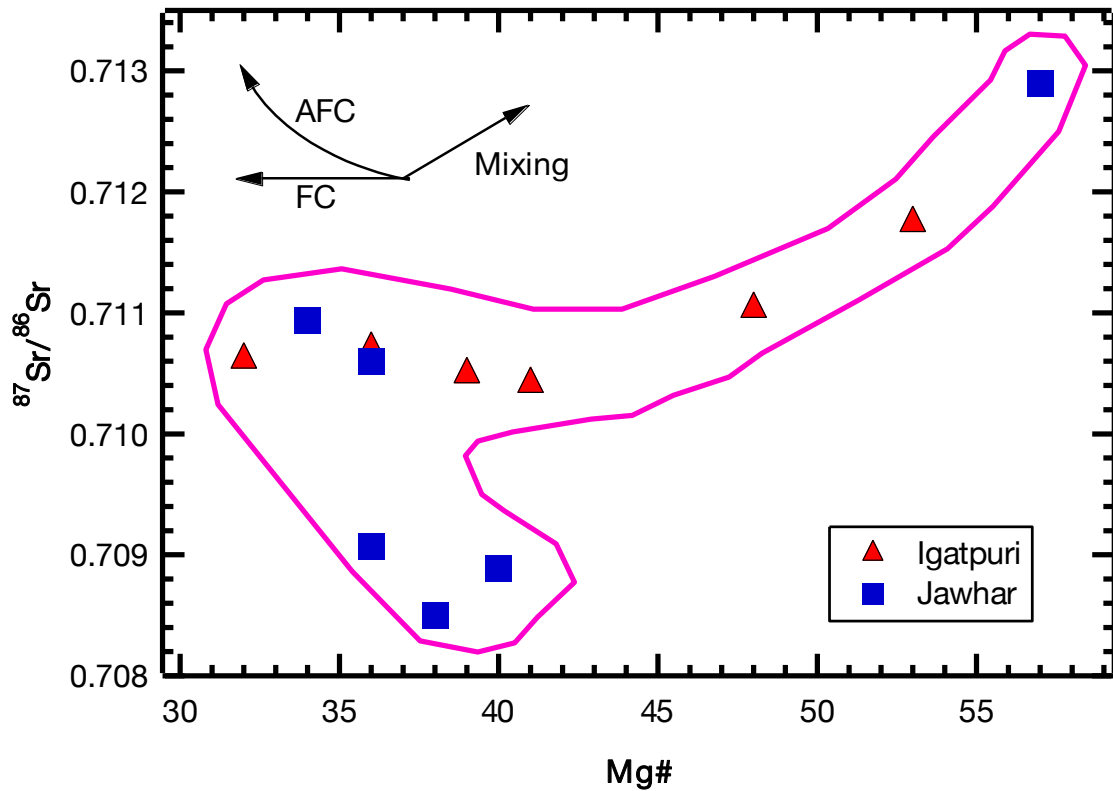
Figure 3.8. $^{87}Sr/^{86}Sr$ vs Mg# variations in lavas from the Jawhar and Igatpuri Formations. Jawhar and Igatpuri compositions (squares and triangles respectively) fall on a linear trend with Jawhar flows of Mg# 40 and 57 as end members. Such a trend is opposite to the expected AFC trend, which is shown by the labeled arrow in the upper left corner of the figure. The low Mg# flows appear to follow the AFC trend: as Mg# decreases from 40 to 32, $^{87}Sr/^{86}Sr$ increases. The intermediate flows of the Igatpuri and Jawhar with near constant $^{87}Sr/^{86}Sr$ of ~0.7108 appear to be related by simple fractional crystallization where a decrease in Mg# is not accompanied by change in $^{87}Sr/^{86}Sr$.
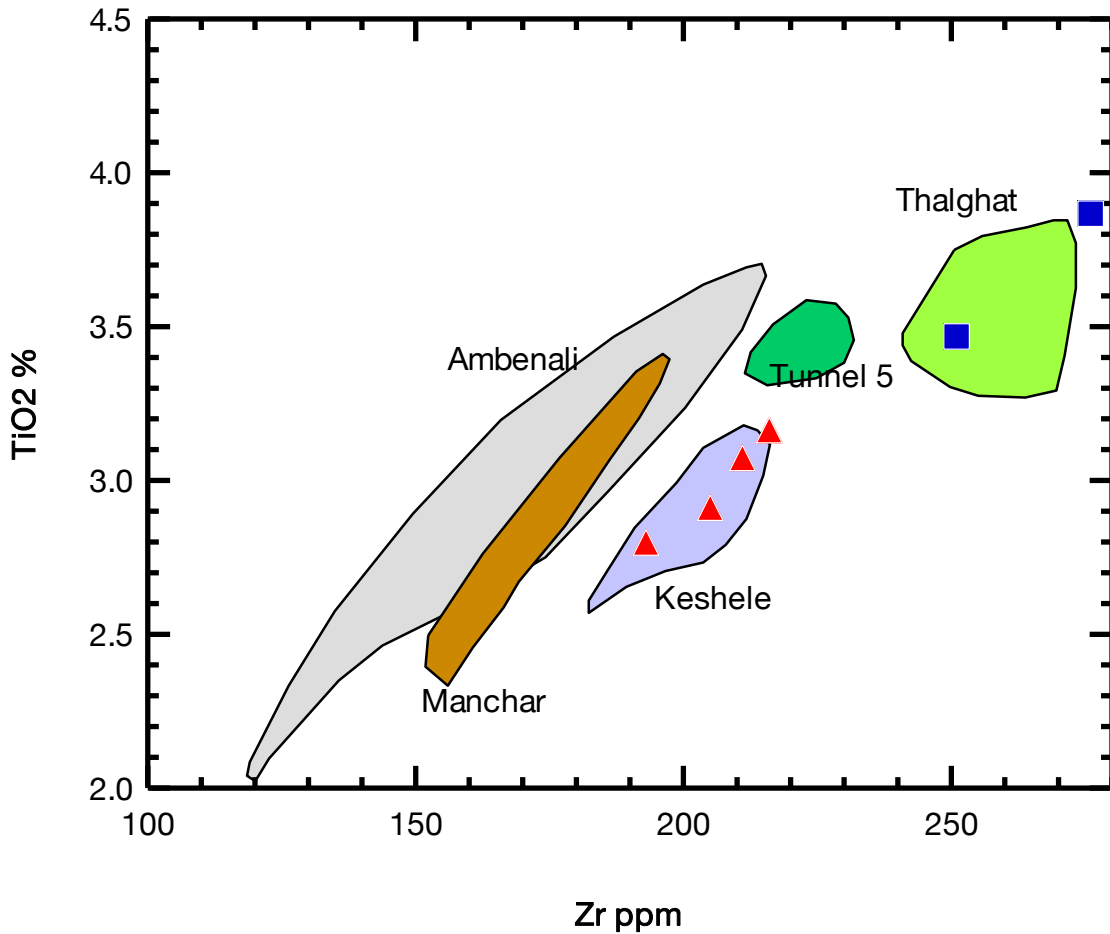
Figure 3.9. TiO₂ and Zr variations in GPB lavas from the Deccan Traps. The different GPB flows from the Kalsubai Subgroup of the Western Ghats are plotted as fields. Flows separate easily in incompatible element space. The field of Ambenali flows is shows for comparison. Kashele and Thalghat data from this study are plotted as squares and triangles respectively. Fields are from Hooper et al. (1988). Data from the present study correlate well with data from Hooper et al. (1988).

CHAPTER IV

OBSERVATIONS ON ZONING IN PLAGIOCLASE FROM THE THALGHAT AND KASHELE GPB FLOWS.

The giant plagioclase crystals from the Jawhar and Igatpuri Formations were the main focus of this study. Crystals were sectioned and studied for compositional zoning characteristics. The GPB crystals were first analyzed for zoning with plane polarized and cross polarized microscopy. Plagioclase crystals from both Thalghat and Kashele Formations show faint but pervasive oscillatory zoning, with the more typical normal or reverse core-rim compositional zoning absent. The only exception was one single crystal from the Kashele GPB that had a clearly visible "mantle" of higher anorthite (An) content than the core and rim. The variation due to oscillatory zoning is not more than 2-3% in An content (Figure 4.1).

Under back-scattered electron (BSE) imaging, the crystals appear completely homogeneous. The intragrain 2-3% variation in the mean atomic number across individual crystals is not strong enough to be picked up by BSE imaging; however, a ~200 μm outermost rim forms a darker border around the crystals. Examination of this zoning with the electron microprobe shows that this rim is drastically lower in An-content and higher in K and Fe (Figure 4.1). This outermost rim most likely grew during rapid cooling of the host lava.

In contrast to the weakly visible optical zoning, cathodoluminescence (CL) imaging revealed conspicuous zoning features.. In the Thalghat GPB, some plagioclase crystals appear to have a well defined central core about 1/3rd the length and width of the

47

crystal (Figure 4.2). In Kashele GPB crystals, the zoning is different and all crystals show a number of well developed zones (Figure 4.3). Oscillatory zoning can also be observed in CL images, although it is much lower in intensity than the core-rim zoning. In Figure 4.9, both types of zoning are exhibited by the Kashele crystal SS11_tr1.

Cathodoluminescence in plagioclase is activated by a number of ions. CL can be caused by variation in An-content, which is why the oscillatory zoning is seen in CL but not in BSE images. Mn^{2+}, Ti^{3+} and Fe^{3+} can also activate CL in plagioclase (Mora and Ramseyer, 1992; Goetze et al., 1999; Lee et al., 2007). Fe^{3+} causes plagioclase to fluoresce in the red spectrum (~690 nm wavelength) and Ti^{3+} causes emission in the blue spectrum (~450 nm) (Goetze et al., 1999; Lee et al., 2007). Since CL images were taken on an electron microprobe rather than an optical CL microscope, the exact cause of the major core-rim zoning cannot be determined. However, it is possible that the zoning revealed by CL imaging reflects a change in Fe^{3+} or Ti^{3+}, which in turn may reflect a change in oxidation states of the surrounding melt from which the crystal grew. One could further speculate that this rapid local changes in the redox state of the melt occurred as a result of mixing of differentially oxidized melts, or perhaps due to an increase in the dissolved water content of the magma.

Plagioclase phenocrysts and plagioclase groundmass crystals in the two formations were analyzed for major elements, trace elements (Sr, Ba, Mg, Fe, K) and $^{87}Sr/^{86}Sr$ ratios. All analyses were performed along transects that cut across zones of crystals as revealed by CL imaging, shown in Figure 4.2. . As stated before in the Methods section, $^{87}Sr/^{86}Sr$ data from this study do not need age-correction and can be compared with whole-rock age-corrected data extracted from the published literature.

Zoning systematics in the Thalghat and Kashele GPB phenocrysts are very different, pointing to varying magmatic processes involved during crystal growth. There are some commonalities between the crystals, namely a weak to nonexistent major element zoning, even when zoning is clearly visible in CL images (Figures 4.5 and 4.6). These features are discussed below.

A note on nomenclature used

In this chapter and in later chapters, compositional zones in a crystal are named as follows. The innermost zone is termed as the core. It is around 1 mm - 1 cm in length in the crystals studied. In some crystals, the core may not be observed, depending on the plane across which the crystal is sectioned. Zones which grow over the core are termed as rims. Note that there can be more than one rim depending on how many cycles of compositional change the magma undergoes. Rims are a few mm in thickness. Where more than one rim is present, the layers are termed as rim1, rim2 etc. In all crystals studied, there is an outermost selvage that has a strongly contrasting composition. This outermost layer is a few tens of microns thick, and has compositions that are increasingly albitic: compositions change from An60 to An40 or less in this thickness. It probably originates during post eruptional cooling of the lava flow. Since this layer is seen in both, zoned and unzoned crystals, it has no relation with the core-rim zoning. This outermost rim is therefore not considered during the evaluation of magmatic processes involved in the creation of crystal zoning. Where referred to it will be termed the "outermost rim". To summarize, the zoned crystals are composed of a core, one or more rim, and an outermost rim.

^{87}Sr/^{86}Sr Zoning in Thalghat GPB.

Thalghat GPB crystals are mostly unzoned, and only 2 of the 16 crystals studied showed zoning. CL images of zoned and unzoned crystals are shown in Figure 4.2. Figure 4.4 shows data collected across three unzoned (in terms of elemental zoning) phenocrysts from the Thalghat GPB. Sr-isotope ratios in these crystals vary from 0.71040 to 0.71060, with a few outliers. ^{87}Sr/^{86}Sr ratios of the groundmass plagioclase crystals form a tight cluster at ~0.71060, which is the same as that of the outermost ratios at the edges of the phenocrysts, both zoned and unzoned. Because the groundmass crystals have likely formed during eruption and cooling of the lava, it is reasonable to conclude that both such crystals and the rims of the plagioclase phenocrysts grew in the host lava while maintaining isotopic equilibrium with it.

Compositional variations along the length and width of the zoned crystals are shown Figures 4.5 and 4.6. As seen in the CL images of zoned crystals SS23A_tr1 and SS23A_tr2, the zoning is simple core-rim zoning. This zoning is not reflected in the major element or the trace element profile, but ^{87}Sr/^{86}Sr shows strong zoning with distinct core and rim isotopic ratios. The rim ^{87}Sr/^{86}Sr composition in both cases is ~0.71060; similar to that of the groundmass plagioclase, and therefore similar to the unzoned crystals. The cores and the rims both appear homogeneous within error, with a sharp change in composition across the core-rim boundary. The two crystals shown in Figures 4.5 and 4.6 differ in core compositions, SS23_tr1 has a higher core ^{87}Sr/^{86}Sr of 0.70985 (Figure 4.5) while SS23_tr2 has a core ^{87}Sr/^{86}Sr of ~0.70970 (Figure 4.6).

^{87}Sr/^{86}Sr Zoning in Kashele GPB.

In contrast to the Thalghat GPB, Kashele GPB crystals are *all* zoned, a typical

example of which is shown in Figure 4.3. Additional CL images of Kashele crystals

accompanied by compositional data are shown in Figures 4.7 – 4.11. Kashele GPB was

sampled in two locations with Sample numbers SS16 and SS11. While SS11 was a fresh

sample with clear plagioclase, SS16 was an altered flow that had plagioclase riddled with

cracks. However, the Sr-isotope analyses for both groups of crystals showed similar

measured Sr-isotopic ratios and crystal profiles were also comparable; for example the

core-rim variation of 0.70980 - 0.71080 in crystal SS16A_tr1 (Figure 4.7) is similar to

that in SS11B (Figure 4.10 center graph), therefore Sr isotope data from the altered SS16

was included in this study.

It is clear from Figures 4.10 and 4.11 that zoning in Kashele GPB is quite unlike

the simple core-rim zoning of the Thalghat. In CL images of Kashele crystals, the darker

zone boundaries show evidence of resorption features, especially in the outermost rims

(e.g. Figure 4.9). In a single crystal, core-rim variations range from 0.0004 to 0.0016 in

Δ^{87}Sr/^{86}Sr ratios, depending on the location of the transect. Tracks through crystal centers

(Figure 4.10 and Figure 4.11 bottom graphs) have small variations from 0.71040 (rim) to

0.71080 (core). This is opposite in style to Thalghat zoning where the core has a lower

ratio than the rim. When transects away from the center of the crystal are considered, the

variation increases to 0.70960 (rim) and 0.71080 (core, middle graph in Figure 4.10). At

the crystal extremities, the lower ratio of 0.70960 sharply rises to ~0.71040. Groundmass

plagioclase also shows a wide variation from 0.71020 to 0.71090.

Decoupled vs. non-decoupled zoning in An-content, trace element and Sr-isotope composition

Figures 4.5 and 4.6 show the variations in Sr, Ba and An-content across Thalghat GPB crystals and Figure 4.10 shows the same in a Kashele GPB crystal. For a crystal growing in thermodynamic equilibrium with a melt, there is a definite relationship between Ba and Sr in the plagioclase crystal versus that in the melt. Specifically, Sr is compatible in plagioclase while Ba is not (for An contents of 30% and above at 1100 °C e.g. Blundy and Wood, 1991). There is also a relationship between An content of plagioclase and Ba and Sr composition, viz that both are increasingly compatible in more albitic plagioclase. Relationship between trace elements and An content is therefore a measure of thermodynamic equilibrium in a crystal, and has been used by Zellmer et al. (1999) and Costa et al. (2003) to calculate crystal residence times.

In zoned Thalghat GPB crystals, Sr and Ba variations are very small over the bulk of the crystal, in fact, as Figure 4.5 and 4.6 show, the core and the rim have essentially the same Sr or Ba concentrations. This also corresponds with the An content, which shows little variation from an average An60 composition. There is therefore complete decoupling between isotopic and elemental variation in the Thalghat GPB. This is a surprising feature, because it requires growth of core and rim from two magmas that were nearly identical in major and trace elemental composition but widely different in isotopic composition. At the core-rim zone boundaries, there is a slight positive jump in An, which is reflected by negative dips in Sr and Ba. This behavior is expected from the thermodynamic relationship of Ba and Sr partitioning in plagioclase to the An content of the plagioclase (Blundy and Wood, 1991).

The Kashele GPB shows an interesting manner of coupling between trace element contents and isotopic ratios. Here the decoupling is not as strong and Sr and Ba are seen to vary directly with $^{87}Sr/^{86}Sr$. This variation is clearly seen at the crystal edge in the bottom left graph in Figure 4.11: as $^{87}Sr/^{86}Sr$ dips close to the crystal edge, Sr and Ba follow suit. However, this coupling does not extend to An content. Apart from a jump near the crystal edge, there is no variation in An corresponding to the trace element and isotopic variation.

Inferences from zoning in Thalghat and Kashele GPB

Equilibrium growth of Thalghat GPB

The Thalghat GPB are mostly unzoned, and the zoned crystals show simple core-rim zoning. The rims of the zoned crystals are similar in Sr-isotope composition to the unzoned crystals. The cores of the zoned crystals have lower Sr-ratios which are different from each other. This may be due to the two cores having separate growth histories before being introduced into the magma chamber in which the rim grew. Conversely, the core ratios could have been the same initially, but changed by solid state processes like diffusive equilibration. It is clear however that the rim zones and the unzoned crystals have a shared history. The cores and rims grew from two different magmas, perhaps in two separate chambers: the crystals initially formed in a chamber with $^{87}Sr/^{86}Sr$ compositions of ~0.7097 – 0.7098 and were then transported to a second magma reservoir where the rims began to grow. This is consistent with the idea that tholeiitic magmas pass through several magma chambers linked via dikes during transit from source to eruption (Marsh, 1988). The uniform groundmass composition, fairly uniform

rim composition of the Thalghat GPB crystal, and the broad thickness of its rim all appear to suggest that this crystal's rim grew in a steady-state, homogenized magma chamber. The equilibrium behaviour of trace elements in response to changing An-content is also a sign of equilibrium growth. In such a steady state condition of growth, the variation between the core and the rim $^{87}Sr/^{86}Sr$ composition can be thought to have resulted from diffusive equilibration across the core-rim boundary. The timescale of this diffusive process would allow the calculation of the residence time of the crystal in the magma chamber, since its growth has not been interrupted by crystal dissolution events.

Disequilibrium growth of Kashele GPB

By combining transects from all Kashele crystals measured, I prepared a schematic of $^{87}Sr/^{86}Sr$ zoning within a typical Kashele crystal showing a core and three rim zones: R1, R2 and R3 (Figure 4.12). The growth history can then be summarized as follows: during the initial part of the crystal's growth duration, the crystal grew in a magma of $^{87}Sr/^{86}Sr$ ratio 0.71080, although large and short lived variations did take place (as in Figure 4.11 top). Growth of rim R1 was accompanied by a smooth increase in of the crystal layers to 0.71120, followed by a smooth decrease back to 0.71080 and the growth of rim R2. This smooth increase and decrease could mean that the original magma mixed with another of higher $^{87}Sr/^{86}Sr$ ratio and its composition change was recorded in the growing crystal. Another change took place when a magma of lower $^{87}Sr/^{86}Sr$ was introduced, causing a smooth lowering of the $^{87}Sr/^{86}Sr$ composition to 0.70960. This event was then suddenly interrupted and magma composition changed rapidly to ~0.71040, growing rim R3 on the crystal. The crystal has therefore seen a

number of magmatic composition, and likely grew in a magma conduit rather than a homogeneous magma chamber.

The magnitude of Sr-isotopic variation in Kashele GPB (0.70960-0.71120) is larger than that of the Thalghat GPB crystals (0.70970-0.71080). Unlike Thalghat crystals, the zone boundaries do not exhibit large jumps in $^{87}Sr/^{86}Sr$, instead small oscillations in $^{87}Sr/^{86}Sr$ are seen. In this case, it appears that the crystal's growing faces were receiving nutrients from an adjacent melt whose $^{87}Sr/^{86}Sr$ composition was continuously changing. This is also borne out by the wide variation in Kashele groundmass plagioclase $^{87}Sr/^{86}Sr$ (0.71020 to 0.71090). This large variation mirrors the oscillatory behavior of $^{87}Sr/^{86}Sr$ in the giant plagioclase crystal, perhaps implying that in this case the crystals grew in a fairly unsettled, non-steady state environment. This type of growth may have happened in a solidification front in a dike-like conduit, rather than a magma chamber network as suggested by Sen et al. (2006).

In both the Kashele and Thalghat GPB crystals, the An content does not vary more than ±5%, which corresponds to a variation of about 150 ppm Sr and 45 ppm Ba; calculated at 1100°C using equations in Blundy and Wood (1991). These are more or less the variations we see in our samples. However, the trace element variation in the Kashele GPB does not follow the thermodynamic condition that Sr and Ba variation should be opposite to that of An, as there is no positive An peak corresponding to the dip in trace elements (bottom graph Figure 4.11). The Kashele therefore grew in disequilibrium conditions, an additional effect of growth in a non steady state environment.

Correlation between zones and erupted flow compositions

It is clear that the zoned Kashele and Thalghat GPB crystals have recorded multiple magmatic signals. Sen (2001) postulated that the signals recorded by GPB crystals would be inherited from magmas that gave rise to flows underlying the GPB. Figure 4.13 compares $^{87}Sr/^{86}Sr$ of crystal zones with $^{87}Sr/^{86}Sr$ of sub-GPB flows. The outer rims of the crystals are seen to be in equilibrium with the host lava flows. In the Thalghat GPB, the core zone with lower $^{87}Sr/^{86}Sr$ cannot be explicitly correlated to an underlying flow. Of the flows underlying the Thalghat GPB, SS21 can be discounted as it has high $^{87}Sr/^{86}Sr$ ratios, but flows SS3, SS5 and SS22 all have low $^{87}Sr/^{86}Sr$ of~ 0.70900. This value is significantly smaller than the Thalghat GPB core value of 0.70960. The magma in which the GPB core grew thus has a composition intermediate between the highest and lowest in the Jawhar Formation, and has no surface expression as a lava flow.

The Kashele GPB zones show good correlation with the stratigraphically lower flows of the Igatpuri Formation. The $^{87}Sr/^{86}Sr$ variations in analyzed Kashele crystals represent nearly all the Igatpuri flows, with exceptions being the high Mg# flows. The source magma of the high Mg# flows SS211 and SS29 would have a higher temperature, and would probably cause dissolution of plagioclase rather than growth. This may be why $^{87}Sr/^{86}Sr$ compositions of the high Mg# flows are not recorded in growing plagioclase crystals. Close to the outer rim, the $^{87}Sr/^{86}Sr$ compositions of Kashele plagioclase decrease to 0.70960 (Figures 4.10, 4.12). This composition is not seen in any of the Igatpuri flows. Oddly, this value is the same as that of the Thalghat GPB zone, which, as seen above, has no correlation with erupted Jawhar Formation lavas (these values are listed in bold lettering in Figure 4.13). The ~2 cm phenocrysts from flow SS27 (which

are not considered to be "giant" plagioclase for reasons stated in Chapter 3) show a similar range in $^{87}Sr/^{86}Sr$ as the Kashele GPB, and also have 0.70960 as the lowest measured ratio. The significance of this fixed lower limit for all sizable phenocryst phases from the Thalghat and Kashele flows is not clear, but it points to a long lived magma composition that was involved in the origin of large phenocrysts, but had no eruptive expression. It is clear from $^{87}Sr/^{86}Sr$ zoning that Keshele GPB crystals were growing throughout the duration of magmatic activity pertaining to eruption of the Igatpuri Formation.
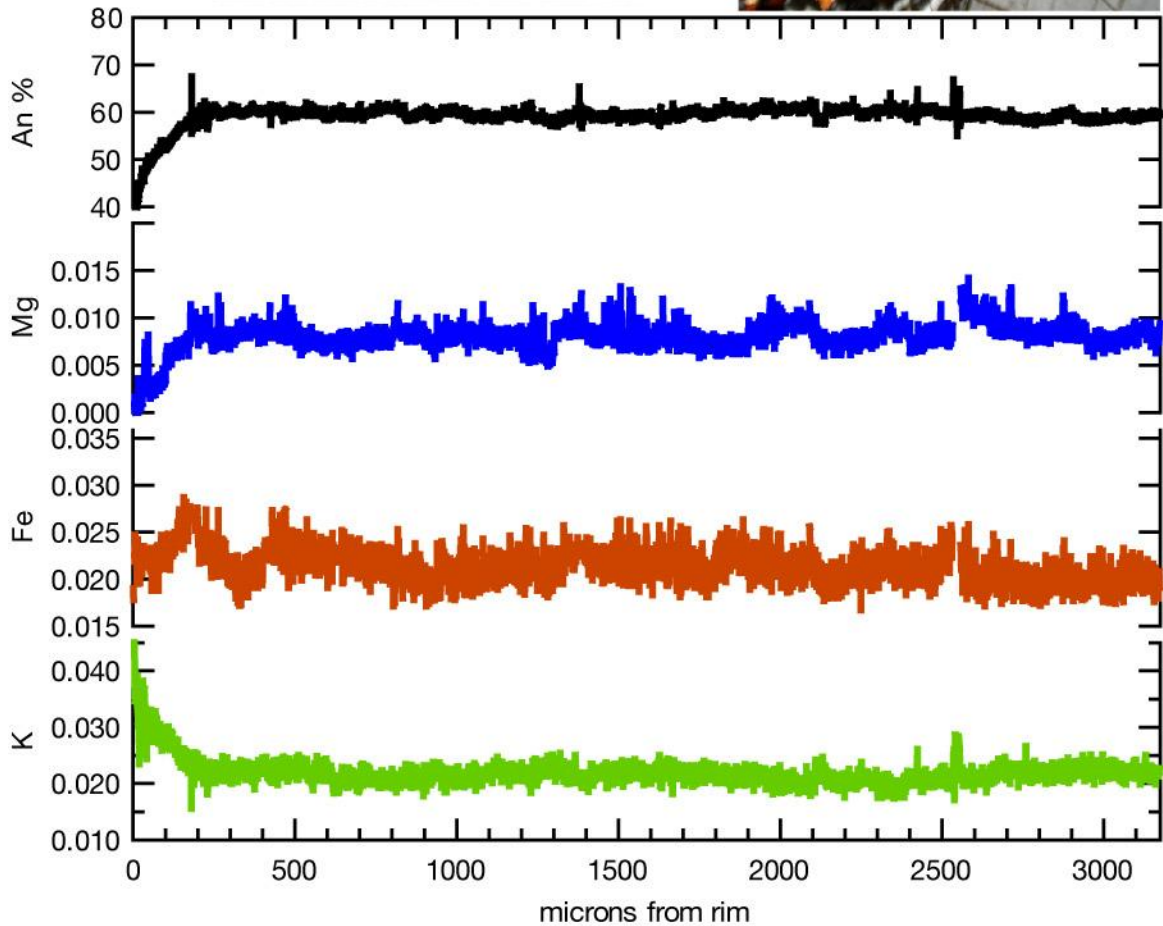
Figure 4.1. Oscillatory zoning in a giant plagioclase crystal. Top - cross polarized light image of a section of Thalghat crystal SS23. The width of the image is ~5mm. the image is a composite of multiple overlain images, and artifacts are seen as diagonal boundaries of differing brightness. Oscillatory zones are seen as faint grey lines that follow the

outline of the crystal. The crystal contains inclusions of altered olivines and glass pockets. The edge of the crystal at the right of the image shows a markedly darker rim, which could be due to an albitic overgrowth. White dashed line shows the path along which electron microprobe analyses were carried out at 1 micron intervals. Bottom: data from electron microprobe transects across the crystal. An content, Mg, Fe and K are presented as molar proportions calculated according to the plagioclase structural formula. It is seen that major zoning is absent and variations due to the oscillatory zoning are small. The albitic overgrowth is ~200 microns thick and is characterized by a smooth decrease in An content accompanied by a decrease in Mg and an increase in K.
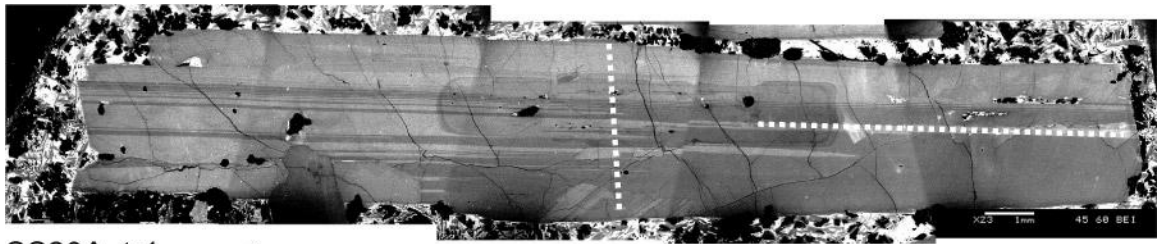
SS23A_tr1 ▭ 1 mm
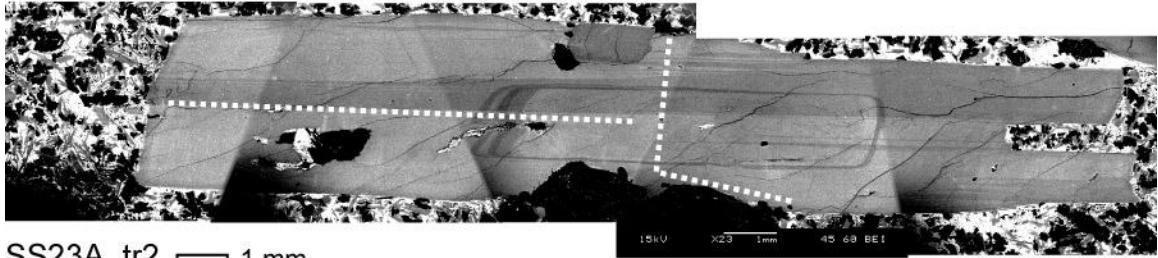
SS23A_tr2 ▭ 1 mm
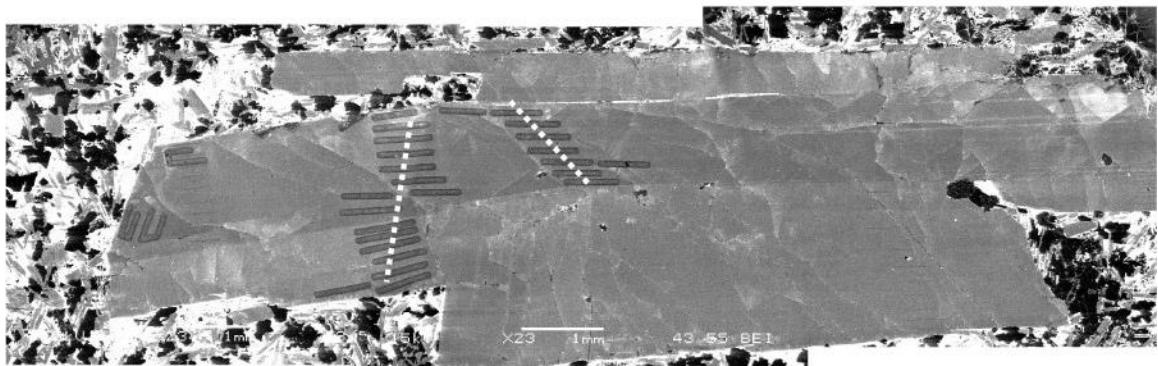
SS23 ▭ 1 mm
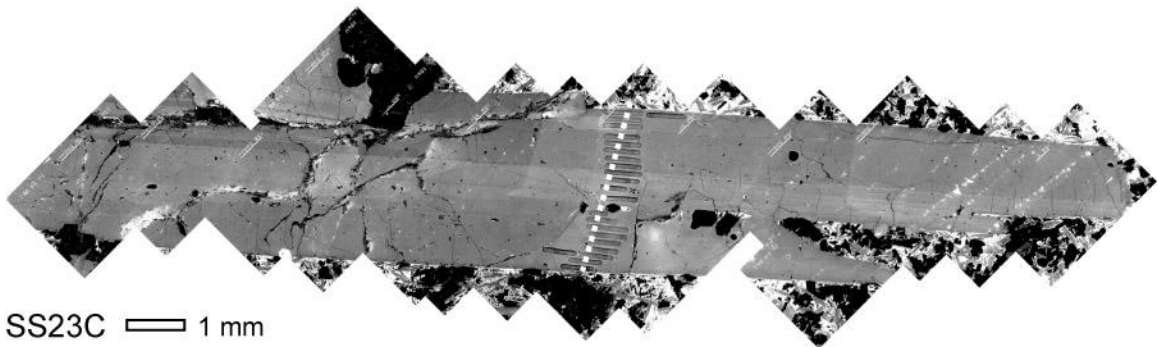
SS23C ▭ 1 mm

Figure 4.2. CL images of zoned and unzoned plagioclase from the Thalghat GPB.
The images are cathodoluminescence (CL) image mosaics of sectioned plagioclase
crystals. Artifacts of the mosaicing process are seen as diagonal lines of unequal
brightness cutting across the width, especially in the two upper images. Dotted lines
represent directions across the crystals along which electron microprobe and laser

60

ablation ICPMS data has been collected. The crystals in the upper figures are zoned, with the core zone visible in CL. In the lower two figures, laser ablation tracks are clearly visible, arranged parallel to each other, and orthogonal to the actual direction of traverse. In the two upper crystals, SS23A_tr1 and SS23A_tr2, data have been measured in two directions across the crystal, rim-to-rim in the short direction, and rim-to-core in the long direction.
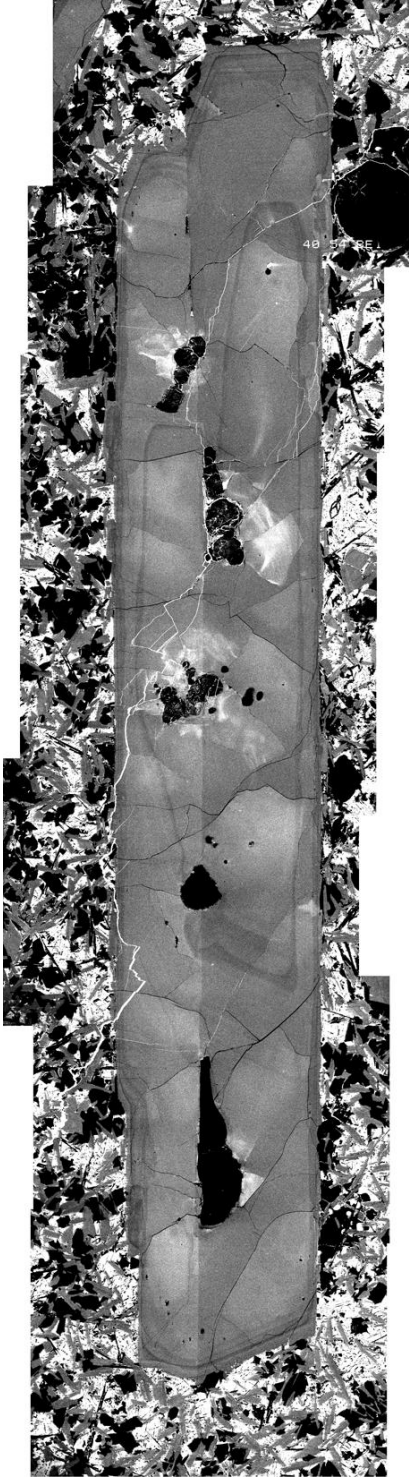
Figure 4.3. CL image of a typical Kashele plagioclase phenocryst. The zoning in this crystal is very different from that of the Thalghat GPB. The zones are narrower towards the crystal extremities, and have rounded outlines.
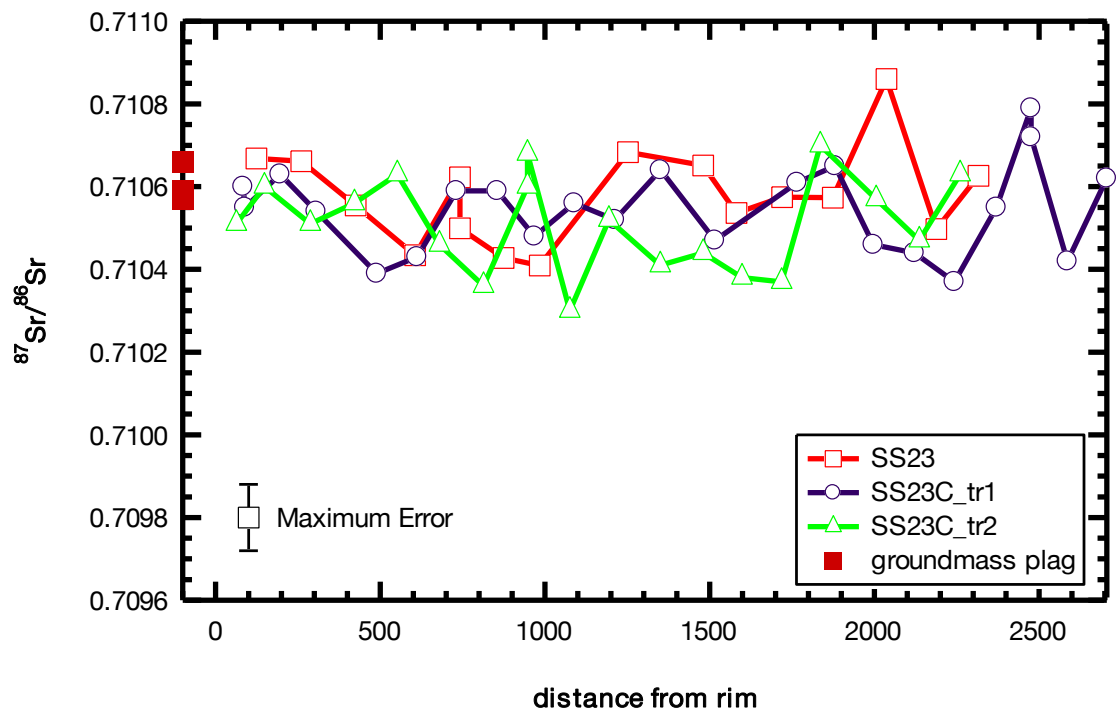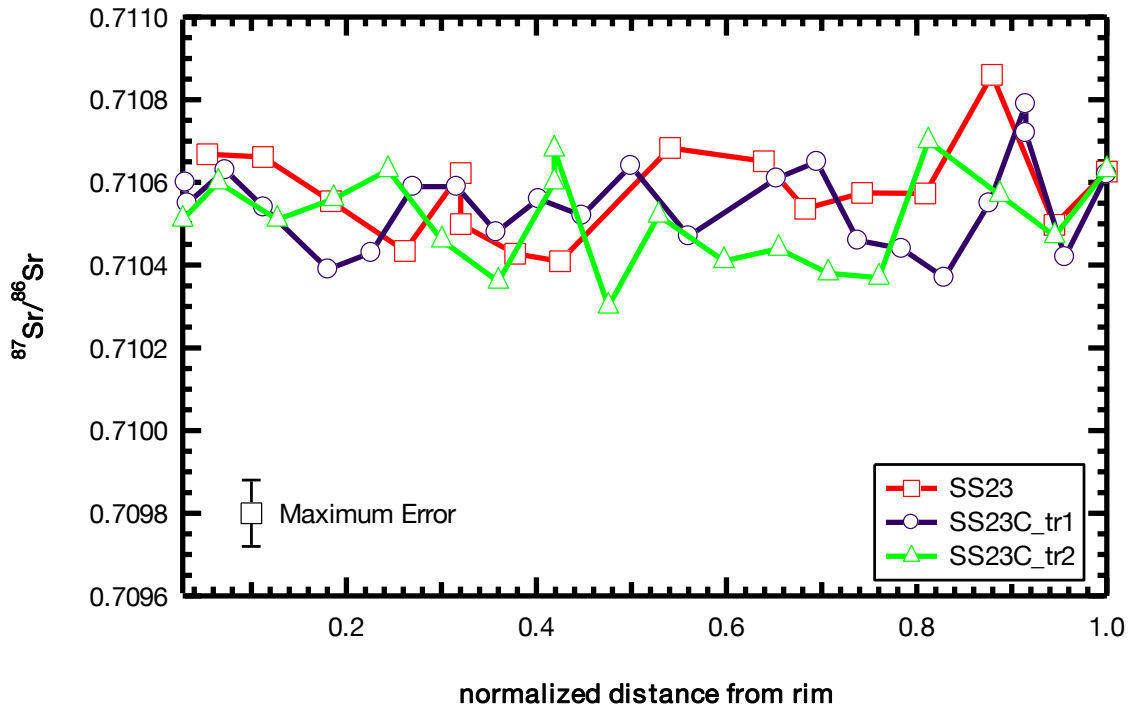
Figure 4.4. Sr isotope variations in unzoned Thalghat GPB crystals. The two graphs show variations in Sr isotopic ratios along core-rim transects through unzoned Thalghat GPB crystals (open symbols). Isotopic ratios measured on groundmass plagioclase crystals are plotted at x<0 on the y axis as solid red squares. In the bottom graph, data are plotted with distance from the crystal rims on the x-axis. On the top graph, transect

distances are normalized from 0 to 1, so that rims can be better compared. Though there is some variation in Sr-isotopic ratios, the rims of the crystals are consistently around 0.71060, which is also the isotopic ratio of the groundmass plagioclase (solid squares).
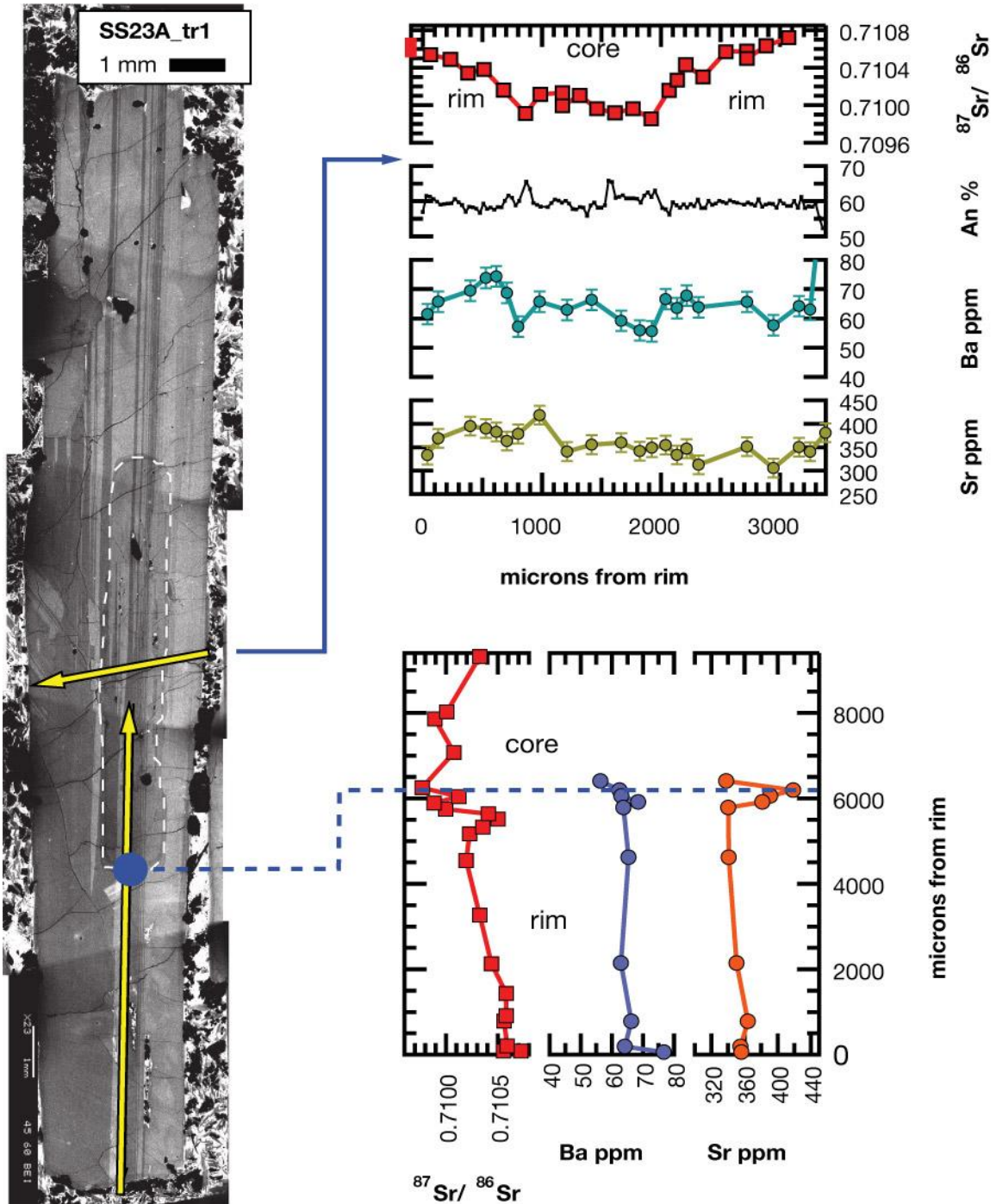
Figure 4.5. Zoning in crystal SS23A_tr2 from the Thalghat GPB. Left: Composite CL image of crystal SS23A_tr2. Note the core zone in the center of the crystal (white dashed outline). Upper graph shows data measured across the width of the crystal and lower graph shows data measured along its length. Sr isotopic ratios show a sharp change at the zone boundaries, accompanied by a jump in Sr and Ba and a minor jump in An. Isotopic ratios measured on groundmass plagioclase crystals are plotted at x<0 on the y axis as solid red squares on the upper graph.
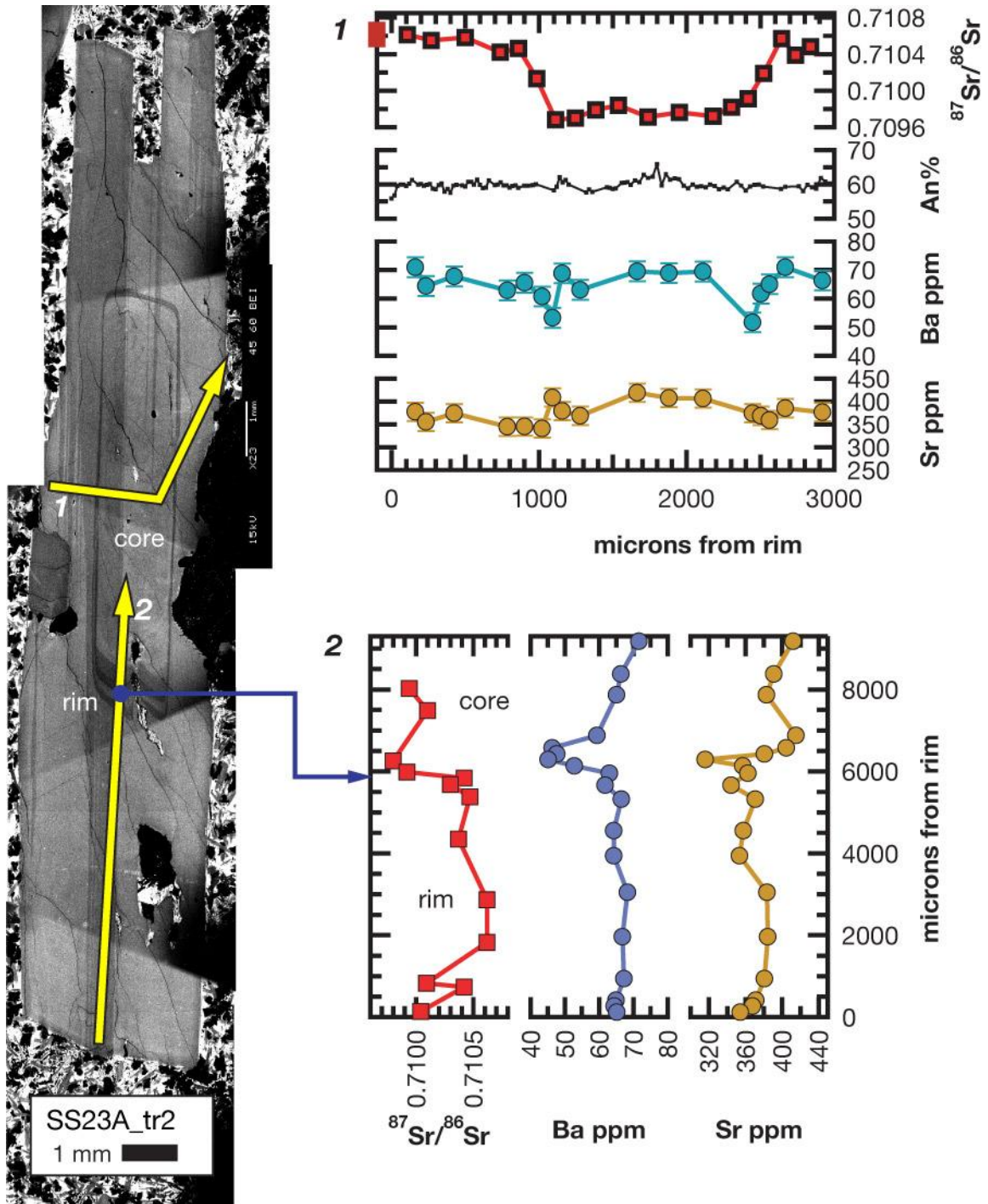
Figure 4.6. Zoning in crystal SS23A_tr2 from the Thalghat GPB. Left: Composite CL image of zoned Thalghat giant plagioclase crystal SS23A_tr2. The core is clearly visible in the center of the crystal. Chemical variations have been measured along the arrows in orthogonal directions across the crystal. Right. The upper graph shows rim-core-rim variations across the width of the crystal, and the lower graph shows core-to rim variations along the length of the crystal. Isotopic ratios measured on groundmass

plagioclase crystals are plotted at x<0 on the y axis as solid red squares in the upper graph.
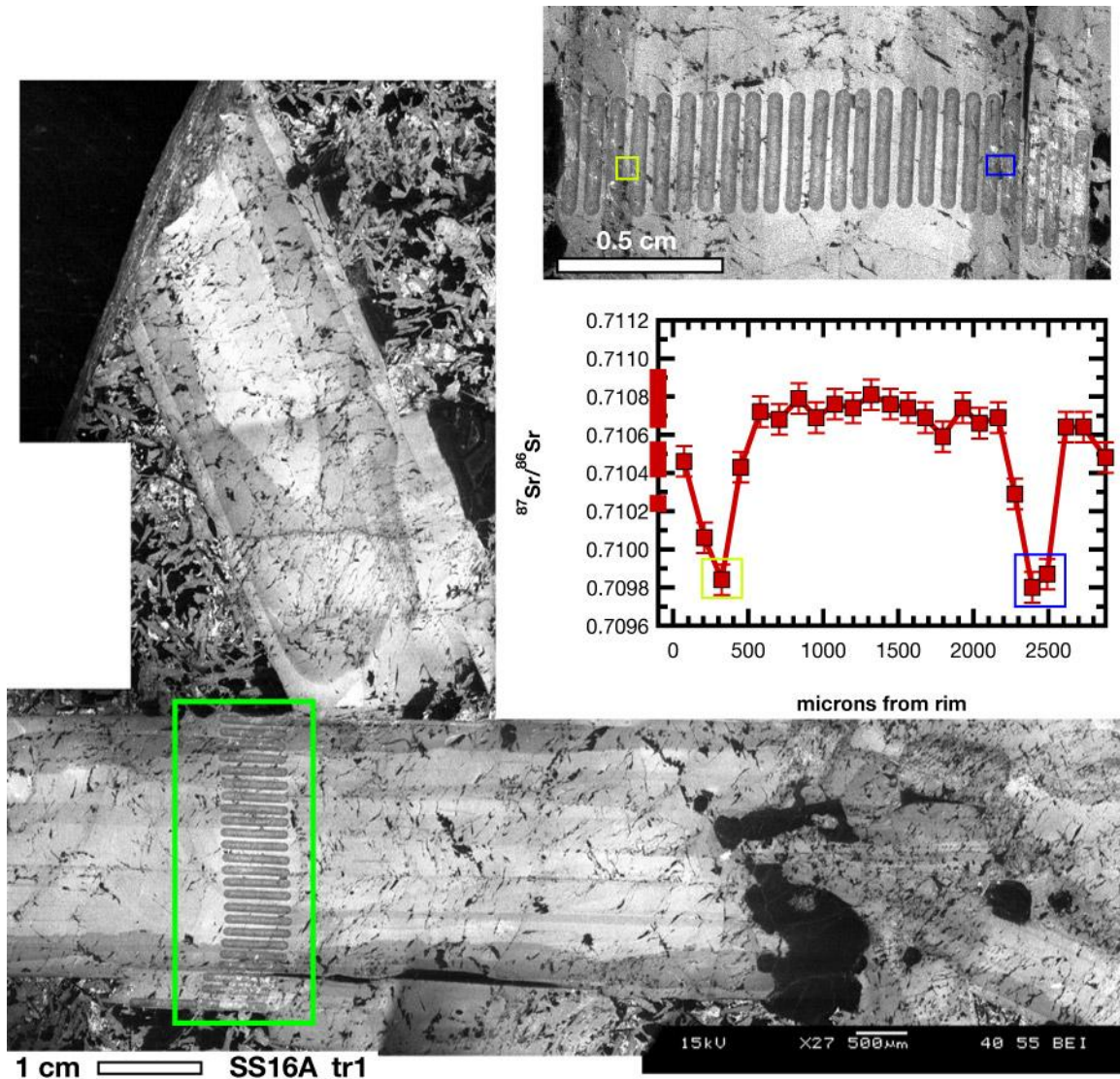
Figure 4.7. Zoning in crystal SS16A_tr1 from the Kashele GPB. The L-shaped image is a composite CL image of two crystals from the Kashele GPB. Compared with other analyzed crystals, crystals from flow SS16 are altered, and this is visible as numerous black areas in the CL image. The Zoning is clearly visible in the upper crystal which displays a core, mantle and rim zone. The lower crystal shows parallel laser tracks along which $^{87}Sr/^{86}Sr$ data were measured. This section of the crystal (within the green box) is magnified in the image above the graph. The graph shows $^{87}Sr/^{86}Sr$ ratios along the transect (outlined squares) and tracks along which the data show steep dips are outlined in blue and yellow on the image and on the graph. Isotopic ratios measured on groundmass plagioclase crystals are plotted at x<0 on the y axis as solid red squares. The scale of the y-axis from 0.7096-0.7112 represents the maximum $^{87}Sr/^{86}Sr$ variation measured in the Kashele crystals, and all Kashele data in the following figures are plotted on the same scale.
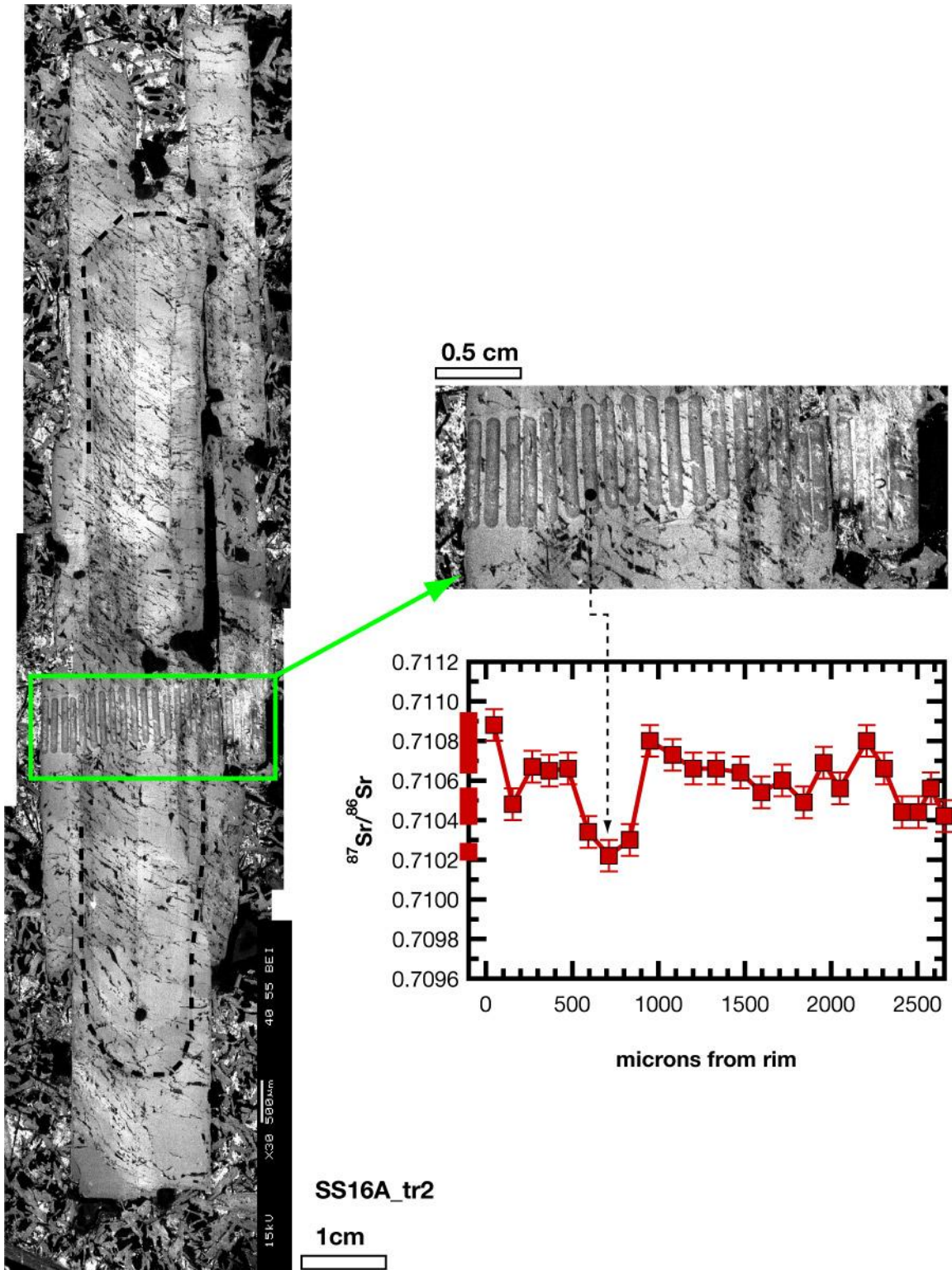
Figure 4.8. Zoning in crystal SS16A_tr2 from the Kashele GPB. Left: composite CL image of crystal SS16A_tr2 from the Kashele GPB. Because of the alteration, zoning features are not easily visible. Where possible, observable zoning has been outlined in

dashed black lines. The upper right image is a magnified view of the laser ablation tracks. The graph shows $^{87}Sr/^{86}Sr$ ratios along the transect. Not much variation is seen, and the location of the single dip in ratios is marked on the image. Isotopic ratios measured on groundmass plagioclase crystals are plotted at x<0 on the y axis as solid red squares.
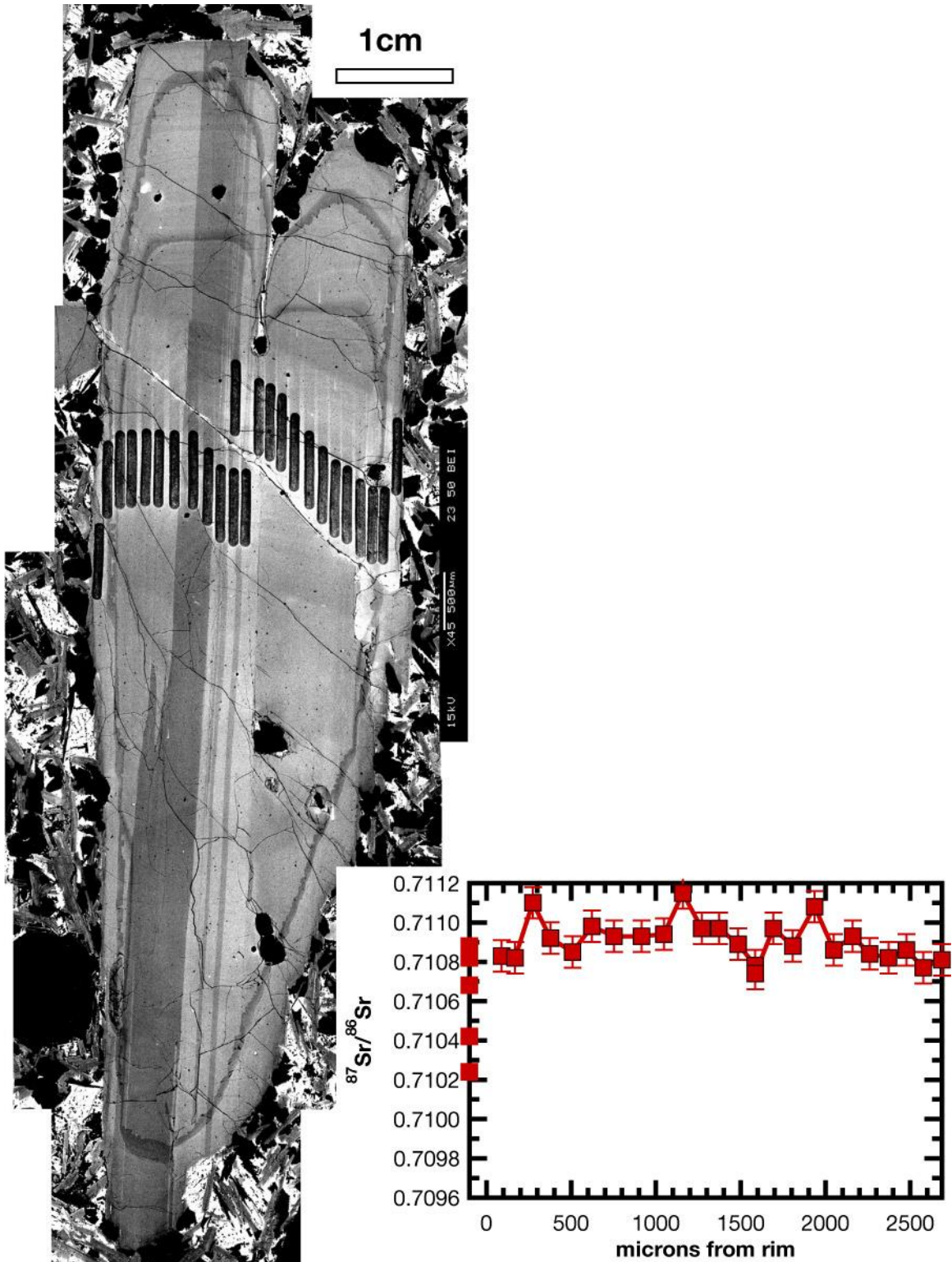
Figure 4.9. Zoning in crystal SS11_tr2 from the Kashele GPB. Left: composite CL image of crystal SS11_tr2 from the Kashele GPB flow. The image shows well defined rim zones with sharp boundaries. Note that the core is not seen in this image, and the

number of zones are also smaller that those seen in the crystals in the following graphs. Oscillatory zoning is faintly seen between the more clearly defined rim zones. The rim zones have a tapering outline towards the crystal edge. The outermost zone boundary shows an undulating outline that could have resulted from dissolution events. The graph shows $^{87}Sr/^{86}Sr$ data across the ablation tracks visible in the crystal. The variation in this crystal is very small, and the $^{87}Sr/^{86}Sr$ ratios the highest in the Kashele crystals studied. Isotopic ratios measured on groundmass plagioclase crystals are plotted at x<0 on the y axis as solid red squares.
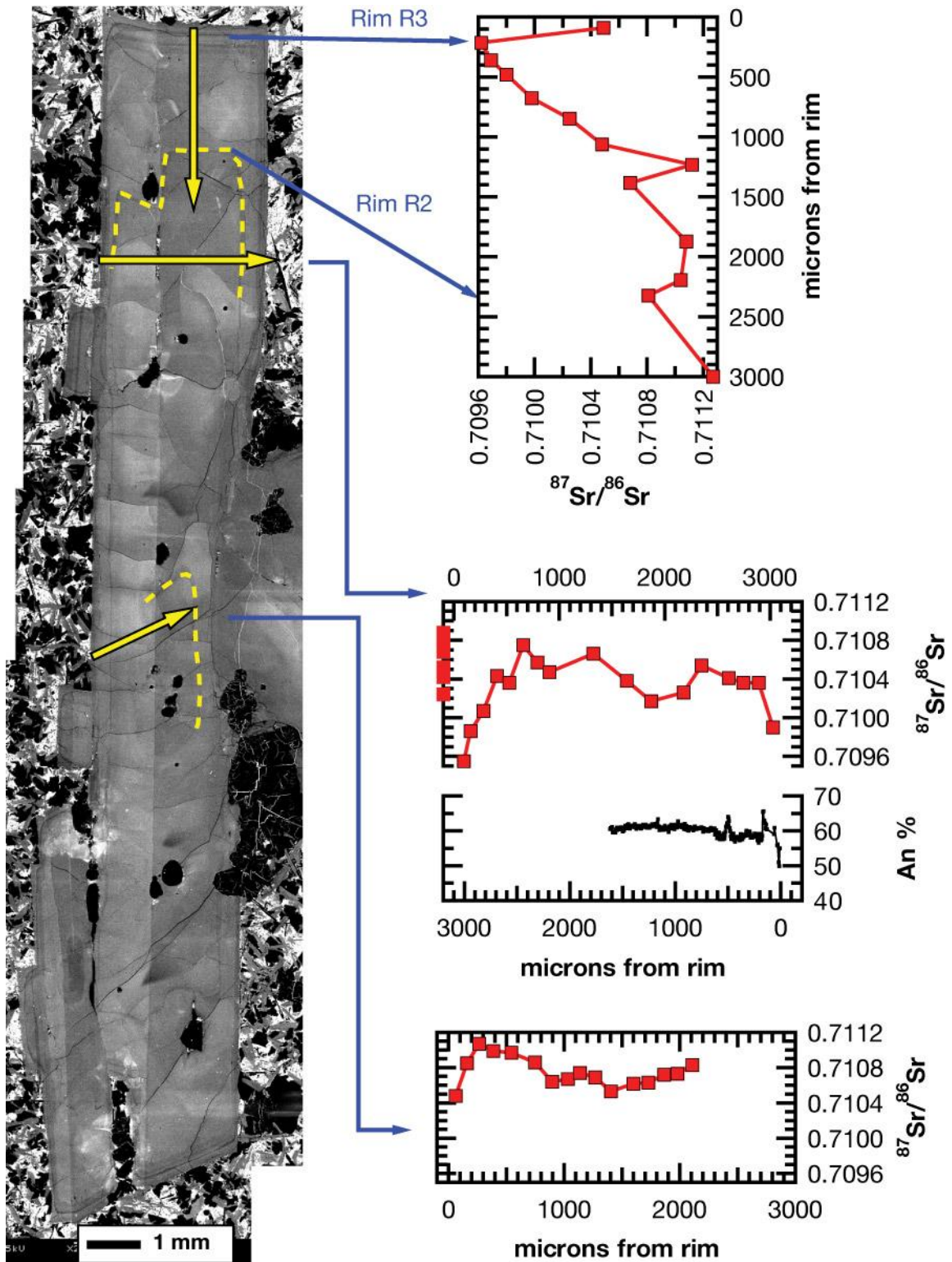
Figure 4.10 Zoning in crystal SS11B from the Kashele GPB. The zoning in this crystal is outlined by yellow dashed lines. The core is faintly visible in the center of the crystal. Sr isotopic ratios have been measured in three directions across this crystal, marked by

yellow arrows and data are shown in the graphs alongside. Arrows marked Rim R3 and Rim R2 locate the data points corresponding to the rims on the y axis of the upper right graph. The middle graph also shows An-content measured parallel to the laser tracks. The An-content of the crystal is nearly constant at An60 except near the crystal edge. It does not follow the variations in $^{87}Sr/^{86}Sr$. Isotopic ratios measured on groundmass plagioclase crystals are plotted at x<0 on the y axis as solid red squares in the middle graph
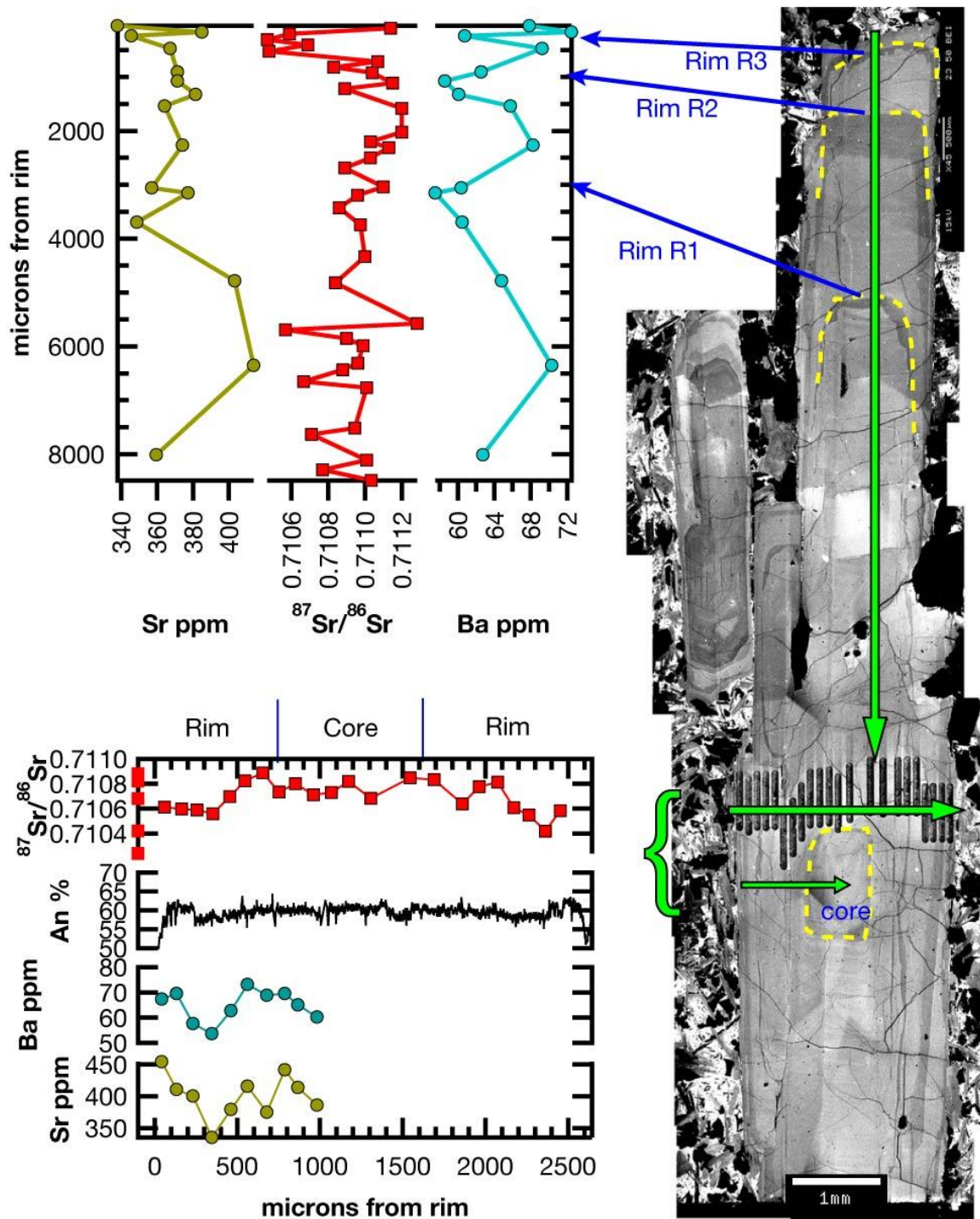
Figure 4.11. Zoning in crystal SS11_tr1 from the Kashele GPB. Zones in this crystal are clearly visible and are outlined in dotted yellow lines. This crystal was truncated from the bottom during sectioning, and the core which now appears at the lower end is actually in the center of the crystal. Both elemental and isotopic analyses were carried out along the arrows marked. The core of the crystal does not show any change in composition at

its boundaries (lower graph). Elemental Sr and Ba concentrations seem to roughly follow the isotopic variations, but An-content does not.
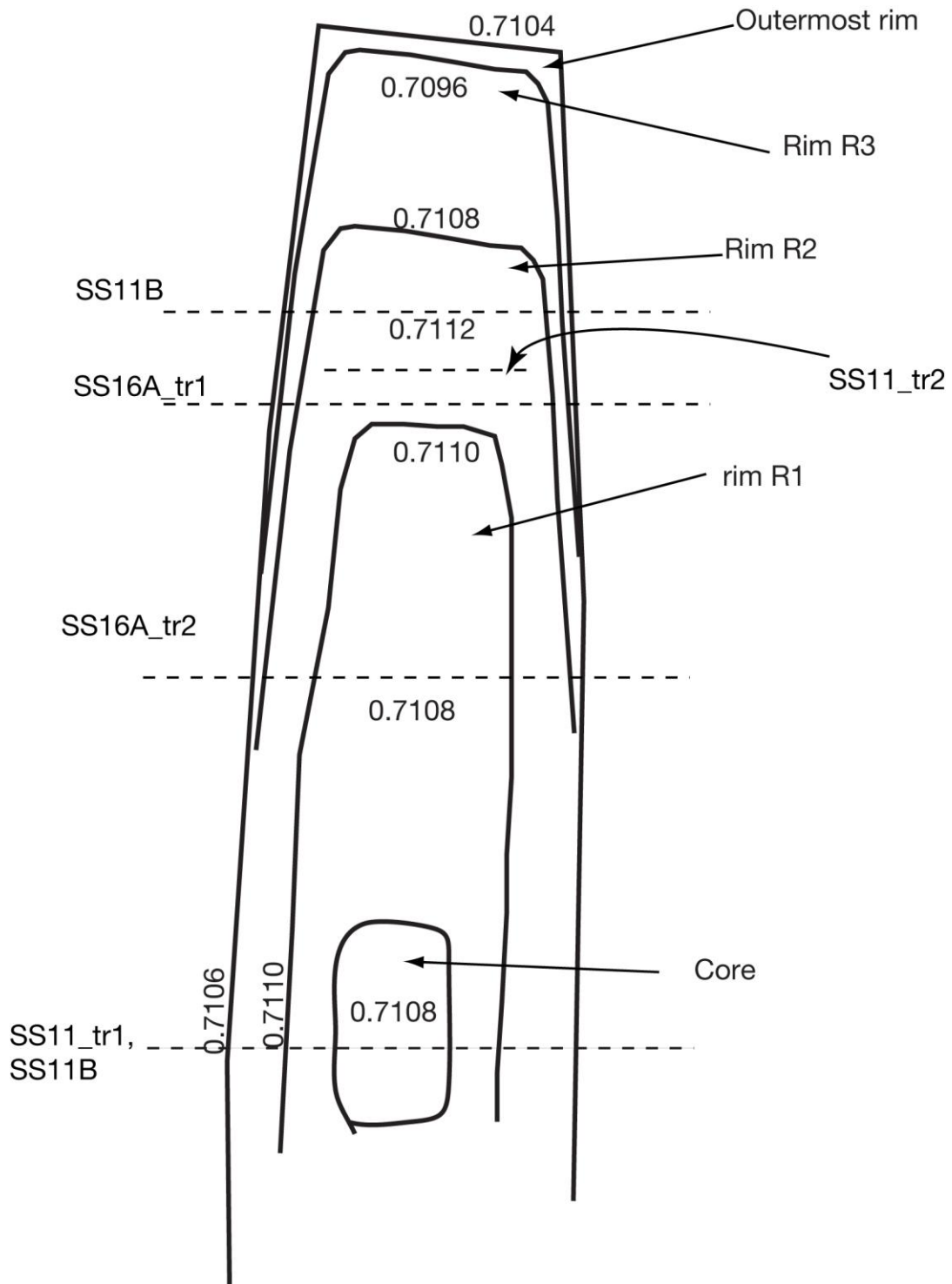
Figure 4.12. Schematic for Sr isotopic zoning in Kashele crystals. Data from all the Kashele crystal profiles are used to assemble this schematic. Kashele crystals have a small ~1mm core, three broad rim zones and a thin outer rim zone. Each rim zone has a change in isotopic value assiociated with it, but the change is not always sharp across the zone, except for the R3 rim zone. The numbers in the diagram are approximate $^{87}Sr/^{86}Sr$

values at various locations in the crystal. Dashed lines are approximate locations across which profiles have been measured in different Kashele GPB crystals, and are labeled with names of the crystals.
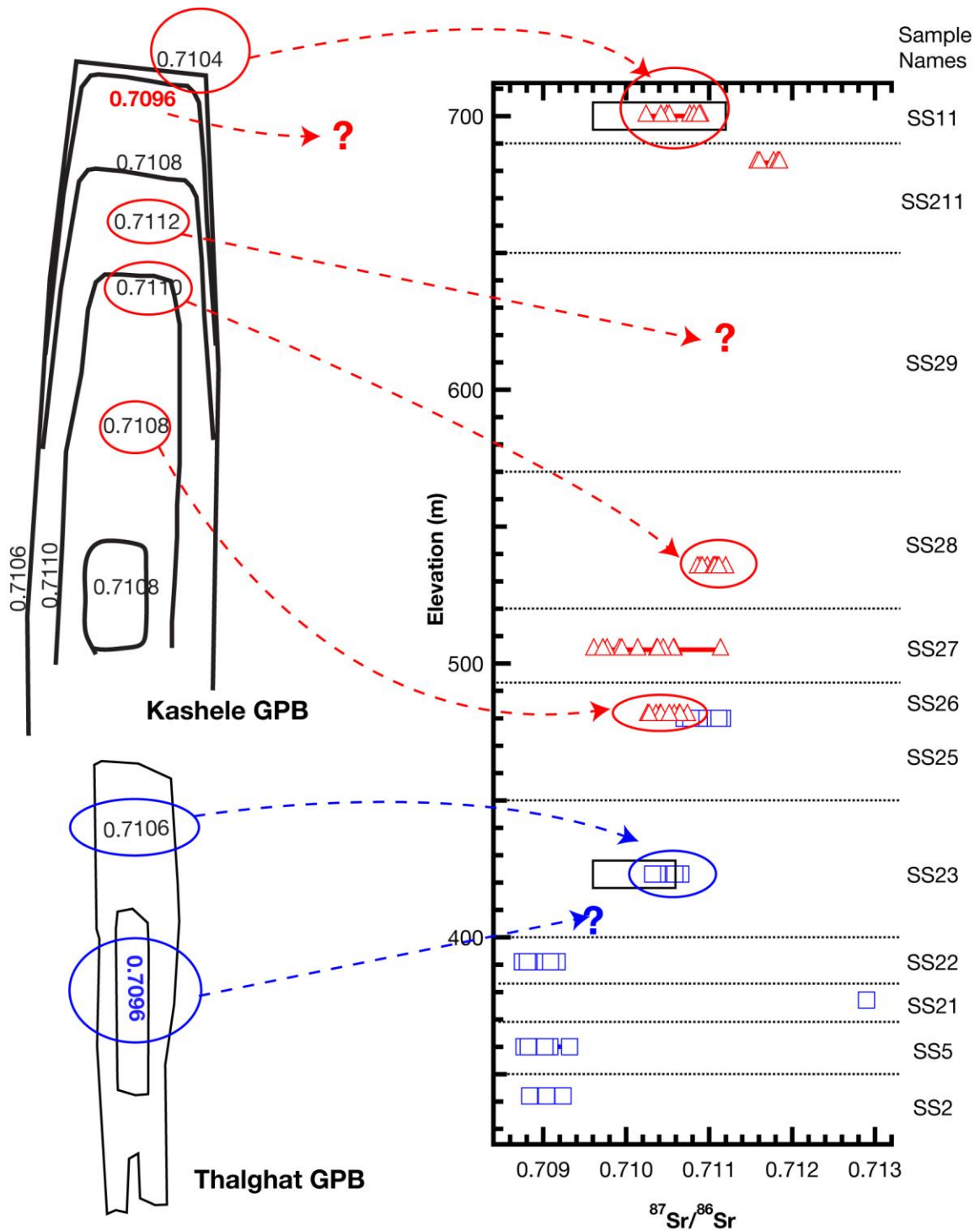
Figure 4.13. Correlation between crystal zones and flow compositions. Sr-isotope compositions of GPB crystal zones are compared with those of underlying flows. Schematics for zoned Kashele and zoned Thalghat plagioclase are shown on the left, with Sr-isotopic ratios marked in each zone. Stratigraphic variation of Sr isotopes in erupted flows is shown on the right, with the flow names marked. $^{87}Sr/^{86}Sr$ of flows is measured

on groundmass plagioclase crystals, except for SS27, data from which were collected on plagioclase phenocrysts. Arrows connect zones and flows of similar compositions. Question marks denote zones that cannot be correlated with any flow. Zones with the $^{87}Sr/^{86}Sr$ value of 0.7096, which have no corresponding flow of similar composition, are marked with bold lettering; red for Kashele and blue for Thalghat plagioclase.

CHAPTER V

MODELING $^{87}Sr/^{86}Sr$ ZONING IN GIANT PLAGIOCLASE CRYSTALS:

IMPLICATIONS FOR DECCAN ERUPTION DURATION

Introductory Remarks

Plagioclase phenocrysts in basaltic and andesitic magma often preserve elemental and Sr-isotopic zoning during growth from magma, examples of which we have seen in the previous chapter. The task of the petrologist is to unscramble such records and obtain information on time scales of crystal growth processes and evaluate the chemical and thermodynamic, and kinetic conditions in which the crystals grew (Zellmer et al., 1999; Davidson et al., 2001; Costa et al., 2003; Tepley and Davidson, 2003; Ramos et al., 2005). In this chapter, I treat the observed Sr-isotope zoning in the plagioclase crystals as possible diffusion profiles and obtain time information from modeling such diffusion profiles. I consider a variety of initial and boundary conditions that are possible in the situation of a plagioclase crystal growing in a magma chamber. I also discuss the interplay of diffusion and crystal growth processes, and compare the profiles arising from these considerations to the measured data.

In order to illustrate the processes involved in forming the giant plagioclase phenocrysts, let us consider a crystal growing in a magma chamber as shown in Figure 5.1. At some point in the growth history, a new batch of magma has been introduced, changing the composition of the mixed magma. The continuous growth of the crystal through this event introduces a compositional jump, leading to the formation of a crystal rim with a separate composition (note that the use of the terms "core" and "rim" is

clarified in the previous chapter). Diffusion will act to smooth out the compositional change across the zone boundary. There are several possible combinations of diffusion and crystal growth processes that can occur. The two "end-member" possibilities are: (1) the diffusive equilibration starts only after the zoned crystal is fully grown, and (2) diffusion starts as soon as a new zone forms. In both cases and in all intermediate possibilities diffusion continues as long as the crystal resides within the magma but stops as soon as the magma erupts, i.e., the crystal is "quenched" below the closure temperature for the element in question – in this case Sr.

As we noted in Chapter IV, the zoning profiles in the large plagioclase crystals in the Thalghat GPB and Keshele GPB are very different. The simple core-rim zoning of the Thalghat crystals (Figure 5.2) is better suited for diffusion modeling as discussed below. Following these discussions, I will attempt to extrapolate the calculated timescales from phenocrysts to the life span of an individual magma chamber.

Different cases of growth vs. diffusion: Application to the Thalghat plagioclase

Case 0. Growth from mixed magma and no subsequent diffusion across the zone boundary

As a "zeroth" condition, one can consider a case where diffusion does not play a role in the modification of crystal compositions. In this case, a crystal grows from an isotopically homogeneous magma until it reaches a certain size at which point a different magma with very different isotopic composition intrudes the magma chamber and mixes with the preexisting magma. The nature of the isotopic zoning within the crystal would depend upon whether the crystal was growing in a melt-dominated vs. crystal-dominated

environment within the magma chamber. Mixing of the new magma with the preexisting melt would be most efficient in the melt-dominated part of the magma chamber where crystal proportion is less than 25% (i.e., suspension zone, Marsh, 1996). A rapidly growing plagioclase crystal in the suspension zone would capture this mixing event by developing a zoning pattern with a sharp step across the zone boundary. This is schematically shown in the top and middle row of Figure 5.2. The size of the step would depend on the difference in the isotopic composition of the two magmas and on relative rates of mixing vs. crystal growth. On the other hand, in the mush zone (25-50% melt), the chances are that mixing of the new and existing melts would not occur instantaneously. A crystal growing in the mush zone may simply record a "mixing profile", a reflection of the changing composition of the surrounding melt during the mixing event. This situation is considered in Case 7.

As seen in Figure 5.2, TGPB zoning can be thought to be a simple case of a homogeneous core and homogeneous rim zone with $^{87}Sr/^{86}Sr$ values of 0.7096-0.7098 and 0.7106, respectively. However, within the ~400 micron boundary layer between the two zones, $^{87}Sr/^{86}Sr$ profile clearly does not show a sharp step like boundary. The boundary could have resulted from slower growth in a mush zone as stated above, or it could have resulted from diffusive equilibration. The different possibilites are considered below.

Case 1: Independent growth and diffusion

In this case, the crystal grows in a melt-dominated part of the magma chamber as described above. Diffusion will act to smooth out the initial step profile and here I consider diffusion to occur only after the crystal has reached its full size i.e. growth is

assumed to be decoupled from diffusion. Such a situation will be possible if growth rates of the core and rim are infinitely faster than diffusion rates. Core and rim growth in such a situation is schematically illustrated in Figure 5.3. In this case the initial profile prior to diffusion will be a square U-shaped step profile as shown in the second row of Figure 5.3. Diffusion then acts to smooth the profile (third row of Figure 5.3).

Under these conditions, diffusion modeling will enable the calculation of the residence time of the crystal in the magma chamber, but we cannot have a handle on the growth rates, except to note that they will be faster than diffusion. However, at high magmatic temperatures, it is highly unlikely that diffusion would be completely inhibited during the entire time of crystal growth. It is more likely that diffusion ensues immediately after a chemical gradient is set up between two adjacent layers within the crystal.

Calculations with the software COMAGMAT (Ariskin, 1999), show that liquidus of the GPB lava (minus the giant plagioclase crystals) is 1150° C; and at 1100° C, the magma forms 25% plagioclase crystals whose An-content would be similar to those of the analyzed phenocrysts. It is therefore likely that these crystals grew at 1100 – 1150° C. Under such conditions diffusion of Sr would be fairly rapid: at 1100° C, D_{Sr} (diffusivity of Sr) is $\sim 10^{-17}$ m^2/s (Cherniak and Watson, 1994; Giletti and Casserly, 1994) as opposed to 10^{-21} for D_{Si} (Cherniak, 2003). Furthermore, the Sr-isotope contrast between the core and rim is large, and therefore, the tendency to diffuse will be strong.

Case 2: Simultaneous and interfering growth vs. diffusion

As in the previous case, the crystal is growing in the melt, and at one point, a new batch of melt with contrasting Sr-isotope composition is introduced into the chamber,

causing the growth of the crystal rim layer. Once rim growth begins and a gradient in Sr-ratios is initiated, diffusion will commence simultaneously. Let us first consider a case where diffusion rates are very rapid, so that the growth front never lags behind the diffusion front. At any timestep, a new layer added to the growing crystal will always be affected by diffusion (See Figure 5.4). The final diffusion profile will have to be modeled as a moving boundary problem, where at each time interval, the diffusion front reaches the crystal boundary. As a result, the final profile will not be flat near the crystal edge (line t3 in Figure 5.4). Note that in the analyzed crystals (Figure 5.2), the isotopic profile in the rim is flat from the edge up to a distance of 700 microns inward, showing that the diffusive front has not yet reached the crystal edge; therefore the condition of diffusion and growth fronts interfering is not applicable to the measured TGPB data. Also note Figure 5.6 where calculations of the relative positions of growth and diffusive fronts for appropriate rates are presented; the diffusive front always lag behind the growth front.

Case 3: Simultaneous and non-interfering growth vs. diffusion

In this case, the diffusion front always lags behind the growth front. Diffusion will once again begin immediately after a layer of rim grows over the core, but the outermost edge of the rim is still not affected by diffusion (Figure 5.5). In Figure 5.6, positions of growth and diffusive fronts are calculated at timescales upto 30 years, using growth rates from Cashman and Marsh (1988), and Sr diffusion rates from Giletti and Casserly (1994) and Cherniak and Watson (1994). Within less than a year, the growth front is seen to overtake the diffusive front. Even if an order of magnitude lower growth rate is used (as suggested by Higgins and Chandrasekharam, 2007, for Deccan GPB), the growth front overtakes the diffusive front in 20 years. Non interfering growth and

85

diffusion is therefore the most likely manner in which the Sr isotope profiles developed in the TGPB crystals.

The final profile can be modeled in a similar manner to Case 1 since diffusion and growth can be treated separately for modeling. The diffusion timescale will be the same as the rim growth time, provided diffusion and growth begin and end simultaneously. As noted earlier, diffusion will commence as soon as a crystal layer of contrasting composition is added to the growing crystal. The closure temperature for Sr diffusion in plagioclase is high, ~800 °C for An64 at a cooling rate of 200 °C/Ma (Giletti and Casserly, 1994), and after the crystal bearing lava is erupted at ~1100 °C, diffusion would stop fairly quickly. Growth of albitic rims on the crystals (An 40) is evidence of further growth in a cooling magma, but these rims are just tens of microns wide, and can be ignored since the resolution of each $^{87}Sr/^{86}Sr$ data point is 80 microns. Hence, we can assume that diffusion and rim growth began and ended simultaneously, and the diffusion timescale is equivalent to the rim growth time.

To summarize, the Thalghat GPB crystals can be considered to have grown in two stages, the core growth stage and the rim growth stage. The initiation of rim growth corresponds to the initiation of diffusive activity. Diffusion can also be considered to have terminated at more or less the same time as the termination of crystal growth. Diffusion will always lag behind growth, enabling diffusive equilibrium to be calculated without taking into account the position of the crystal growth front. In order to set up the diffusion model, initial and boundary conditions of the model have to be set up.

Different initial and boundary conditions

There are many possible initial and boundary conditions under which diffusion could occur, and the model results depend strongly on the choice of initial and boundary conditions. I now consider the different possible situations.

Case 4: Initially unzoned core and rim

In Figure 5.1, and in the treatments so far, core and rim growth were assumed to have occurred separately, possibly in different magma chambers, from melts that had different Sr isotope ratios. Another possibility is that the entire crystal was initially homogeneous with Sr-ratios of 0.7096, and the fully-grown crystal was transferred to another magma chamber that had a $^{87}Sr/^{86}Sr$ of 0.7106. This may explain the lack of variation in major and trace elements that are seen in the Thalghat and Keshele GPB crystals (previous chapter). In this case, after the crystal is transferred to the new chamber, diffusion will act to elevate the ratios at the boundary, and after an infinite amount of time, the entire crystal will have the ratio of 0.7106. To test such a situation, I model the variations seen in crystal SS23A_tr2 from Figure 5.2. Results are shown in Figure 5.7. The initial condition, as shown by the dotted t=0 line will be a flat profile throughout the crystal, with a composition of the core. At the crystal boundary, the profile will sharply rise to the magma composition of 0.7106. In the first instant after diffusion begins, the composition at the crystal edge will rise to equal the composition of the magma, but the core would remain unchanged. Profiles after various timescales are shown in Figure 5.7. It is clear that no matter what the diffusion timescale, the flat profile from the crystal edge to ~700 microns into the rim cannot be replicated under these

conditions. This boundary condition is clearly not applicable to model diffusion in the Thalghat GPB crystals.

Case 5: Lower initial core ratio

In the situations so far, the core was assumed to have an initial composition similar to the measured near-homogenous core compositions. However, once rim growth and therefore diffusion begins, there is no reason for the core composition to remain constant, i.e. the core composition is not a fixed boundary condition. In fact, if diffusion continues infinitely, the final composition of the crystal will be a homogenous flat profile that has the composition of the rim. In order to test the possibility that the initial core composition could have been different, I consider a special case of the profile SS23A_tr2 from Figure 5.2, where the initial core $^{87}Sr/^{86}Sr$ value is taken to be lower than 0.7096, and assume that diffusion has acted to raise the core ratio to the measured value. I investigated this by modeling the diffusive re-equilibration of $^{87}Sr/^{86}Sr$ assuming a lower initial core $^{87}Sr/^{86}Sr$ ratio of 0.7095.

Figure 5.8 shows the initial profile as well as a calculated profile at t = 600 years that fits the core compositions. While the 600 yr profile matches the measured core ratios, the measured rim compositions are well above the calculated values; that is, a proper fit cannot be obtained simultaneously for the core and rim. Therefore, the possibility of a lower initial core ratio is ruled out.

Case 6: Non-constant boundary condition due to diffusion in the melt

So far, we have assumed the rim of the crystal to be in equilibrium with the melt, so that crystal-melt diffusive exchange is minimal to non-existent. This condition can be

met if the melt surrounding the crystal is frequently replenished by vigorous convection. Here I consider the implications of diffusive exchange between the crystal and melt. Diffusion in melt is much faster than in crystals, e.g. at 1200 °C, $D_{Sr} = 10^{-11} m^2.s^{-1}$ in basalts (from Brady, 1995) and $\sim 10^{-17} m^2.s^{-1}$ in An64 (Cherniak and Watson, 1994; Giletti and Casserly, 1994). Figure 5.9 shows a schematic of a crystal in contact with a melt of differing composition. The initial profile across the crystal melt interface will be a step (dotted line in Figure 5.9). Over time, diffusion will act to smooth out this profile. The degree of smoothing will vary in the melt and crystal. Diffusive distance is related to D by the expression $x \approx \sqrt{D_{Sr}t}$, and because of larger Ds of elements in melt, the diffusive front will travel further into the melt than into the crystal after the same amount of time (Figure 9 bottom). The crystal-melt boundary, i.e. the outermost edge of the crystal, will have a composition intermediate between the magma composition and the crystal core composition. Therefore, the crystal edge cannot be considered a fixed boundary.

If the measured Sr-isotope profile in TGPB crystals has been affected by diffusion in melt, then the crystal core, rim and melt Sr-isotope compositions will be as shown in the bottom graph in Figure 5.9. The concentration will show a sharp dip at the crystal edge, flattening out at the core. This profile will be similar to the profiles obtained in Case 4, shown in Figure 5.7. Measured data, however, show a different profile, having nearly constant values up to ~700 microns from the crystal edge. This non constant boundary condition can therefore be discounted. Also, if melt $^{87}Sr/^{86}Sr$ composition changes by diffusion, the major element composition of the melt would also change, since most elements have D of $\sim 10^{-10} - 10^{-11} m^2.s^{-1}$ in a basaltic melt (Brady, 1995; LaTourrette et al., 1996). Variations in melt concentrations would cause variation in

major and trace elements in the crystal, which is not seen. It appears from major element zoning that melt replenishment was rapid, and the depletion was minor. Higgins and Chandrasekharam (2007) calculate a mass transfer Peclet number and a thermal Peclet number for crystals growing in convecting magma and conclude that transport of both matter and heat around a growing crystal take place by advection. They further attribute the tabular shape of Deccan GPB crystals to growth in a strongly advecting medium i.e. a "well stirred" magma. Depleted melt surrounding a growing GPB crystal can therefore be assumed to be rapidly refreshed, and that $^{87}Sr/^{86}Sr$ (and major and trace element composition) in the melt has stayed constant while the crystals were growing.

Case 7: No diffusion but mixing

In Case 0, the crystal growth during rapid magma mixing was considered, without the influence of diffusion. In the remainder of the situations considered, the initial step function was maintained, with the added effect of diffusion that acted to produce the zoning profiles seen in the crystals. The last situation I will consider is of zoning due to growth from a magma whose composition has changed along a mixing line between end members. The difference here is that the zoning does not appear as a step function, but as a series of smaller steps that define a nearly straight line compositional gradient in the crystal (Figure 5.10). The ~400 micron core-rim zone boundary (Figure 5.2) will therefore not be a diffusion zone, but a mixing zone. As mentioned earlier, this situation can occur if the crystal is growing in a magmatic mush zone, where the liquid proportion is ~50%. This situation may also occur if crystal growth rate is much faster than the rate of magma homogenization.

90

Whether the zone boundary is diffusion related or growth related cannot be unequivocally resolved with the present dataset. It is possible that closer spaced tracks with a beam diameter less than the 80-micron laser beam used could better define the zoning profile, enabling us to obtain a straight mixing line or a curved diffusion profile. If the profile is taken to result from mixing rather than diffusion, then diffusive timescales would be vanishingly small. This would mean that growth far surpassed the diffusion rate, and that the residence time was too small to allow for diffusion. Treating the profiles as diffusion profiles enables us to calculate a more conservative rate, and enables us to match diffusion and rim growth timescales, allowing for calculation of crystal growth rates.

One straightforward way to check if profiles are diffusion related is to compare orthogonal profiles across the width and length of a crystal section. These crystals have a 1:8 aspect ratio, and growth along the b-axis direction was slower, leading to the shortening of the crystals along this direction (Higgins and Chandrasekharam, 2007). So if the zone boundary has a thickness of 100 microns in the short directions, it would have a thickness of 800 microns in the long direction, which is what we see in the CL images of these crystals (see Figure 5.11). Now if Sr- isotope variations were due to mixing, then the distance over which the isotopes vary at the zone boundary should also conform to the 1:8 aspect ratio. Figure 5.11 shows a comparison between transects along the short and long directions in crystal SS23A_tr2. The graph in Figure 5.11 shows Sr-isotopic variations across the zone boundary in orthogonal directions. The thickness of the zone boundary is the same in both cases, ~400 microns. Therefore the variation in the zone boundary of these crystals cannot be due to growth from a mixed melt. It is therefore

91

reasonable to assume that the zone boundary variation was due to diffusion, and that the initial condition was a sharp step profile, which then was smoothed out by diffusion.

Diffusion model results

Based on the elimination of diffusive conditions, can assume that diffusion occurred as described in Case 3 above, where diffusion began immediately after rim growth was initiated. We can then diffusively model intracrystalline diffusion between the core and the rim of zoned TGPB crystals, at a constant temperature of 1100 °C. Diffusion in zoned crystals can be modeled using the 1-dimensional diffusion equation:

$$\frac{\partial C}{\partial t} = D_{Sr} \frac{\partial^2 C}{\partial x^2}$$

where C is the $^{87}Sr/^{86}Sr$ ratio, x is distance in meters and t is time in seconds. In this study, D_{Sr} is the self-diffusion constant for strontium in plagioclase rather than the elemental or chemical diffusion constant. Sr elemental concentrations are near homogenous throughout the crystal, and so there would be no chemical potential over which chemical diffusion would take place. Diffusion will therefore occur by ^{87}Sr and ^{86}Sr moving across the zone boundary by random walk. A similar effect has been demonstrated by in diffusion experiments. LaTourrette et al. (1996) used glass-glass diffusion couples of similar major element compositions but differing isotopic compositions. After the experiments, they found that MgO content was constant over the interface, but measured profiles of the isotope ^{25}Mg showed a well-defined diffusion profile (Figures 3 and 4 of LaTourrette et al., 1996). The data measured on the Thalghat crystals shows a similar effect, where core and rim Sr trace element composition is nearly constant, but $^{87}Sr/^{86}Sr$ shows a clear difference (Chapter 4, Figures 4.5 and 4.6).

Using data from Gilleti and Casserly (1994), and Cherniak and Watson (1994) I

obtain a calculated average D_{Sr} of 6.27×10^{-18} $m^2.s^{-1}$ for An64. I assume that both isotopes

of Sr have the same diffusivity. I assume that diffusion across the zone boundary can be

treated as diffusion in a semi-infinite medium. I also assume that temperature does not

change much during the diffusive timescale, which is borne out by the constant An

content and lack of major dissolution features. Using a step initial condition (dotted lines

in Figure 5.12), and fixing the boundary conditions at the edge of the rim to 0.7106,

which is the groundmass and whole rock value, I modeled diffusion numerically using

finite difference methods. Numerical modeling allows for calculating diffusion without

holding the core value steady, a condition that is closer to the natural scenario.

Because plagioclase shows significant directional anisotropy in its physical

properties (e.g. Smith, 1974), profiles along the length should be more elongated than the

profile along the width, since diffusion should act faster along the length for the same

timescale. However, many workers have noted the lack of diffusive anisotropy in

plagioclase for Sr (Giletti and Casserly, 1994), and also for Na, Ca and Fe (Behrens et al.,

1990). Cherniak and Watson (1992) note the lack of diffusional anisotropy in orthoclase

feldspar, but also note an order of magnitude difference in plagioclase feldspar diffusivity

D_{Sr} with the diffusion along the c-axis faster than that along the b axis (long and short

dimensions respectively in the above figures). Since diffusion distance x is related to D

and time by the expression $x \approx \sqrt{D_{Sr}t}$, an order of magnitude variation in D would lead

to a half order of magnitude (factor of 5) difference in diffusion distance, time remaining

constant. Comparison of orthogonal profiles in Figure 5.11 shows no difference in the diffusion distance, so here I assume isotropic diffusion throughout the crystal.

Results of the diffusion models are shown in Figure 5.12. The initial "square wave" condition is shown by dotted lines. Dashed curves are calculated profiles at various timescales. The best-fit profiles are profiles corresponding to t=200 years and t=150 years for crystals SS23_tr1 and SS23_tr2 respectively. Note that the dashed lines, which represent profiles at ± 50 years from the best fit, are not too different from the best fit profiles. It must be assumed that the calculated time has a ± 50 year error. At 1100° C, the largest timescale we obtain is 200 years for diffusive equilibrium.

Calculation of crystal growth rates

The calculated diffusion duration for relaxation of Sr-isotope profiles is 200 years at 1100° C and as noted above, this time is the same as that of rim growth, therefore the rim growth duration is also 200 years. The width of the rim, from the figure above is ~0.8 mm, on each side of the core and the combined width of the rim is then 1.6mm. As stated before, the crystals have an aspect ratio of 1:8, and this gives us a lengthwise rim thickness of 12.8mm. This lengthwise total rim thickness of 12.8 mm and the 200-year duration of rim growth gives us a rim growth rate of 2.03×10^{-10} cm.s^{-1}. This lengthwise growth rate can be compared to growth rates obtained from other studies, and it agrees well with data from natural measurements on Hawaii and Kamchatka, as well as some experimental results (see Table 5.1).

The rim growth rate we have calculated should be considered the mean growth rate, since it is likely that growth rates varied in the magma chamber over time. From the

small variability of major element composition, the lack of dissolution boundaries, and the chemical equibrilium between major and trace element compositions in Thalghat plagioclase (see previous chapter), it appears that growth conditions were uniform. Therefore, variations in crystal growth rates were likely small in magnitude. Diffusion modeling does not allow the calculation of the growth rate of the core or the growth rate of the non-zoned crystals. It can however be assumed that non-zoned crystals shared the same history as the rims of the zoned crystals owing to the similarity in major, trace element and isotopic compositions. The core of the crystal had a separate history, although it does share similar major and trace element compositions, and likely had very similar growth conditions. I assume here that non-zoned crystals and zoned cores grew at the same rate: the calculated rim growth rate of 2.03×10^{-10} cm.s^{-1} at 1100° C.

Implications for Deccan eruptive rates

Using the Deccan-specific growth rate calculated above we can calculate residence times for all TGPB crystals. Assuming a maximum crystal size of 5 cm, we calculate $(2.03 \times 10^{-10}$ cm.s$^{-1}) \div (5$ cm$) = 781$ years as the growth time of the crystal, which is also the residence time, assuming uninterrupted growth.

We can apply this timescale to all the flows that these crystals have been in equilibrium with. The core of the TGPB crystals are not in equilibrium with any underlying flow, though the ratio is in between that of the TGPB lava and the immediately underlying flow, as described in the previous chapter. The thickness of the TGPB flow (SS23) is 80 m and that of the underlying flow (SS22) is 20 m. We can directly relate the incubation and eruption of the 80 m thick TGPB to the residence time

of the crystals and obtain a 1-dimensional eruption rate of 0.1 m.y^{-1} for the TGPB. If we

assume that the TGPB was also in equilibrium with the magma of flow SS22, we can

apply the timescale to both the GPB and the underlying flow, obtaining a rate of 0.13

m.y^{-1}. Ideally, one would calculate a volumetric rate, but there are no estimates of flow

volumes for most of the Deccan Western Ghats lavas, especially for the older formations

as the outcrops are limited and most are overlain by younger formations over a large area

of the Western Ghats.

The Keshele GPB shows more complicated zoning patterns, but an interesting

aspect is that the crystals hold evidence of having been in equilibrium with at least two

underlying lava flows, and may have been growing throughout the life cycle of the

Igatpuri Formation. Residence times of the KGPB would therefore give the eruptive

duration of the entire 220 m thick Igatpuri Formation. Unfortunately, because of

dissolution boundaries, the residence times cannot be known for sure. Close to the crystal

edge, KGPB crystals show a smooth change in ^{87}Sr/^{86}Sr from 0.7112 to 0.7096. This

variation is seen in both the lengthwise and widthwise transects, however the variations

occur over very different length scales in these directions. The variation takes place over

~2500 microns and ~400 microns in the lengthwise and widthwise directions

respectively, and if these variations are modeled as diffusion profiles, this gives us 1500

years and 70 years respectively. Sr self diffusion is close to isotropic in plagioclase

(Giletti and Casserly, 1994), so this large difference in timescales could mean rapid

growth from a varying melt composition and a short diffusion timescale (as noted in Case

7). So at least the outer 3 mm of the crystal can be said to have grown faster than the

calculated rate for the TGPB, assuming that the homogenization rate of the mixed magma

is the same in both cases. Keshele GPB crystals have similar sizes as the TGPB crystals, so if we assume a 5cm crystal and use our calculated growth time of 781 years, we get a 1-D rate of 0.28 $m.s^{-1}$ for eruption of the KGPB.

The results show that it is possible, using diffusive equilibration modeling, to obtain crystal growth rates that are appropriate for a particular magmatic system, and the method has the potential to calculate incubation + eruptive timescales for the host lava flows. This study represents a refinement of the earlier work by Sen (2001) and Sen et al. (2006). Similar studies on other formations over the stratigraphic extent of an igneous province can provide a total euptive timescale for the province. If we use an eruptive rate of 0.1 m/y for the entire 2.7 km thickness of the Western Ghats, we obtain a timescale of 27,000 years for the duration of Western Ghats activity. Different authors have different estimations of Western Ghat thickness; a recent study by Chenet et al. (2007) use 3.5 km as the thickness. Calculated duration could then be up to 35000 years. This timescale would of course be more rigorous if we calculate and average separate eruptive rates for other flows in the Deccan Western Ghats section. It is clear however, that this technique has the potential to constrain eruptive durations better than any present radiometric method.
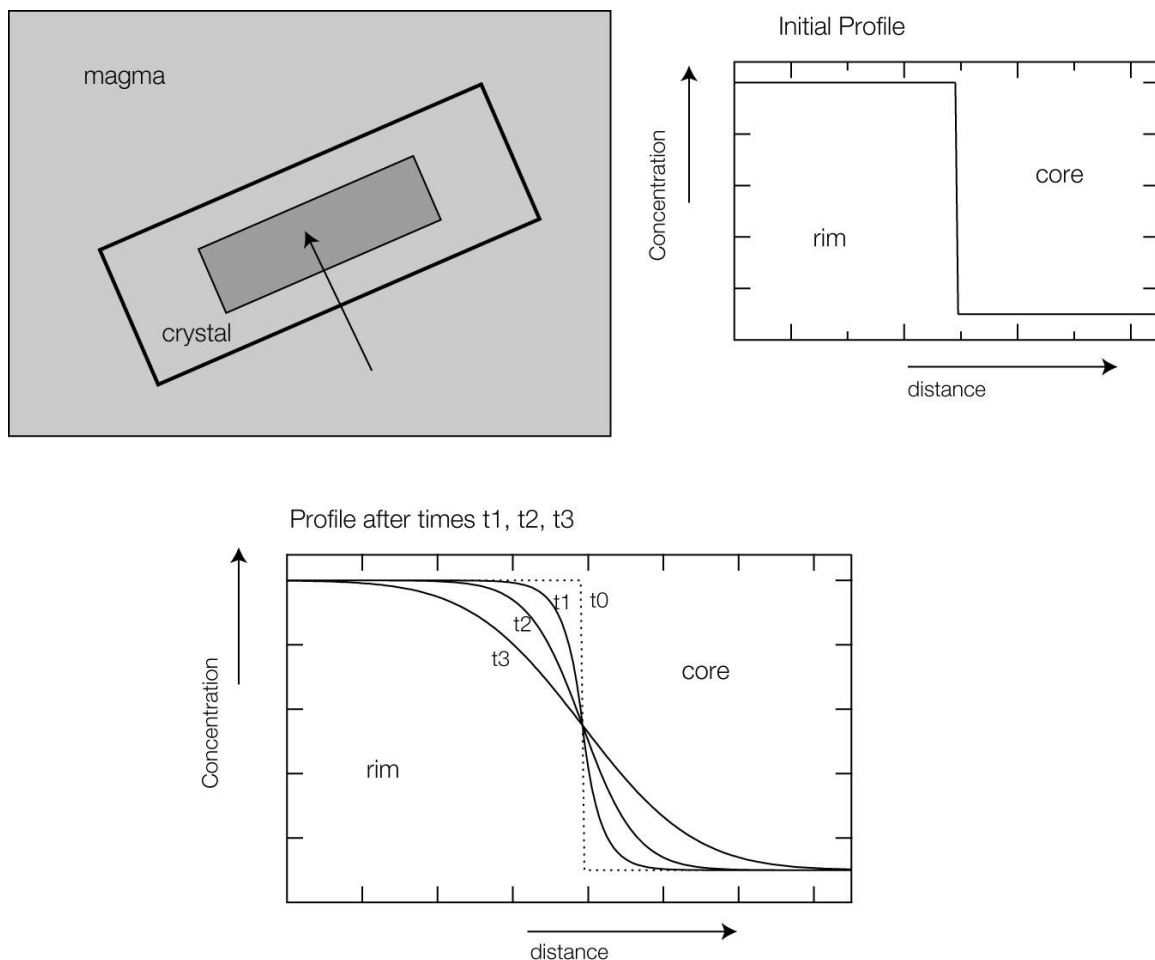
Figure 5.1. Schematic of crystal growth and diffusion. Top left: A typical zoned crystal growing in a magma chamber. The core and rim have different concentrations, denoted by the two shades of gray, and here the crystal is shown growing in a magma with the same composition as the rim. The core may have grown separately and transported into the magma chamber, or conversely the composition of the magma in the chamber could have changed, giving rise to the abrupt change in composition between the core and rim. Either condition would give rise to the profiles depicted. A concentration profile measured from rim to the center of the core along the arrow is shown in the adjacent graphs. **Top right:** this is the initial profile after crystal growth, but before diffusion. In this model, the core is assumed to have a lower concentration than the rim. Here, the time taken for crystal growth is negligible, i.e. it has no effect on the initial profile. **Bottom:** The initial concentration profile (dotted) which has a sharp jump in composition, will gradually smoothen out over time. Three profiles at subsequent times t1, t2, and t3 are shown.
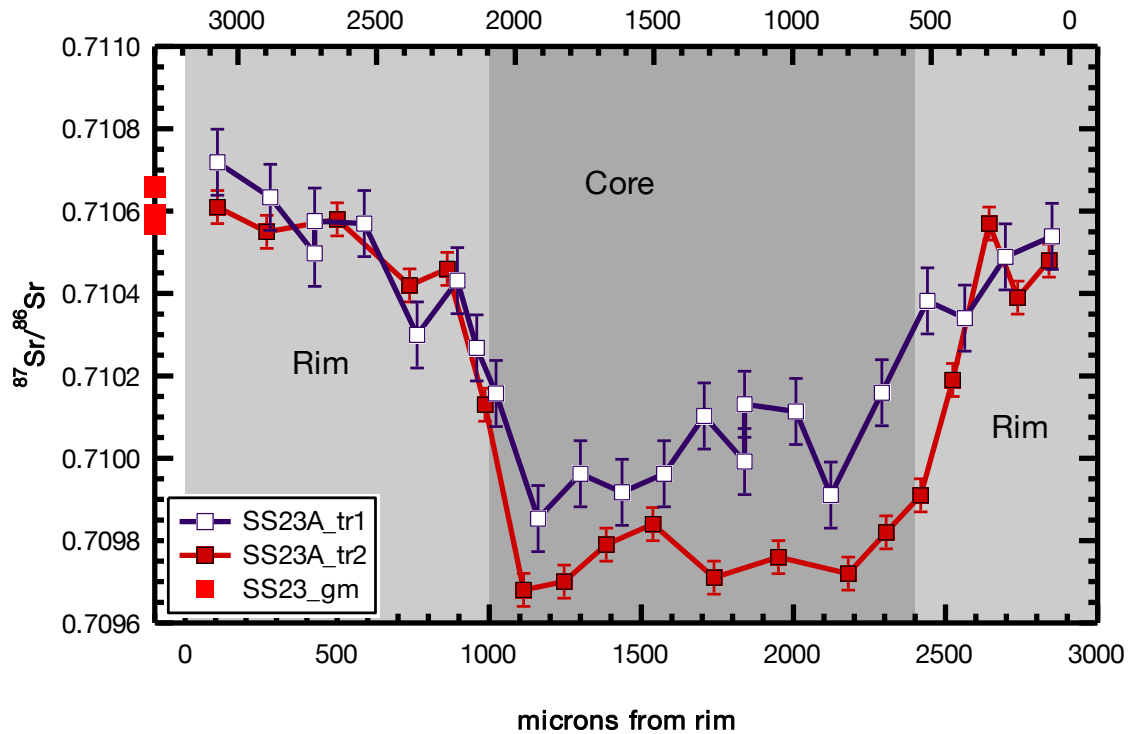
Figure 5.2. ^{87}Sr/^{86}Sr variation in zoned crystals from the Thalghat GPB. Filled squares are from crystal 1 and open squares are from crystal 2 in Figure 5.1. Red squares on the left x-axis are groundmass plagioclase ^{87}Sr/^{86}Sr values. The core and rim zones are labeled and shown in light grey, while the intermediate zone between the core and rim is shown by a darker shade of grey. Note the shape of the zoning profile: the core zone is more or less even, if the small variations are discounted; and the rim zone can be considered flat from the crystal edge to the zone boundary. The presence of within-core and within-rim variations cannot be completely discounted, but in this case, the variations are not much larger than the error in ^{87}Sr/^{86}Sr.
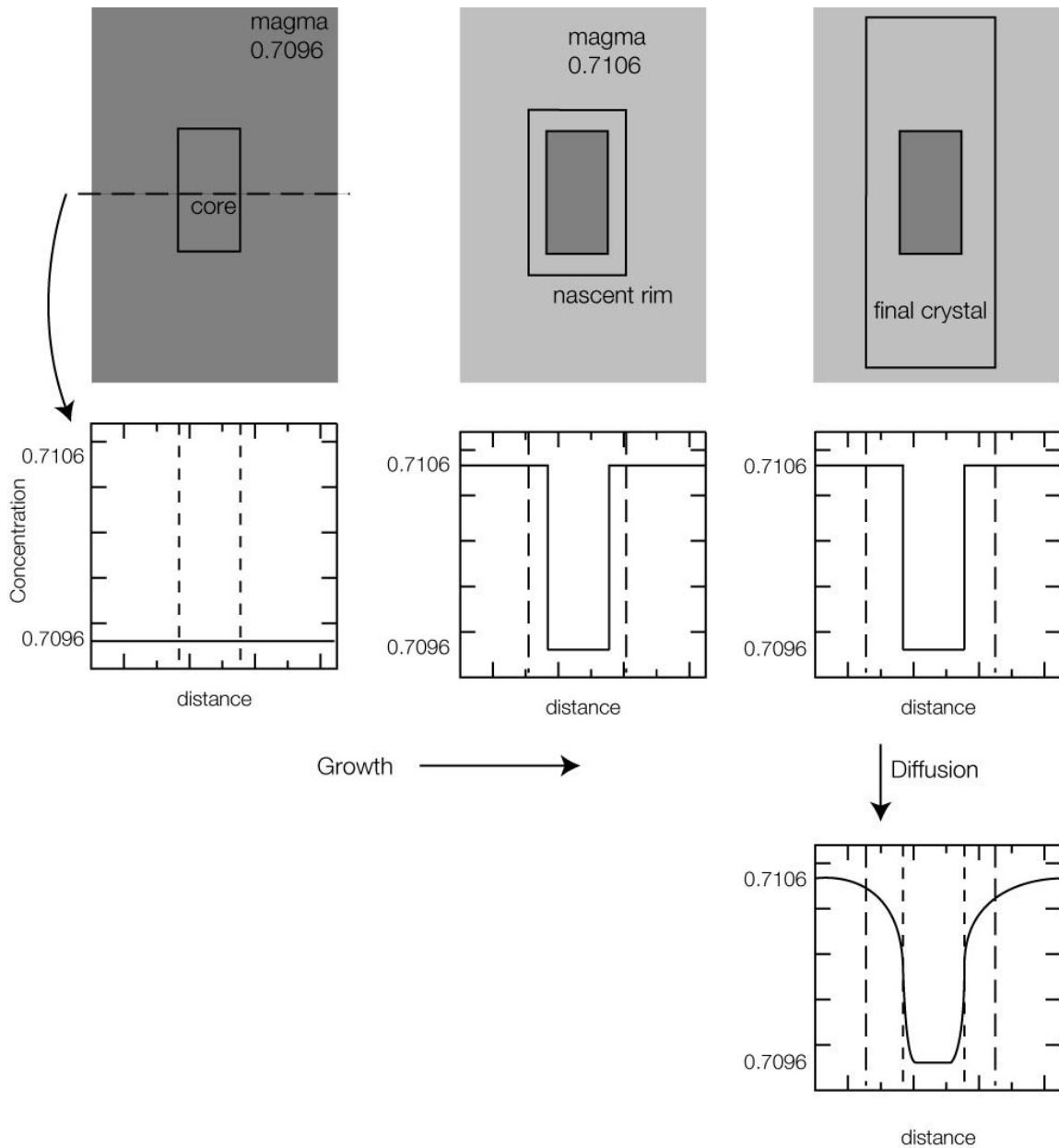
Figure 5.3. Schematic showing decoupled growth and diffusion. Top row: crystal growing in a magma chamber, left to right: core growth, initiation of rim growth and final crystal. Middle row: transect across the center of the domain in the upper figure (dotted line in the top left diagram). Dotted lines are outlines of the crystal; solid lines are $^{87}Sr/^{86}Sr$ concentration profiles. Bottom row: Profile after diffusion has acted for a certain time.

100
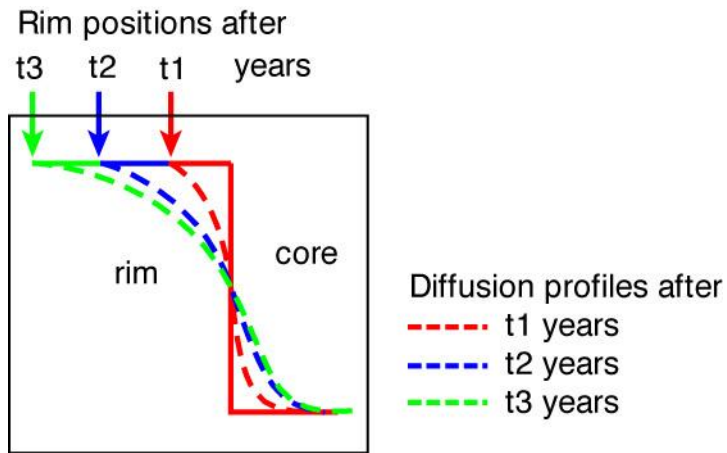
Figure 5.4. Compositional variations resulting from interfering growth and diffusion processes. The figure shows an initial condition (solid line) in a growing crystal, where a rim of higher composition has just begun to form. After time t1, the edge of the crystal is as shown by the arrow. In this case, because of rapid diffusion, the initial profile will have diffusively relaxed after time t1, as shown by the dashed line, and the diffusion front will have reached the crystal edge. After time t3, the diffusion profile is seen to have affected the crystal edge.
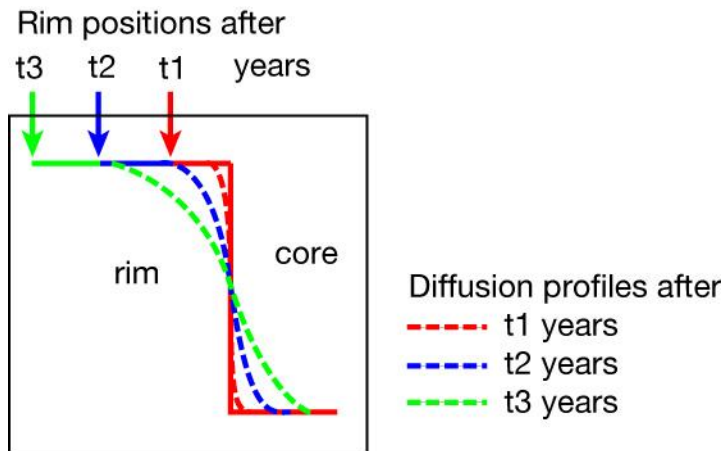
Figure 5.5. Compositional variations resulting from non-interfering growth and diffusion. This condition is similar to that of Figure 5.4, but the diffusion rate is slower. Therefore, after times t1, t2, and t3, the diffusion front does not reach the crystal edge. The final profile then shows a near homogeneous core and a near homogeneous rim, with only the core-rim boundary showing concentration variations.
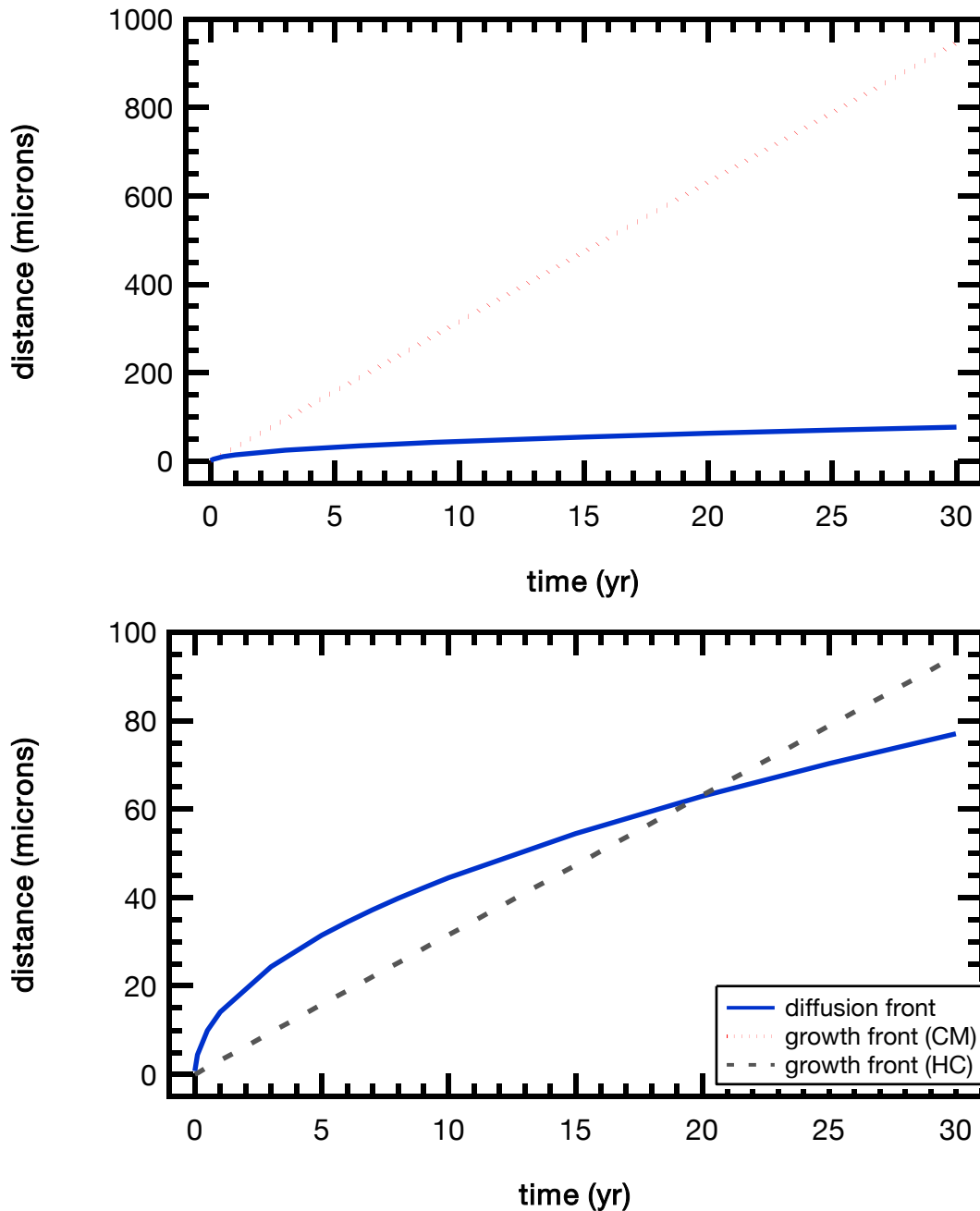
Figure 5.6. Comparison of growth rate and diffusion rate over similar timescales.
The diagrams show the extent of the growth front and diffusive front over varying
timescales. In each graph, the growth and diffusion distances are plotted on the y-axis and
the timescales in years on the x-axis. Diffusion is measured with the equation
$x \approx \sqrt{D_{Sr}t}$ where D_{Sr} is the diffusivity of Sr in plagioclase calculated at 1100 °C; x is the
diffusion distance in microns and t is time in seconds. Growth is calculated using a
growth rate of 10^{-10} cm/s from Cashman and Marsh (1988) in the upper graph (labeled
CM). In the lower graph a slower growth rate of 10^{-11} cm/s is used, which is the growth

rate suggested by Higgins and Chandrasekharam (2007) for plagioclase growth in a subsurface magma chamber. Note that this rate is much smaller than growth rates from the literature shown in Table 5.1. In the upper graph, the growth front supersedes the diffusion front almost immediately after t=0, whereas in the case of the slower growth rate (lower graph), the growth front will overtake the diffusion front after 20 years.
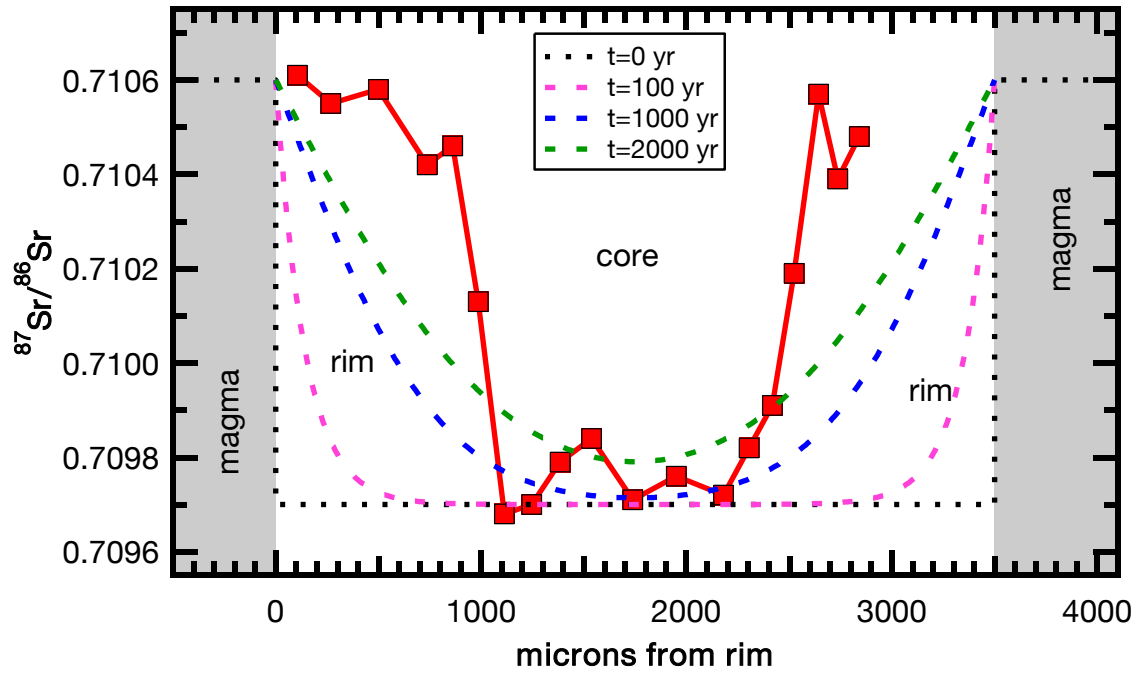
Figure 5.7. Diffusion profiles calculated assuming no initial zoning. The initial profile is shown by the dotted line at t=0. Profiles are calculated at t=100, 1000 and 2000 years. The grey area is the magma, which has a composition of 0.7106, and the white area is the crystal. $^{87}Sr/^{86}Sr$ data from crystal SS23A_tr2 is shown as solid squares. As is clear from the figure, using an initial homogeneous condition gives a concave upwards diffusion profile, anchored at the crystal edge. The profiles do not match the roughly square wave shaped profile of measured TGPB data.
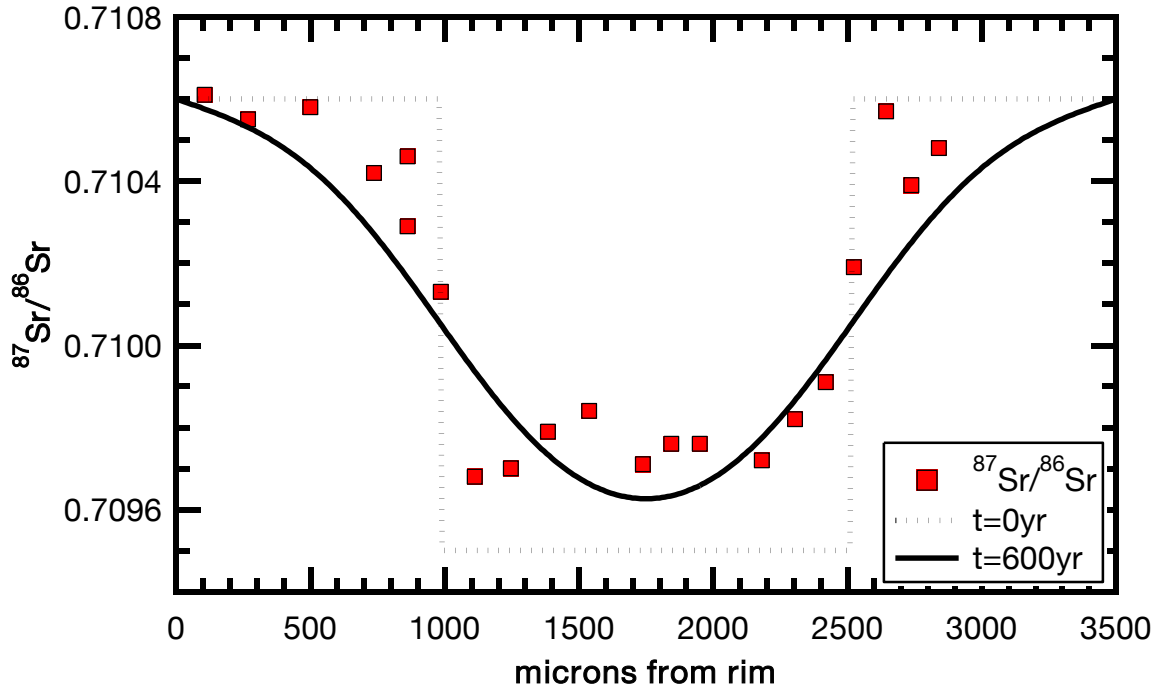
Figure 5.8. Diffusion profile calculated assuming a lower initial core composition.
$^{87}Sr/^{86}Sr$ data from crystal SS23A_tr2 is represented by solid squares. The initial condition denoted by the dotted t=0 line is taken to have a lower core value. After t=600 years, diffusion acts to raise the core compositions to fit the measured data. However, at the rim, the 600-year profile is much lower than the measured ratios; this initial condition cannot explain the measured profile.
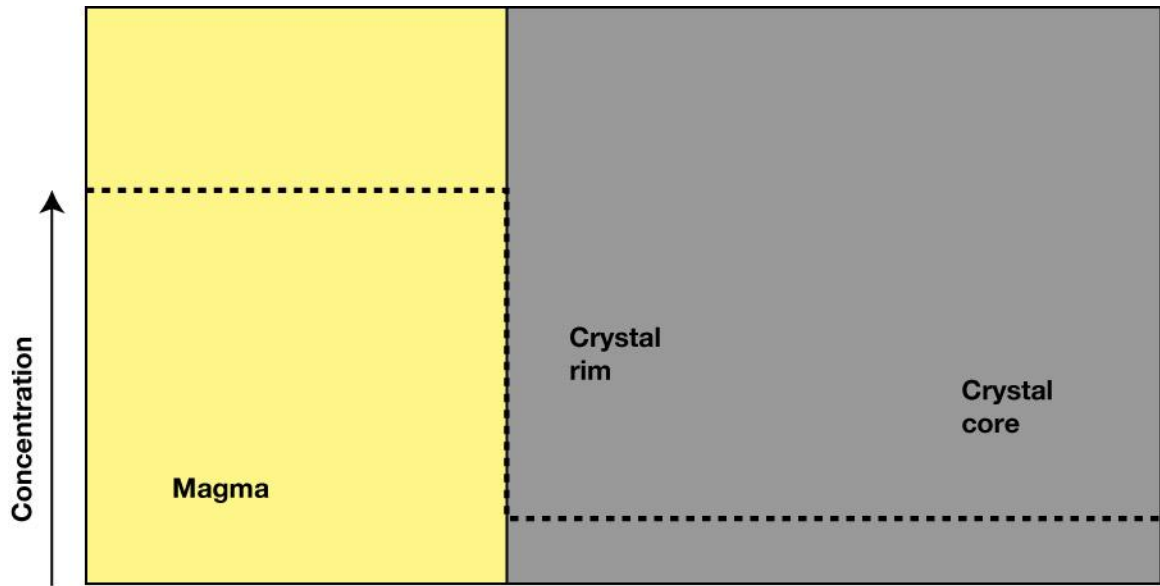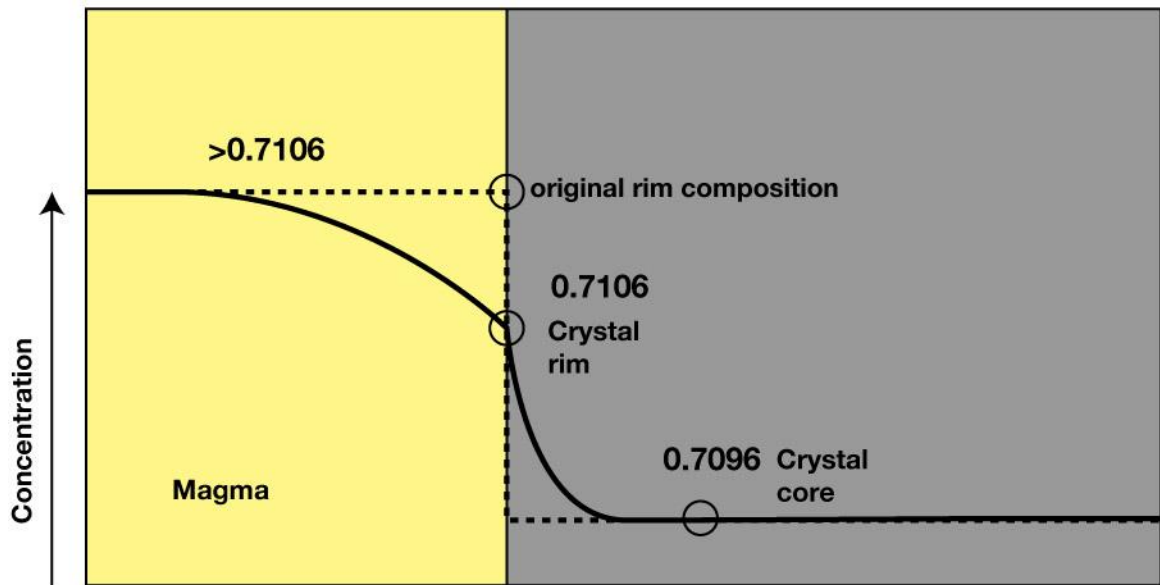
Figure 5.9. Schematic of the effect of diffusion at the crystal – melt boundary. Here the composition in the melt does not remain steady, but changes by diffusion. Since diffusion in the melt is orders of magnitude faster than in the crystal, the diffusive front in the melt extends further into the melt region than in the crystal after a time "t". The crystal-melt boundary diffusion requires that the shape of the profile show a sharp dip from the rim to the core. Such a profile is not seen in the measured data in Figure 5.2 where the ~ 700-micron rim has a flat profile, and therefore has not been affected by diffusion.
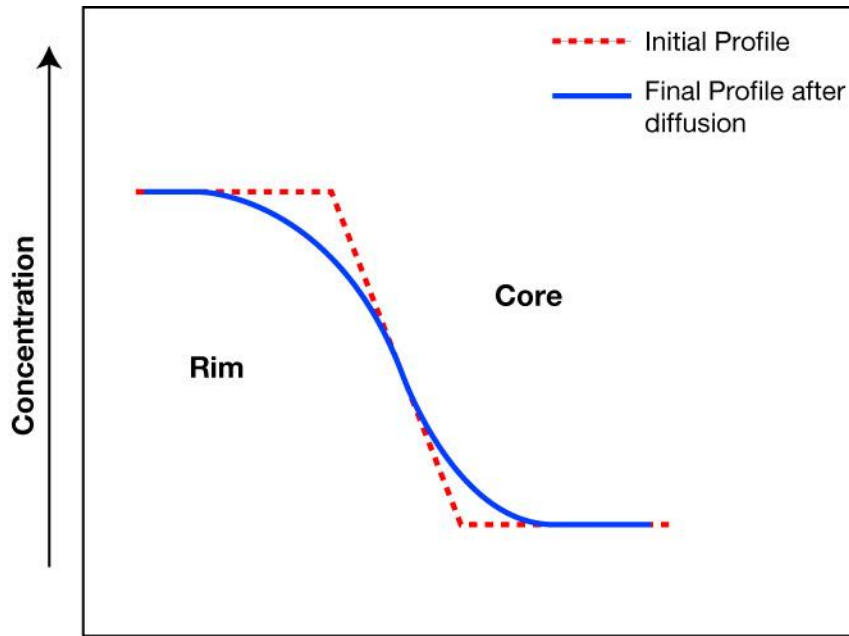
Figure 5.10. Crystal zoning profile resulting from growth within a magma of varying composition. Here the core and rim are growing from separate magma compositions, but the mixing process between the two compositions is slow, and new crystal layers growing over the core will show a smooth variation due to growth from the mixed magma. The initial condition is shown by the dotted line. Diffusion will act to smooth out the initial profile, as shown by the solid line.
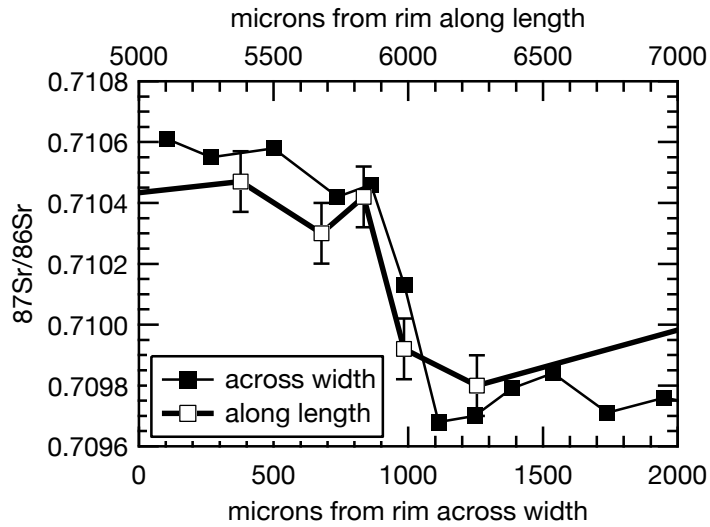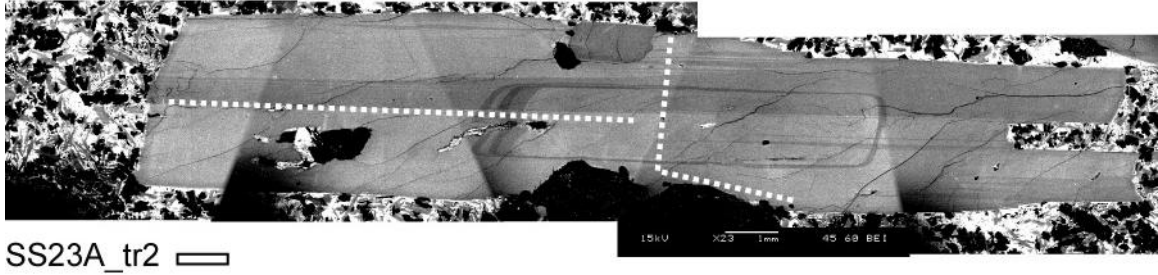
SS23A_tr2 ▭

Figure 5.11. Comparison of orthogonal zoning profiles from a single zoned crystal. The image is a CL image of Thalghat GPB crystal SS23A_tr2. The white bar at the bottom right of the image is a 1 mm scale bar. Note the clearly visible core, and the variation in thickness of the zone boundary in the two directions. Zoning profiles have been measured in two directions along the dotted lines shown in the image. The bottom graph shows isotopic variations across the zone boundaries. The upper and lower x-axes are distances from the rim, and the width represented by both axes is 2000 microns. It is seen that the distance over which isotopic values change across the width and length is the same, around 400 microns.

109
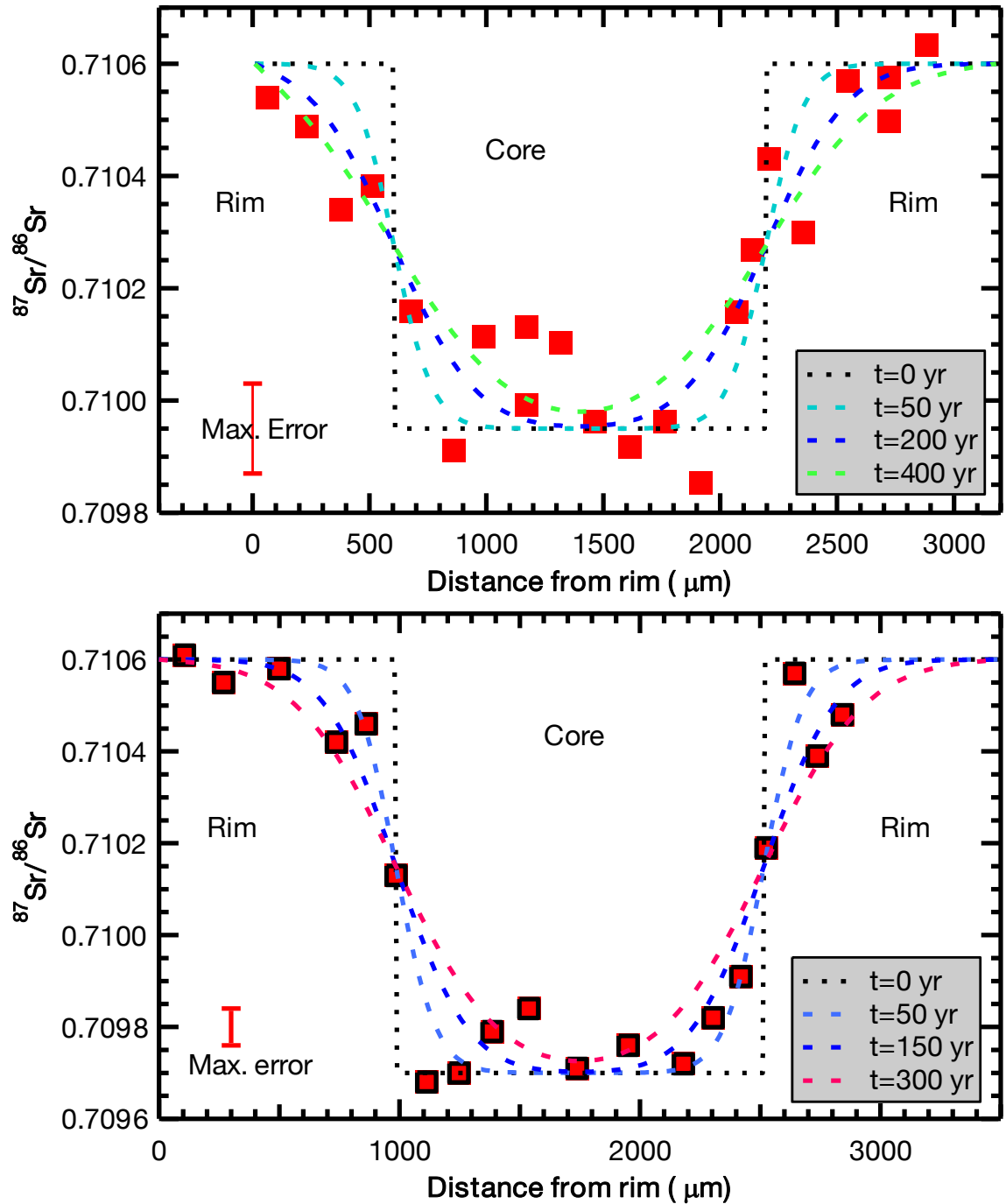
Figure 5.12. Results of diffusion modeling of Thalghat plagioclase zoning profiles.
The upper graph shows data from crystal SS23A_tr1 and the lower graph shows data
from crystal SS23A_tr2. Measured Sr-ratios are represented by solid squares. Dotted line
at t=0 is the initial condition and dashed lines are equilibration curves at various
timescales, calculated using a D_{Sr} value of 6.27×10^{-18} $m^2.s^{-1}$ at a temperature of 1100 °C.

Table 5.1. Comparison of plagioclase growth rates from this study to those from previous studies.

Reference	Growth rates $\times 10^{-10}$ cm/s	Comments
This study	2.03	Calculated from diffusive equilibration at 1100 °C
	5.07	Calculated from diffusive equilibration at 1150 °C
(Cashman and Marsh, 1988)	0.99	Direct measurement of a cooling Hawaiian lava lake
(Izbekov et al., 2002)	2.50	Measurement of crystal sizes in eruptions of known timescales from Karymsky volcano, Kamchatka.
(Burkhard, 2005)	5.37	Growth experiments on Kilauea basalt (longest duration 224 hr experiment at 990 °C)
(Larsen, 2005)	5.60	880 °C 216 hr sodic rim growth experiment
	3.50	850 °C 480 hr sodic rim growth experiment
(Kohut and Nielsen, 2004)	204.00	Growth experiments on MORB composition, 116hr at 1230 °C

The values obtained through diffusion modeling agree well with most other estimations except for the Kohut and Nielsen (2004) value, which was from an experiment at a much higher temperature.

CHAPTER VI

DISCUSSION, CONCLUSIONS AND FUTURE WORK

Deccan Magma Chambers and growth of "giant" crystals

An interesting question is what type of environment was it that allowed the plagioclase crystals to grow to "giant" sizes. Previous authors (Sen, 2001; Sen et al., 2006; Higgins and Chandrasekharam, 2007) have pondered this issue, and based on my new data, I evaluate their models and present my own hypothesis. As a starting point, it is reasonable to assume that such crystals grew in shallow crustal magma chambers since phase equilibrium studies on Western Ghat tholeiites show that fractionation occurred at relatively shallow depths of ~0.2 GPa or less (Cohen and Sen, 1994; Sano et al., 2001). A cooling magma chamber loses heat through the chamber walls and as a result develops a solidification front that advances toward the interior of the chamber with time (Figure 6.1). The solidification front is zoned in terms of the crystal and melt proportions. Crystals are more abundant towards the walls and the liquidius marks the inner edge of the front.

Marsh (1988, 1996) suggested that the part of the solidification front with crystal proportion >55% rheologically behaves like the wall rock, and the liquid entrapped in this part does not communicate with the rest of the magma chamber. The region with 25-50% crystallinity is a "mushy" region from where crystals are unlikely to migrate into the liquid rich part of the chamber. The plane of 25% crystallinity that bounds this region is called the "capture front". In Figure 6.1, crystals to the left of the capture front (25 – 55% crystals) are "non-eruptible", while crystals to the right of the front (25% - 0% crystals)

are "eruptible" in the sense that if the chamber collapses, or if a new magma batch pushes out the existing liquid-rich mass, then such crystals will erupt. As the magma chamber continues to solidify, a gradation in crystal size must also develop. The tiniest crystals would form at the liquidus edge of the solidification front, and the size of the crystals would progressively increase towards the walls (Figure 6.1). When the magma chamber is tapped, only liquid and crystals from the "suspension zone" (< 25% crystals) will be erupted.

Marsh (1996) noted that typical plagioclase phenocrysts in modern day basalts are up to 1 cm long. If all phenocryst bearing lavas originate from the suspension zone as stated above, then it can be assumed that the suspension zone generally contains crystals up to 1 cm in size. Note that the giant crystals of the Thalghat and Kashele GPB do not commonly touch each other, implying that they were brought up from a liquid rich environment in the magma chamber. However, their unusual size would require some special set of conditions in which they could grow. I explore this issue by evaluating ideas previously presented by Sen (2001), Sen et al., (2006) and Higgins and Chandrasekharam (2007)

Sen (2001) model

Figure 6.2 presents a schematic of the Sen (2001) magma chamber model for the origin of zoned plagioclase crystals (figure from Sen, unpublished). A shallow crustal magma chamber (at ~ 6 km depth, 2 kbar pressure) is continuously filled by magma supplied from the source region. Within the chamber, the magma mixes with the existing melt, differentiates and is periodically tapped, leading to the eruption of lava flows of varying compositions. The erupted flows may carry varying amounts of phenocrysts.

During the repeated replenishment and tapping processes, plagioclase crystals will continuously grow in a solidification zone that develops in the suspension zone of the magma chamber (e.g. Marsh, 1989a, 1996). As new batches of magma are introduced into the chamber, the composition of the mixed magma will change, and the growing crystals will mirror the change. Finally, there is a hiatus in magmatic activity during which the crystals continue to grow, but no eruption occurs. Instead, erosion of the older lava produces hematite rich soil ("red bole") on the surface. It is during this stage that plagioclase crystals grow to large or "giant" size. The solidification front may encroach further towards the center of the chamber, and magma compositions may continue to evolve, becoming more Fe-rich, and therefore denser. Increasing density combined with convection may cause plagioclase crystals from the melt-dominated solidification front (<25% crystals) to float near the top of the chamber. At some point the magma chamber would collapse, expelling the evolved, giant phenocryst rich magma as a GPB flow. Figure 6.2 shows an idealized giant plagioclase crystal that is internally zoned, each zone corresponding with an underlying flow expelled from the magma chamber.

Sen et al. (2006) add to the Sen (2001) model a special case where crystals grow in conduits (dikes) rather than magma chambers. They suggest the crystals form a "chicken wire network" i.e. a mesh of plagioclase crystals, through which magma is continuously flushed (Figure 6.2 b). This growth environment has the advantage of providing a continuous supply of nutrients from fresh magma, which aid the growth of large crystals.

114

Higgins and Chandrasekharam (2007) model

Higgins and Chandrasekharam (2007, henceforth abbreviated to HC) presented a model (Figure 6.3) based on the similarity of the GPB phenocrysts to plagioclase crystals from layered intrusions and anorthosite massifs. Based on crystal size distribution (CSD) and crystal textural studies, HC calculated a residence time of 600-1500 years for GPB crystals. Deccan GPB CSD plots show a cutoff in the lower limit of crystal sizes – there are no crystals < 2mm. HC attribute this to a stage of coarsening (Ostwald ripening) where no new crystals nucleated, but small crystals and nuclei dissolved and supplied the nutrients for continued growth of the larger crystals. HC noted the textural similarities between the GPB phenocrysts and anorthosite layers in upper parts of layered mafic intrusions like Sept Iles and Skaergaard. The anorthosite layers likely formed by flotation of plagioclase crystals to the top of magma chambers (e.g. Higgins, 2005) and similar processes may have affected the Deccan giant plagioclase crystals. HC proposed a three step process of GPB formation (a, b and c in Figure 6.3). Lava flows that occur beneath the GPB were transported to the surface from depth through conduits (Figure 6.3 a). The conduits were closed off at one point, and new magma accumulated in a shallow magma chamber (Figure 6.3 b). This new magma had no outlet to the surface and this stage was marked by a hiatus in eruptive activity. Erosion of existing flows would form red bole beds on the surface during this hiatus. HC suggested that the magma chamber would form at the base of the erupted lava pile – a much shallower level than that suggested by Sen (2001) on the basis of phase equilibria. The thickness of the Jawhar Formation has not yet been accurately estimated as its bottom boundary is beneath the surface. Samples collected in this study give a thickness of 220 m for the Igatpuri and >150 m for the

Jawhar. Peng et al. (1994) give the combined thickness as >700m. If the giant crystals did grow in a magma chamber at the base of this erupted pile, then the pressure at that depth in the HC model would be ~ 0.3 kbar. Plagioclase crystals would nucleate and grow, and eventually collect at the roof of the chamber by convection. When another conduit is opened to the surface, or the pre-existing conduit remobilized, the crystal laden contents of the chamber will erupt as GPB flows (Figure 6.3 c). Following this, the magma chamber is abandoned, and later flows are transported to the surface from depth as in Figure 6.3 a

Comparative evaluation of previous models: Further discussion and a new model

There are notable differences between the models of Sen (2001) and HC (2007). Sen (2001) considers GPB eruption as the culmination of a magmatic cycle, while HC consider the GPB eruption to be the start of a new magmatic cycle. The Sen (2001) model will lead to the formation of zoned plagioclase crystals owing to the passage of multiple compositionally diverse melts through the same magma chamber that the crystals grew in. The HC model does not explicitly allow for the passage of different magmas through the chamber: growth of the GPB is confined to the chamber below the lava pile, and all other flows bypass this chamber.

I summarize the similarities and differences between the Sen (2001), Sen et al. (2006) and HC models as follows:

1. Both models require that the giant crystals form in shallow magma chambers. The Sen (2001) model suggests formation of these crystals around 0.2 GPa while the HC model prefers a much shallower depth. There is no constraint on the depth of such a

magma chamber other than the fact that the Western Ghats tholeiites all plot at the 0.2 GPa plagioclase+olivine+augite+melt pseudocotectic (Sen, 1995).

2. One of the similarities between the models is in that both require accumulation of plagioclase crystals in Fe-rich differentiated liquid near the roof of the magma chamber. The HC model calls for active convection currents in the magma chamber that will sweep the lighter plagioclase crystals towards the roof. Whether or not convection can occur in a differentiated magma chamber is an issue of dispute (Marsh, 1989b; Huppert and Turner, 1991). Marsh suggests that convection in magma chamber is sluggish or nonexistent, except in ultramafic intrusions (e.g. Duke Island Irvine, 1987). Another problem with flotation is that the cooler, denser Fe-rich melts, in which the plagioclase crystals would accumulate, should sink in the magma chamber. Yet another problem is the manner in which the crystals occur in the erupted lava. HC indicate that they occur in clusters, but within each cluster the crystals are sharply angular to each other. In layered intrusions in which plagioclase flotation has been invoked, crystals conspicuously touch each other and are sub parallel to each other, a texture termed "igneous lamination" (Hess, 1960). My own examination of the GPB flows in the field (see the field photo - Figure 1.4) indicates that the crystals have little to no layering and rarely touch each other, suggesting an origin in a melt dominated environment, and not in an environment where crystals would align themselves by flotation and accumulation. The role of plagioclase flotation in the origin of the giant crystals would therefore be minor.

3. An important observation by HC is that plagioclase crystals <2mm in size do not occur among the "giant" plagioclase. They therefore proposed that these crystals grew by Ostwald ripening processes after accumulation by flotation. Studies of layered intrusions suggest that such processes generally result in the development of adcumulus texture (e.g. Higgins, 2005). HC proposed that such continued growth occurred due to supply of nutrients from dissolving smaller crystals. In the case of GPB, individual plagioclase crystals are euhedral, and show little evidence of adcumulus growth. If Ostwald ripening did affect the giant plagioclase crystals, it probably was not accompanied by segregation of the crystals by flotation.

The present study provides minute details of intracrystalline variations in elemental chemistry and Sr-isotope ratio, and therefore introduces crystal chemistry as a further constraint to crystal growth processes. Based on the new information I present a new model for giant plagioclase formation.

Effect of volatiles on crystal growth

The presence of volatiles can enhance crystal growth rates, leading to large crystal sizes as seen in the large crystals from volatile-rich, pegmatitic liquids. While the effect of volatiles cannot be fully discounted, it may not be the sole reason for the growth of large crystals as Deccan lavas, and flood basalt lavas in general, do not have large amounts of dissolved water. Water contents of ~0.6% have been measured in melt pockets within phenocrysts in Deccan Basalts (Sano et al., 2001). Amount of water in basaltic magmas will increase with pressure and it may be argued that giant crystals grew at depth, where the GPB magmas had more dissolved water. This effect may however be

buffered by lower growth rates at high pressures. Growth in water-saturated conditions would not support the argument of HC that the plagioclase grew in extremely shallow chambers. The effect of water would also be to increase the An content of crystallized plagioclase (e.g. Panjasawatwong et al., 1995). This is not supported by the measured An content of plagioclase from GPB flows, which are the lowest among the flows of the Jawhar and Igatpuri. It can therefore be concluded that these crystals could not have grown in shallow chambers under water-rich conditions.

Growth of Thalghat GPB

The presence of zoned and non-zoned plagioclase in Thalghat GPB can provide further constraints to test the models. As stated in previous chapters, zoned Thalghat GPB shows a near-homogeneous core with $^{87}Sr/^{86}Sr$ of ~0.7096 – 0.7098 and a near-homogeneous rim with $^{87}Sr/^{86}Sr$ 0.7106. Unzoned Thalghat plagioclase, which form the majority of the phenocrysts, have $^{87}Sr/^{86}Sr$ of ~0.7106. There is no size difference between zoned and unzoned crystals, nor are there major, trace element, and isotopic differences in the zoned crystal rims and unzoned crystals.

Growth of zoned plagioclase could have occurred in two ways: 1) growth of the core and rim in the same magma chamber, by an influx of magma with a different Sr-isotope composition, or 2) by transport of crystals between two magma chambers, each with a different Sr-isotope composition. In the first case the following would be the series of events that would occur:

1. The magma chamber originally contained magma with $^{87}Sr/^{86}Sr$ composition of 0.7096, containing some proportion of plagioclase phenocrysts.

2. Another magma intruded into this chamber, the $^{87}Sr/^{86}Sr$ of this would be >0.7106 and the mixed magma would have the composition of 0.7106.

3. New crystals nucleated in this mixed magma, and grew as unzoned crystals with a composition of 0.7106.

4. Simultaneously, new layers grew onto pre-existing crystals with $^{87}Sr/^{86}Sr$ of 0.7096 forming zoned crystals.

Assuming that growth rates in the mixed magma were constant for all crystals growing in it, the zoned crystals would be the largest sized crystals, owing to a pre-existing rim. This is not found to be the case. If the input melt contained crystals, then this size difference would not exist. However, since the input melt has to have a $^{87}Sr/^{86}Sr$ higher than 0.7106, there would exist two kinds of zoned crystals, those having cores with $^{87}Sr/^{86}Sr$ greater than 0.7106 and those with cores of $^{87}Sr/^{86}Sr < 0.7106$. This is also not observed.

The origin of this zoning is best explained by a magma of $^{87}Sr/^{86}Sr$ 0.7096 carrying plagioclase phenocrysts intruding into a magma chamber with a $^{87}Sr/^{86}Sr$ composition slightly higher than 0.7106. The proportion of two magmas is important, because the end result has to be a magma with a composition of 0.7106. The volume of magma with $^{87}Sr/^{86}Sr$ of 0.7096 has to be negligible to ensure such a resulting mixed magma composition. This is borne out by the volumetrically insignificant amount of plagioclase with $^{87}Sr/^{86}Sr$ 0.7096 (i.e. crystal cores) in the total crystal population. Only two out of 16 crystals studied showed zoning. While the crystal proportion does not necessary correspond to the magma volume proportion, it must be noted that the extreme

similarity of major and trace element compositions in the plagioclase core and rim suggest that the major element compositions of the two magmas were similar. Therefore, at a certain temperature, the magmas would have the same proportion of phases crystallized, assuming equilibrium conditions prevailed. Therefore the phase ratio can be taken to be a reflection of the magma ratio. The addition of 12.5% of magma with $^{87}Sr/^{86}Sr$ of 0.7096 to a chamber with $^{87}Sr/^{86}Sr$ 0.7106 would result in a mixed magma with $^{87}Sr/^{86}Sr$ of ~0.7015, similar to the measured ratios in groundmass from the Thalghat GPB flow. The mixed population of Thalghat crystals could therefore have grown in a steady-state magma chamber, and the only disruption to this steady-state was the introduction of ~12.5% of crystal bearing magma with a differing composition. This is schematically illustrated in Figure 6.4. Note that magma homogenization after this mixing event would be rapid, as the crystal core-rim interface shows a sharp change in $^{87}Sr/^{86}Sr$, and it has been shown in the previous chapter that this variation cannot be due to growth in a variable magma composition.

Kashele GPB crystals require a different mode of formation. We have seen in Chapter IV that different zones in the Kashele GPB correspond to different flows from the Igatpuri Formation, and the relative age of the flow corresponds to the relative age of the corresponding crystal zone. The growth of the Kashele crystals therefore coincided with the magmatic activity that resulted in the eruption of Igatpuri flows. There are a number of features that require further explanation. Most important is the fact that Igatpuri flows are more mafic than the Jawhar flows, and the Mg# increases with $^{87}Sr/^{86}Sr$. Therefore An content of the plagioclase should have been higher than An60, closer to the An63 or even An75, as seen in plagioclase from the Igatpuri flows. This is

not the case . If the flows originated from a single magma chamber, and if GPB crystals also grew in the same magma chamber, then the final crystal population should contain a mixed population of crystals of different An contents. This is also not the case. One reason why high An zones are not seen could be that introduction of the hotter magma caused dissolution rather than crystallization, evidence for which is seen in the Kashele crystals.

A more likely environment where crystals would come in contact with multiple batches of melt is a magma conduit through which melt is transferred between magma chambers. A schematic of magma movement through such a conduit is shown in Figure 6.5. For magma moving through a dike under conditions of laminar flow, the flow velocity would be greatest at the center and lowest at the dike walls, where a solidification front could perhaps be maintained. Because the flow is laminar, mixing between melt from the center and melt from the edges of the dike will be minimized. Within the suspension zone, there would likely be some turbulence, ensuring that input melts are mixed with the melts in the suspension zone. Since flow rates are low near the suspension zone, the mixing process would be relatively slow, and growth rate of crystals could be faster than the rate of melt homogenization. A growing crystal will record this slower mixing process as gradual changes between compositional zones, as opposed to sharp zone boundary changes. Since crystals can grow at variable rates along the different crystallographic directions, the width over which the variations are recorded would depend on the aspect ratio of the crystal. As discussed in Chapters VI and V, this is true for the Kashele giant plagioclase.

Eruption of the GPB crystals could have taken place when magma of $^{87}Sr/^{86}Sr$ composition 0.7096 passed through the conduit and swept the crystals into a temporary holding chamber. This step is necessary, since the composition 0.7096 is not observed as an eruptive unit. The outermost zone of the Kashele crystals is a thin rim with $^{87}Sr/^{86}Sr$ of 0.71040 – 0.71050. We can assume all magmas that passed through the conduit to have collected in the staging area (i.e. shallow magma chamber) before eruption. Magma of $^{87}Sr/^{86}Sr$ 0.7096 would pick up the plagioclase crystals from the conduit and introduce them into the shallow chamber, which would probably contain magma of $^{87}Sr/^{86}Sr$ composition 0.71174, similar to the Igatpuri flow erupted immediately before the Kashele GPB. Mixing between the two compositions in the chamber would be rapid, and a 50:50 mix would result in homogenized magma of $^{87}Sr/^{86}Sr$ 0.7106, which then erupted as the Kashele GPB. During this process, GPB crystals may have suffered dissolution, followed by the growth of the outermost rim with $^{87}Sr/^{86}Sr$ of 0.71040 – 0.71050. Kashele groundmass has highly variable $^{87}Sr/^{86}Sr$ ratios of 0.71061±0.00027, which may be because incomplete homogenization of the magma prior to eruption.

It must be noted that the final stage in the growth of the GPB, viz. transfer from the conduit to the low level staging area has some similarity to the HC model. the difference being that the bulk of crystal growth occurred separately. The growth of the crystals in the dike is similar to the Sen et al. (2006) "chicken wire" model. However, it is probably not possible to erupt the interconnected mass of crystals in the chicken wire network. A phenocryst bearing magma would likely lose its crystal population when passing through such a network, and if the mass of crystals was erupted, it would have crystals of mixed origin. This is not the case with the GPB as all crystals show similar

compositions and zoning features. The laminar flow model of Figure 6.5 seems to be the best explanation for the Kashele GPB.

Future research directions

We have seen that diffusion modeling of zoning in the "giant" plagioclase crystals is a useful tool to better constrain the eruptive duration of the Deccan and I plan to use the same techniques on plagioclase phenocrysts from other Deccan Formations. The first step would be to complete similar studies on the other GPB flows from the Kalsubai Subgroup. Apart from the application to timescale calculations, we have seen that plagioclase zoning is a useful tool in the study of magma chamber processes. Two stratigraphically successive formations (Jawhar and Igatpuri) have plagioclase crystals with widely varying zoning systematics and growth histories. The study of the other formations will provide a near-continuous of magmatic processes leading to the eruption of the Kalsubai Subgroup. GPB flows appear to be absent from the younger subgroups, however zoning studies could still be carried out on other plagioclase phyric flows. The well studied, chemically uniform and volumetrically significant Ambenali Formation would be an ideal subject of study, and another advantage is that the spatial extent of this formation is probably the best known of the Western Ghats formations. This could enable the calculation of a more robust 3-D extrusion rate.

Summary of Conclusions

1. The lowermost Jawhar Formation of the Deccan Western Ghats consists of evolved lava flows that have elevated Sr isotopic ratios of 0.7090 – 0.7128.

124

2. Flows from the Igatpuri Formation are higher in Mg# than most Jawhar flows, and have correspondingly higher $^{87}Sr/^{86}Sr$ ratios.

3. The high Mg# flows of the Jawhar and Igatpuri Formations define a trend in Mg# vs $^{87}Sr/^{86}Sr$ opposite to that expected from AFC processes.

4. Zoning systematics in giant plagioclase phenocrysts from the Thalghat and Kashele GPB are dissimilar, possibly owing to differing growth histories and / or growth environments.

5. Thalghat giant plagioclase crystals are mostly unzoned, with respect to $^{87}Sr/^{86}Sr$, major and trace elements. The few crystals that show zoning have a single rim layer over a core zone. Zonal variations are seen only in $^{87}Sr/^{86}Sr$, major and trace element concentrations are roughly equal in the core and rim. Growth was probably in a steady state magma chamber under equilibrium growth conditions.

6. All Keshele plagioclase crystals studied were zoned with multiple growth zones and widely varying compositional variations in $^{87}Sr/^{86}Sr$ between zones. Keshele plagioclase probably grew in a constantly varying magma composition in disequilibrium conditions, and this growth likely took place in a magma conduit rather than a magma chamber.

7. Zoning profiles in Thalghat GPB have been affected by intracrystalline diffusive processes, and diffusion modeling can constrain the residence timescales of these crystals.

8. Thalghat plagioclase phenocrysts have a calculated growth rate of 2.03×10^{-10} cm/s.

9. Residence time of a 5 cm long Thalghat crystal will be 781 years.

10. 1-D eruptive rate of Thalghat GPB flow is 0.1 m/y. Deccan eruptive duration could be on the order of 35,000 years. A more rigorous estimate would require similar studies to be carried out on the remaining Deccan formations.
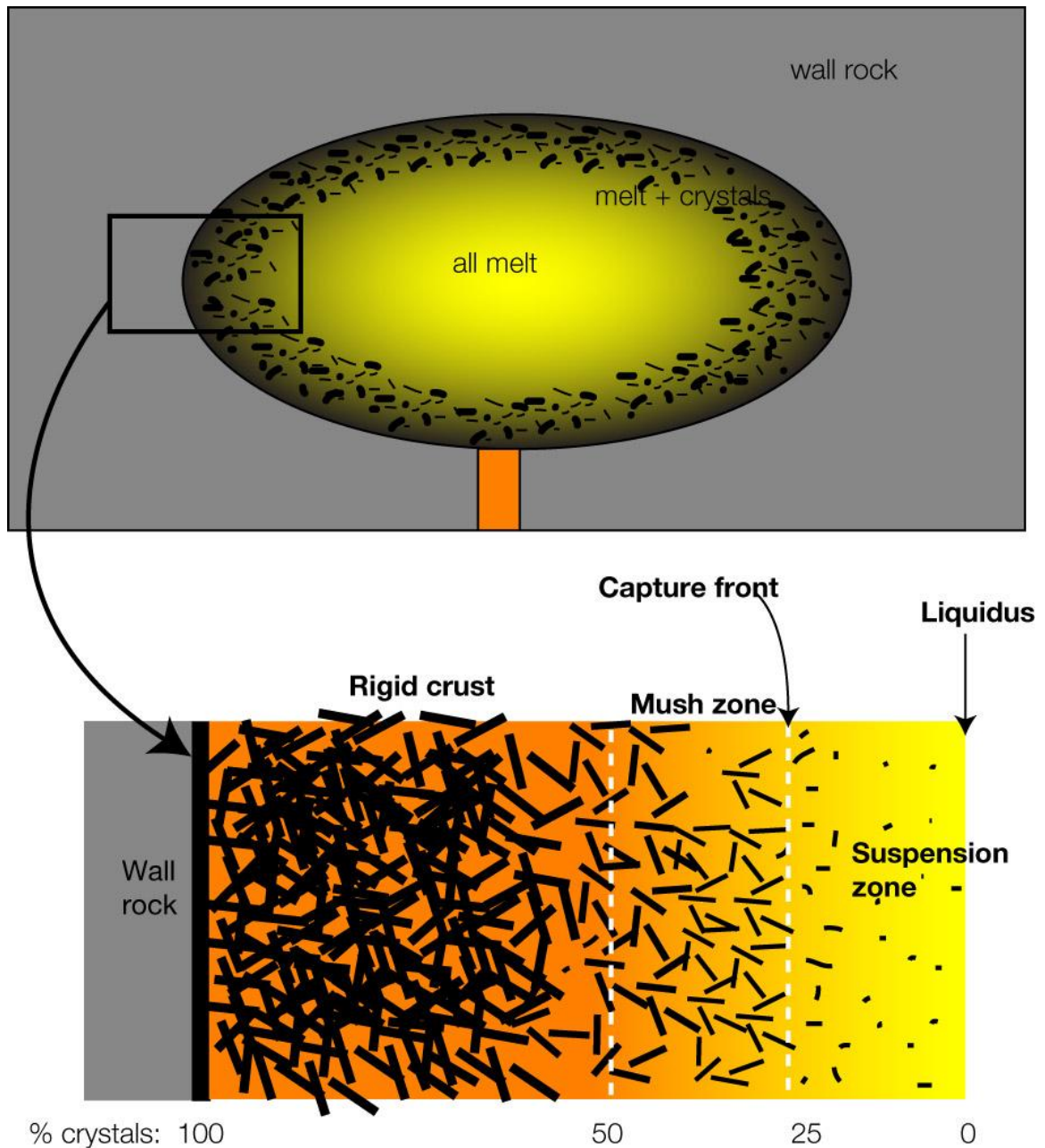
Figure 6.1. Schematic of a solidification front magma chamber. The magma chamber is stratified, with a crystal free center and a boundary with varying amount of cryatallinity. The magma is emplaced into the chamber as a near-liquidus melt, and begins to lose heat to the wall rock forming a chilled margin. With further cooling, temperature will decrease inward, and crystallization will commence. The crystallization front that is so formed will continue to move inwards, bounded by the liquidus at one end, and the wall rock on the other. Based on degree of crystallization, the solidification front can be divided into the suspension zone, mush zone and the rigid crust, demarcated by white dotted lines in the bottom sketch. Melts in the rigid crust are isolated from the

rest of the chamber, and will continue to differentiate to silicic compositions. Only liquids from the suspension zone are eruptible.

GPB
3
2
1

LAVA FLOWS

Conduit
[feeder dike]

"Giant"
Plagioclase

MAGMA CHAMBER

Solidification fronts

Largely molten

From Source

A

Melt SiO$_2$ (wt. %)

70

60

50

% Crystals

95
85
75
50
5

B
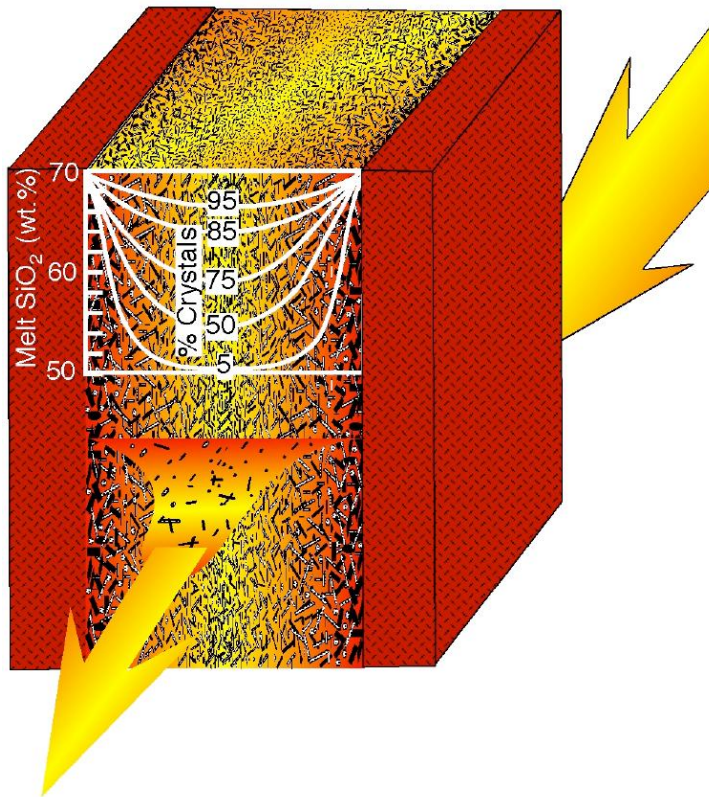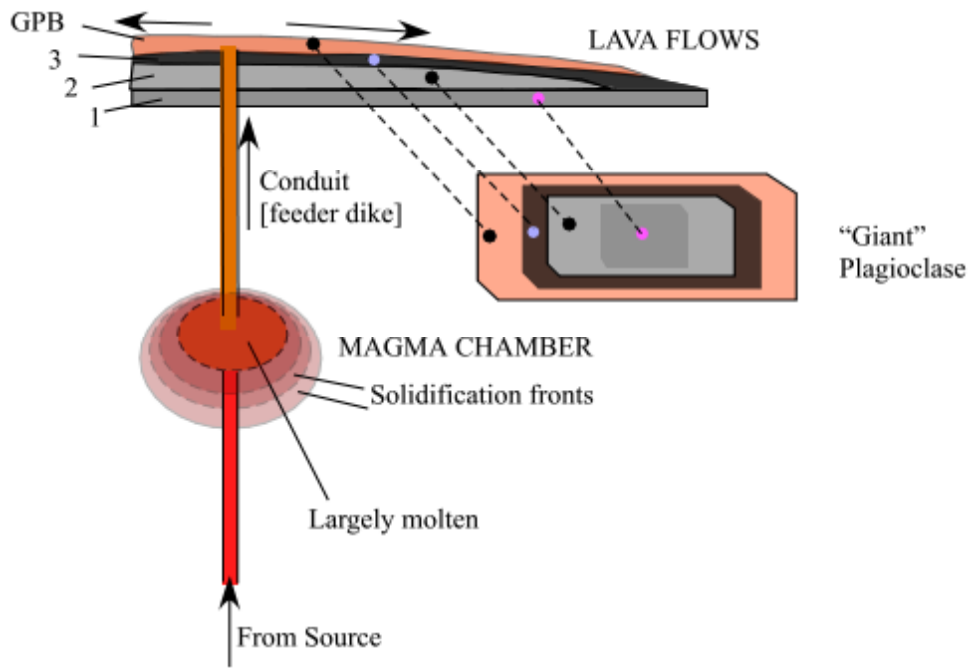
Figure 6.2. Schematic of the Sen (2001) model of GPB formation. Flows from one entire formation originate from a single magma chamber . Giant plagioclase crystals will grow along the periphery of the chamber throughout the life cycle of the formation, and

129

will be zoned with each zone being related to a different flow in the formation. Dashed lines in the upper figure connect the crystal zones with the flows they grew in equilibrium with. As the magma composition evolves, its density increases to a point where the growing crystals can float in the liquid. They will then collect at the top of the chamber and will be extruded when the chamber collapses, thus ending the cycle of magmatism.

Sen et al. (2006) provided a second mode of GPB formation where crystals grow in a magma conduit (bottom figure). The crystals grown in this conduit will form a loosely connected mesh that they label a "chicken wire network". This network acts as a sieve, allowing the crystals to be flushed through with fresh magma, enabling them to grow to large sizes.

(a) Eruption of 'normal' flood basalts

Magma conduit

Faults

(b) Surface weathering and sub-volcanic plutonism

Red bole

Magma chamber

Coarsening

Plagioclase flotation cumulates

Magma conduit

Hot, rising magma

(c) Draining of magma chamber and eruption of Giant Phenocryst Basalts

Magma chamber

Plagioclase flotation cumulates

Mafic cumulates
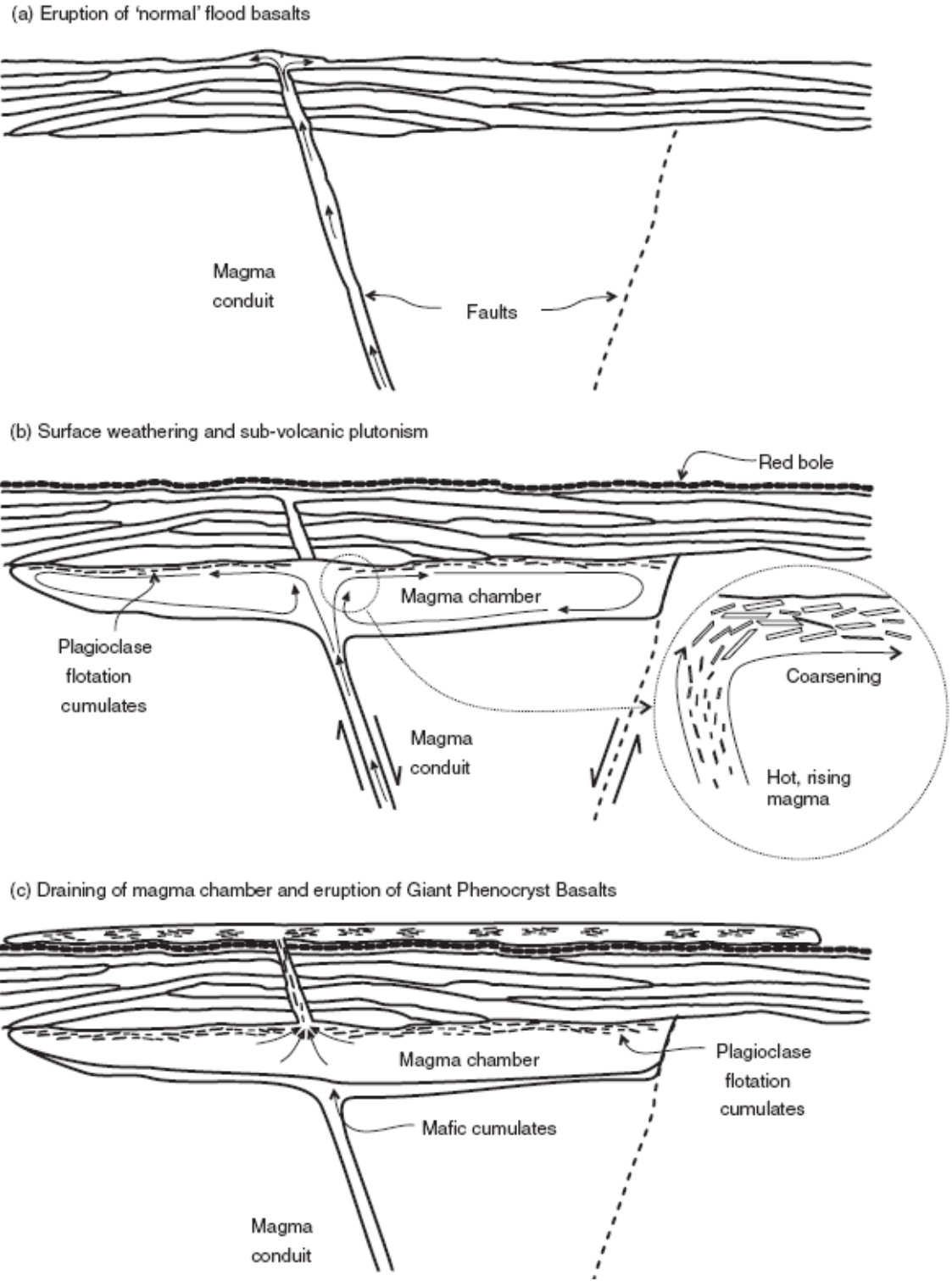
Magma conduit

Figure 6.3. Schematic of the Higgins and Chandrasekharam (2007) model of GPB formation. (a) Normal basalts erupt through conduits to the surface. (b) When the conduit is closed off, magma will pond in a shallow magma chamber. This is when giant crystals will begin to grow. The crystals will be carried to the top of the chamber by

convection, where they will accumulate and coarsen. (c) When the pathway to the surface is reopened, the crystal laden magma will erupt as a GPB flow.
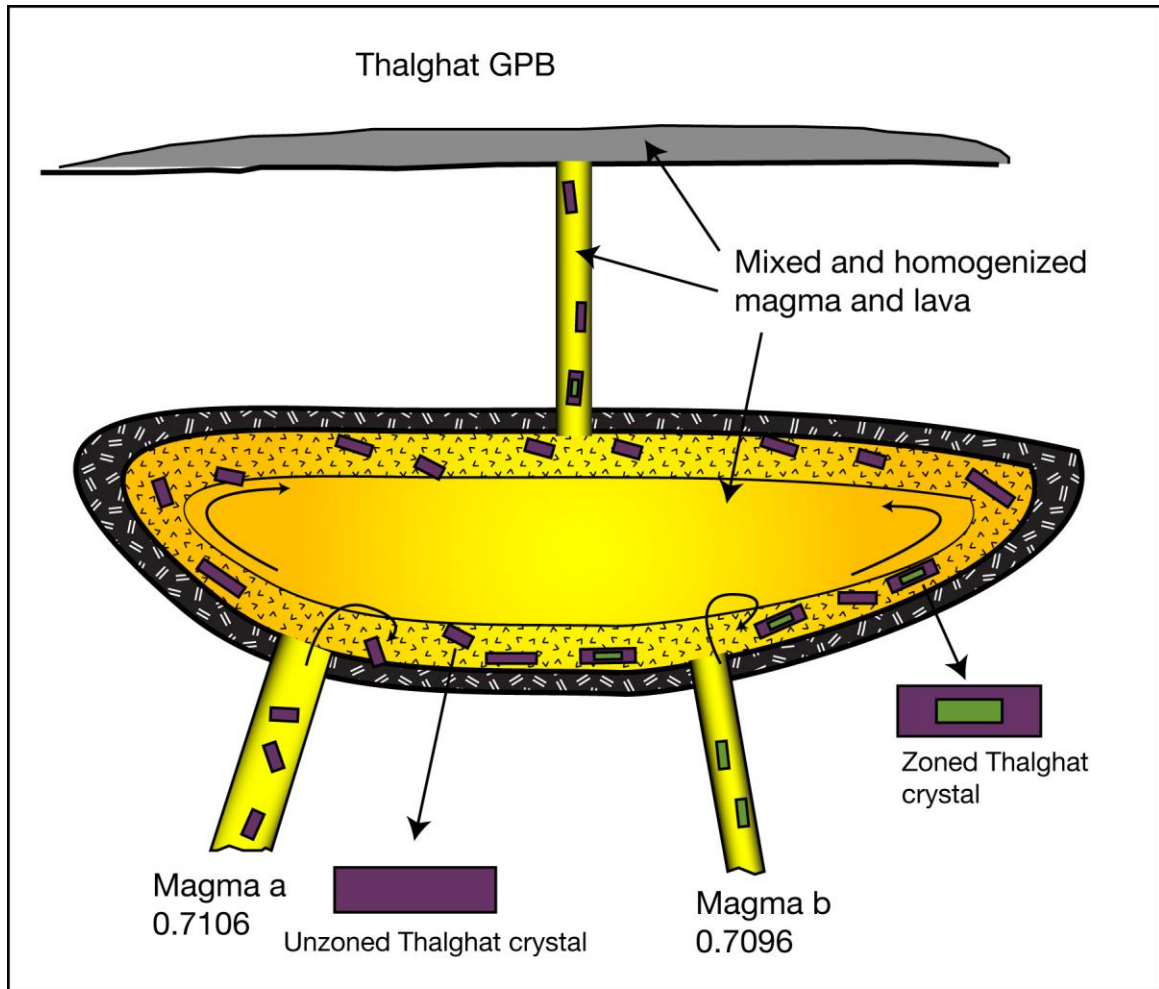
Figure 6.4. Origin of zoning in Thalghat GPB. Plagioclase crystals are growing in a magma chamber of Sr-isotope composition 0.7106, labeled Magma a in the figure. A small amount of crystal bearing magma, Magma b, both with composition 0.7096 is intruded into the chamber. The composition of magma in the chamber is not affected by this minor input. New layers with $^{87}Sr/^{86}Sr$ 0.7106 will grow on the crystals intruded into this chamber. Growth processes are similar to those of the previous schemes. The GPB magma that erupts will have zoned and unzoned crystals, and the zoned crystals be a minor proportion of the total crystal population.
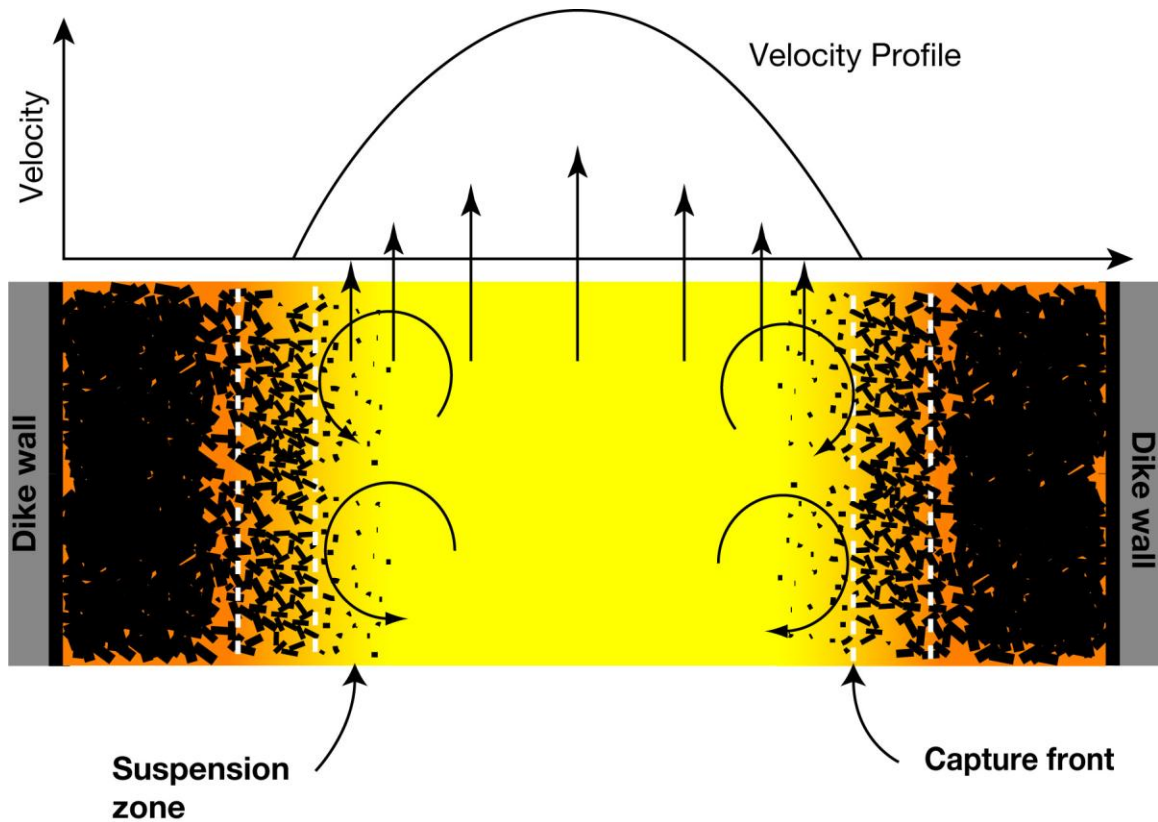
Figure 6.5. Schematic of Kashele crystal growth in a magma conduit. This can be considered a refinement of the Sen et al. (2006) model shown in Figure 6.2. The magma conduit does not have a "chicken wire" mesh, but is bounded by solidification fronts. Laminar flow through the dike will have a velocity profile as shown by the top curve. Straight arrows of various lengths show the direction and magnitude of velocity across the central portion of the dike. Turbulent eddies are denoted by circular arrows, limited to the suspension zone. Kashele crystals will grow in this zone.

LIST OF REFERENCES

Allegre, C.J., Birck, J.L., Capmas, F., and Courtillot, V., 1999, Age of the Deccan Traps using ^{187}Re-^{187}Os systematics: Earth and Planetary Science Letters, v. 170, p. 197-204.

Alvarez, L.W., Alvarez, W., Asaro, F., and Michel, H.V., 1980, Extraterrestrial cause for the Cretaceous Tertiary extinction: Science, v. 208, p. 1095-1108.

Ariskin, A.A., 1999, Phase equilibria modeling in igneous petrology; use of COMAGMAT model for simulating fractionation of ferro-basaltic magmas and the genesis of high-alumina basalt: Journal of Volcanology and Geothermal Research, v. 90, p. 115-162.

Basu, A.R., Renne, P.R., Dasgupta, D.K., Teichmann, F., and Poreda, R.J., 1993, Early and late alkali igneous pulses and a high- ^{3}He plume origin for the Deccan flood basalts: Science, v. 261, p. 902-906.

Beane, J.E., 1988, Flow stratigraphy, chemical variation and petrogenesis of Deccan flood basalts from the Western Ghats, India [Ph.D. thesis], Washington State University, Pullman, WA, United States (USA).

Beane, J.E., Hooper, P.R., and Subbarao, K.V., 1988, A note on the picrite basalts of the Western Ghats, Deccan Traps, India: Memoir - Geological Society of India, v. 10, p. 117-133.

Beane, J.E., Turner, C.A., Hooper, P.R., Subbarao, K.V., and Walsh, J.N., 1986, Stratigraphy, composition and form of the Deccan Basalts, Western Ghats, India: Bulletin of Volcanology, v. 48, p. 61-83.

Behrens, H., Johannes, W., and Schmalzried, H., 1990, On the mechanisms of cation diffusion processes in ternary feldspars: Physics and Chemistry of Minerals, v. 17, p. 62-78.

Blundy, J.D., and Wood, B.J., 1991, Crystal-chemical controls on the partitioning of Sr and Ba between plagioclase feldspar, silicate melts, and hydrothermal solutions: Geochimica et Cosmochimica Acta, v. 55, p. 193-209.

Bodas, M.S., Khadri, S.F.R., Subbarao, K.V., and Subbarao, K.V., 1988, Stratigraphy of the Jawhar and Igatpuri formations, western Ghat lava pile, India: Memoir - Geological Society of India, v. 10, p. 235-252.

Brady, J.B., 1995, Diffusion data for silicate minerals, glasses, and liquids: AGU Reference Shelf, v. 2, p. 269-290.

Brandon, A.D., Walker, R.J., Morgan, J.W., Norman, M.D., and Prichard, H.M., 1998, Coupled [186]Os and [187]Os Evidence for Core-Mantle Interaction: Science, v. 280, p. 1570-1573.

Burkhard, D.J.M., 2005, Nucleation and growth rates of pyroxene, plagioclase, and Fe-Ti oxides in basalt under atmospheric conditions: European Journal of Mineralogy, v. 17, p. 675-685.

Campbell, I.H., and Griffiths, R.W., 1990, Implications of mantle plume structure for the evolution of flood basalts: Earth and Planetary Science Letters, v. 99, p. 79-93.

Cashman, K.V., and Marsh, B.D., 1988, Crystal size distribution (CSD) in rocks and the kinetics and dynamics of crystallization; 2, Makaopuhi lava lake: Contributions to Mineralogy and Petrology, v. 99, p. 292-305.

Chenet, A.-L., Quidelleur, X., Fluteau, F., Courtillot, V., and Bajpai, S., 2007, [40]K-[40]Ar dating of the Main Deccan large igneous province: Further evidence of KTB age and short duration: Earth and Planetary Science Letters, v. 263, p. 1-15.

Cherniak, D.J., 2003, Silicon self-diffusion in single-crystal natural quartz and feldspar: Earth and Planetary Science Letters, v. 214, p. 655-668.

Cherniak, D.J., and Watson, E.B., 1994, A study of strontium diffusion in plagioclase using Rutherford backscattering spectroscopy: Geochimica et Cosmochimica Acta, v. 58, p. 5179-5190.

Cohen, T.H., and Sen, G., 1994, Fractionation and ascent of Deccan Trap magmas; an experimental study at 6 kilobar pressure, *in* Subbarao, K.V., ed., Volcanism, Wiley Eastern Limited, p. 173-186.

Collier, J.S., Minshull, T.A., Kendall, J.M., Whitmarsh, R.B., Ruempker, G., Joseph, P., Samson, P., Lane, C.I., Sansom, V., Vermeesch, P.M., Hammond, J., Wookey, J., Teanby, N., Ryberg, T.M., and Dean, S.M., 2004, Rapid continental breakup and microcontinent formation in the western Indian Ocean: Eos, Transactions, American Geophysical Union, v. 85, p. 481.

Costa, F., Chakraborty, S., and Dohmen, R., 2003, Diffusion coupling between trace and major elements and a model for calculation of magma residence times using plagioclase: Geochimica et Cosmochimica Acta, v. 67, p. 2189-2200.

Courtillot, V., Besse, J., Vandamme, D., Montigny, R., Jaeger, J.-J., and Cappetta, H., 1986, Deccan flood basalts at the Cretaceous/Tertiary boundary?: Earth and Planetary Science Letters, v. 80, p. 361-374.

Courtillot, V., Feraud, G., Maluski, H., Vandamme, D., Moreau, M.G., and Besse, J., 1988, Deccan flood basalts and the Cretaceous/Tertiary boundary: Nature, v. 333, p. 843-846.

Courtillot, V., Jaupart, C., Manighetti, I., Tapponnier, P., and Besse, J., 1999, On causal links between flood basalts and continental breakup: Earth and Planetary Science Letters, v. 166, p. 177-195.

Courtillot, V.E., and Renne, P.R., 2003, On the ages of flood basalt events: Comptes Rendus Geosciences, v. 335, p. 113-140.

Cox, K.G., and Hawkesworth, C.J., 1985, Geochemical stratigraphy of the Deccan Traps at Mahabaleshwar, western Ghats, India, with implications for open system magmatic processes: Journal of Petrology, v. 26, p. 355-377.

Davidson, J., Tepley, F., III, Palacz, Z., and Meffan-Main, S., 2001, Magma recharge, contamination and residence times revealed by in situ laser ablation isotopic analysis of feldspar in volcanic rocks: Earth and Planetary Science Letters, v. 184, p. 427-442.

DePaolo, D.J., 1981, Trace element and isotopic effects of combined wallrock assimilation and fractional crystallization: Earth and Planetary Science Letters, v. 53, p. 189-202.

Devey, C.W., and Cox, K.G., 1987, Relationships between crustal contamination and crystallisation in continental flood basalt magmas with special reference to the Deccan Traps of the Western Ghats, India: Earth and Planetary Science Letters, v. 84, p. 59-68.

Devey, C.W., and Stephens, W.E., 1991, Tholeiitic dykes in the Seychelles and the original spatial extent of the Deccan: Journal of the Geological Society of London, v. 148, p. 979-983.

Duncan, R.A., and Pyle, D.G., 1988, Rapid eruption of the Deccan flood basalts at the Cretaceous/Tertiary boundary: Nature, v. 333, p. 841-843.

Eldholm, O., and Coffin, M.F., 2000, Large igneous provinces and plate tectonics: Geophysical Monograph, v. 121, p. 309-326.

Gallet, Y., Weeks, R., Vandamme, D., and Courtillot, V., 1989, Duration of Deccan Trap volcanism; a statistical approach: Earth and Planetary Science Letters, v. 93, p. 273-282.

Ghiorso, M.S., Hirschmann, M.M., Reiners, P.W., and Kress, V.C., III, 2002, The pMELTS: A revision of MELTS aimed at improving calculation of phase relations and major element partitioning involved in partial melting of the mantle at pressures up to 3 GPa: Geochemistry, Geophysics, Geosystems, v. 3, p. 28.

Ghiorso, M.S., and Sack, R.O., 1995, Chemical mass transfer in magmatic processes; IV, A revised and internally consistent thermodynamic model for the interpolation and extrapolation of liquid-solid equilibria in magmatic systems at elevated

temperatures and pressures: Contributions to Mineralogy and Petrology, v. 119, p. 197-212.

Giletti, B.J., and Casserly, J.E.D., 1994, Strontium diffusion kinetics in plagioclase feldspars: Geochimica et Cosmochimica Acta, v. 58, p. 3785-3793.

Goetze, J., Habermann, D., Kempe, U., Neuser, R.D., and Richter, D.K., 1999, Cathodoluminescence microscopy and spectroscopy of plagioclases from lunar soil: American Mineralogist, v. 84, p. 1027-1032.

Gwalani, L.G., Rock, N.M.S., Chang, W.J., Fernandez, S., Allegre, C.J., and Prinzhofer, A., 1993, Alkaline rocks and carbonatites of Amba Dongar and adjacent areas, Deccan igneous province, Gujarat, India; 1, Geology, petrography and petrochemistry: Mineralogy and Petrology, v. 47, p. 219-253.

Hart, S.R., Hauri, E.H., Oschmann, L.A., and Whitehead, J.A., 1992, Mantle Plumes and Entrainment: Isotopic Evidence: Science, v. 256, p. 517-520.

Hess, H.H., 1960, Stillwater igneous complex, Montana--a quantitative mineralogical study: Memoir - Geological Society of America, p. 230.

Higgins, M.D., 2005, A new interpretation of the structure of the Sept Iles intrusive suite, Canada: Lithos, v. 83, p. 199-213.

Higgins, M.D., and Chandrasekharam, D., 2007, Nature of Sub-volcanic Magma Chambers, Deccan Province, India: Evidence from Quantitative Textural Analysis of Plagioclase Megacrysts in the Giant Plagioclase Basalts: J. Petrology, v. 48, p. 885-900.

Hofmann, C., Feraud, G., and Courtillot, V., 2000, $^{40}Ar/^{39}Ar$ dating of mineral separates and whole rocks from the Western Ghats lava pile; further constraints on duration and age of the Deccan Traps: Earth and Planetary Science Letters, v. 180, p. 13-27.

Hooper, P.R., 1999, The winds of change, the Deccan Traps; a personal perspective: Memoir - Geological Society of India, v. 43, Part 1, p. 153-165.

Hooper, P.R., Subbarao, K.V., Beane, J.E., and Subbarao, K.V., 1988, The giant plagioclase basalts (GPBs) of the Western Ghats, Deccan Traps: Memoir - Geological Society of India, v. 10, p. 135-144.

Huppert, H.E., and Turner, J.S., 1991, Comments on On convective style and vigor in sheet-like magma chambers by Bruce D. Marsh: Journal of Petrology, v. 32, p. 851-860.

Irvine, T.N., 1987, Layering and related structures in the Duke Island and Skaergaard intrusions; similarities, differences, and origins: NATO ASI Series Series C: Mathematical and Physical Sciences, v. 196, p. 185-245.

Izbekov, P.E., Eichelberger, J.C., Patino, L.C., Vogel, T.A., and Ivanov, B.V., 2002, Calcic cores of plagioclase phenocrysts in andesite from Karymsky Volcano; evidence for rapid introduction by basaltic replenishment: Geology (Boulder), v. 30, p. 799-802.

Jerram, D.A., and Widdowson, M., 2005, The anatomy of continental flood basalt provinces; geological constraints on the processes and products of flood volcanism, *in* Kerr, A.C., England, R.W., and Wignall, P.B., eds., Lithos, Volume 79, p. 385-405.

Karmarkar, B.M., Kulkarni, S.R., Marathe, S.S., Sowani, P.V., and Peshwa, V.V., 1972, Giant Phenocryst Basalts in the Deccan Trap: Bulletin of Volcanology, v. 35, p. 965-974.

King, S.D., and Anderson, D.L., 1995, An alternative mechanism of flood basalt formation: Earth and Planetary Science Letters, v. 136, p. 269-279.

Kohut, E., and Nielsen, R.L., 2004, Melt inclusion formation mechanisms and compositional effects in high-An feldspar and high-Fo olivine in anhydrous mafic silicate liquids: Contributions to Mineralogy and Petrology, v. 147, p. 684-704.

Krishnamurthy, P., and Cox, K.G., 1977, Picrite basalts and related lavas from the Deccan Traps of western India: Contributions to Mineralogy and Petrology, v. 62, p. 53-75.

Krishnamurthy, P., Gopalan, K., and Macdougall, J.D., 2000, Olivine compositions in picrite basalts and the Deccan volcanic cycles: Journal of Petrology, v. 41, p. 1057-1069.

Larsen, J.F., 2005, Experimental study of plagioclase rim growth around anorthite seed crystals in rhyodacitic melt: American Mineralogist, v. 90, p. 417-427.

LaTourrette, T., Wasserburg, G.J., and Fahey, A.J., 1996, Self diffusion of Mg, Ca, Ba, Nd, Yb, Ti, Zr, and U in haplobasaltic melt: Geochimica et Cosmochimica Acta, v. 60, p. 1329-1340.

Lee, M.R., Parsons, I., Edwards, P.R., Martin, R.W., Coulson, I.M., Edwards, P.R., and Lee, M.R., 2007, Identification of cathodoluminescence activators in zoned alkali feldspars by hyperspectral imaging and electron-probe microanalysis: American Mineralogist, v. 92, p. 243-253.

Lightfoot, P.C., and Hawkesworth, C.J., 1988, Origin of Deccan Trap lavas; evidence from combined trace element and Sr-, Nd- and Pb-isotope studies: Earth and Planetary Science Letters, v. 91, p. 89-104.

Lightfoot, P.C., Hawkesworth, C.J., Devey, C.W., Rogers, N.W., and van Calsteren, P.W.C., 1990, Source and differentiation of Deccan Trap lavas; implications of geochemical and mineral chemical variations: Journal of Petrology, v. 31, p. 1165-1200.

Mahoney, J., Macdougall, J.D., Lugmair, G.W., Murali, A.V., Sankar Das, M., and Gopalan, K., 1982, Origin of the Deccan Trap flows at Mahabaleshwar inferred from Nd and Sr isotopic and chemical evidence: Earth and Planetary Science Letters, v. 60, p. 47-60.

Mahoney, J.J., 1988, Deccan Basalts, *in* Macdougall, J.D., ed., Continental Flood Basalts, Kluwer Academic Publishers.

Mahoney, J.J., Sheth, H.C., Chandrasekharam, D., Peng, Z.X., and Anonymous, 2000, Geochemistry of flood basalts of the Toranmal section, northern Deccan Traps, India; implications for regional Deccan stratigraphy: Journal of Petrology, v. 41, p. 1099-1120.

Marsh, B.D., 1988, Crystal capture, sorting, and retention in convecting magma: Geological Society of America Bulletin, v. 100, p. 1720-1737.

Marsh, B.D., 1989a, Magma chambers: Annual Review of Earth and Planetary Sciences, v. 17, p. 439-474.

Marsh, B.D., 1989b, On convective style and vigor in sheet-like magma chambers: Journal of Petrology, v. 30, p. 479-530.

Marsh, B.D., 1996, Solidification fronts and magmatic evolution: Mineralogical Magazine, v. 60, p. 5-40.

McDonough, W.F., and Sun, S.S., 1995, The composition of the Earth: Chemical Geology, v. 120, p. 223-253.

Melluso, L., Barbieri, M., and Beccaluva, L., 2004, Chemical evolution, petrogenesis, and regional chemical correlations of the flood basalt sequence in the central Deccan Traps, India: Proceedings of the Indian Academy of Sciences: Earth and Planetary Sciences, v. 113, p. 587-603.

Melluso, L., Mahoney, J.J., and Dallai, L., 2006, Mantle sources and crustal input as recorded in high-Mg Deccan Traps basalts of Gujarat (India): Lithos, v. 89, p. 259-274.

Mora, C.I., and Ramseyer, K., 1992, Cathodoluminescence of coexisting plagioclases, Boehls Butte anorthosite; CL activators and fluid flow paths: American Mineralogist, v. 77, p. 1258-1265.

Najafi, S.J., Cox, K.G., Sukheswala, R.N., Subbarao, K.V., and Sukheswala, R.N., 1981, Geology and geochemistry of the basalt flows (Deccan Traps) of the Mahad-Mahableshwar section, India: Memoir - Geological Society of India, v. 3, p. 300-315.

Pande, K., 2002, Age and duration of the Deccan Traps, India; a review of radiometric and paleomagnetic constraints: Proceedings of the Indian Academy of Sciences: Earth and Planetary Sciences, v. 111, p. 115-123.

Panjasawatwong, Y., Danyushevsky, L.V., Crawford, A.J., and Harris, K.L., 1995, An experimental study of the effects of melt composition on plagioclase; melt equilibria at 5 and 10 kbar; implications for the origin of magmatic high-An plagioclase: Contributions to Mineralogy and Petrology, v. 118, p. 420-432.

Peng, Z.X., Mahoney, J., Hooper, P., Harris, C., and Beane, J., 1994, A role for lower continental crust in flood basalt genesis? Isotopic and incompatible element study of the lower six formations of the western Deccan Traps: Geochimica et Cosmochimica Acta, v. 58, p. 267-288.

Peng, Z.X., Mahoney, J.J., Hooper, P.R., Macdougall, J.D., and Krishnamurthy, P., 1998, Basalts of the northeastern Deccan Traps, India; isotopic and elemental geochemistry and relation to southwestern Deccan stratigraphy: Journal of Geophysical Research, B, Solid Earth and Planets, v. 103, p. 29,843-29,865.

Ramos, F.C., Wolff, J.A., and Tollstrup, D.L., 2005, Sr isotope disequilibrium in Columbia River flood basalts; evidence for rapid shallow-level open-system processes: Geology (Boulder), v. 33, p. 457-460.

Rampino, M.R., and Stothers, R.B., 1988, Flood Basalt Volcanism During the Past 250 Million Years: Science, v. 241, p. 663-668.

Ravizza, G., and Peucker-Ehrenbrink, B., 2003, Chemostratigraphic evidence of Deccan volcanism from the marine osmium isotope record: Science, v. 302, p. 1392-1395.

Richards, M.A., Duncan, R.A., and Courtillot, V.E., 1989, Flood basalts and hot-spot tracks; plume heads and tails: Science, v. 246, p. 103-107.

Sano, T., Fujii, T., Deshmukh, S.S., Fukuoka, T., and Aramaki, S., 2001, Differentiation processes of Deccan Trap basalts; contribution from geochemistry and experimental petrology: Journal of Petrology, v. 42, p. 2175-2195.

Self, S., Blake, S., Sharma, K., Widdowson, M., and Sephton, S., 2008, Sulfur and Chlorine in Late Cretaceous Deccan Magmas and Eruptive Gas Release: Science, v. 319, p. 1654-1657.

Self, S., Widdowson, M., Thordarson, T., and Jay, A.E., 2006, Volatile fluxes during flood basalt eruptions and potential effects on the global environment: A Deccan perspective: Earth and Planetary Science Letters, v. 248, p. 518-532.

Sen, G., 1986, Mineralogy and petrogenesis of the Deccan Trap lava flows around Mahabaleshwar, India: Journal of Petrology, v. 27, p. 627-663.

Sen, G., 1995, A simple petrologic model for the generation of Deccan Trap magmas: International Geology Review, v. 37, p. 825-850.

Sen, G., 2001, Generation of Deccan Trap magmas: Proceedings of the Indian Academy of Sciences: Earth and Planetary Sciences, v. 110, p. 409-431.

Sen, G., Borges, M., and Marsh, B.D., 2006, A case for short duration of Deccan Trap eruption: Eos, Transactions, American Geophysical Union, v. 87, p. 197.

Sheth, H.C., Pande, K., and Bhutani, R., 2001, ^{40}Ar/^{39}Ar ages of Bombay trachytes; evidence for a Palaeocene phase of Deccan volcanism: Geophysical Research Letters, v. 28, p. 3513-3516.

Simonetti, A., Bell, K., and Viladkar, S.G., 1995, Isotopic data from the Amba Dongar carbonatite complex, west-central India; evidence for an enriched mantle source: Chemical Geology, v. 122, p. 185-198.

Simonetti, A., Goldstein, S.L., Schmidberger, S.S., and Viladkar, S.G., 1998, Geochemical and Nd, Pb, and Sr isotope data from Deccan alkaline complexes; inferences for mantle sources and plume; lithosphere interaction: Journal of Petrology, v. 39, p. 1847-1864.

Smith, J.V., 1974, Feldspar Minerals; 1, Crystal Structure and Physical Properties, Springer-Verlag.

Subbarao, K.V., Bodas, M.S., Hooper, P.R., Walsh, J.N., and Subbarao, K.V., 1988, Petrogenesis of Jawhar and Igatpuri formations, western Deccan basalt province: Memoir - Geological Society of India, v. 10, p. 253-280.

Sun, S.S., 1980, Lead isotopic study of young volcanic rocks from mid-ocean ridges, ocean islands and island arcs: Philosophical Transactions of the Royal Society of London, Series A: Mathematical and Physical Sciences, v. 297, p. 409-445.

Sun, S.S., and McDonough, W.F., 1989, Chemical and isotopic systematics of oceanic basalts; implications for mantle composition and processes: Geological Society Special Publications, v. 42, p. 313-345.

Tepley, F.J., III, and Davidson, J.P., 2003, Mineral-scale Sr-isotope constraints on magma evolution and chamber dynamics in the Rum layered intrusion, Scotland: Contributions to Mineralogy and Petrology, v. 145, p. 628-641.

Tepley, F.J., III, Davidson, J.P., and Clynne, M.A., 1997, Magma interactions at Chaos Crags, Lassen Volcanic National Park, California: LPI Contribution, v. 921, p. 205.

Tepley, F.J., III, Davidson, J.P., Tilling, R.I., and Arth, J.G., 2000, Magma mixing, recharge and eruption histories recorded in plagioclase phenocrysts from El Chichon Volcano, Mexico: Journal of Petrology, v. 41, p. 1397-1411.

Thordarson, T., and Self, S., 1993, The Laki (Skaftar Fires) and Grimsvotn eruptions in 1783-1785: Bulletin of Volcanology, v. 55, p. 233-263.

Vandamme, D., Courtillot, V., Besse, J., and Montigny, R., 1991, Paleomagnetism and age determinations of the Deccan Traps (India); results of a Nagpur-Bombay traverse and review of earlier work: Reviews of Geophysics, v. 29, p. 159-190.

Viladkar, S.G., 1981, The carbonatites of Amba Dongar, Gujarat, India: Bulletin of the Geological Society of Finland, v. 53, p. 17-28.

Walker, R.J., Morgan, J.W., and Horan, M.F., 1995, Osmium-187 Enrichment in Some Plumes: Evidence for Core-Mantle Interaction?: Science, v. 269, p. 819-822.

Widdowson, M., Pringle, M.S., and Fernandez, O.A., 2000, A post K-T boundary (early Palaeocene) age for Deccan-type feeder dykes, Goa, India: Journal of Petrology, v. 41, p. 1177-1194.

Zellmer, G.F., Blake, S., Vance, D., Hawkesworth, C., and Turner, S., 1999, Plagioclase residence times at two island arc volcanoes (Kameni Islands, Santorini, and Soufriere, St. Vincent) determined by Sr diffusion systematics: Contributions to Mineralogy and Petrology, v. 136, p. 345-357.

APPENDIX

Table 1a XRF major element analyses of samples from the Jawhar Formation. Analyses in wt%.

Oxides (wt%)	SS2	SS3	SS5	SS21	SS22	SS7	SS23	SS25
SiO2	50.39	50.42	49.81	50.58	49.89	52.90	51.35	50.84
TiO2	3.031	3.030	2.913	1.676	2.985	2.131	3.468	3.867
Al2O3	13.46	13.26	13.45	13.91	13.12	18.89	13.68	12.65
FeO*	14.85	15.00	14.55	11.26	15.17	9.01	13.83	14.92
MnO	0.219	0.217	0.219	0.175	0.205	0.136	0.196	0.207
MgO	4.81	4.86	5.45	8.45	5.20	2.94	4.43	4.34
CaO	9.37	9.34	10.13	11.93	9.75	8.94	8.63	8.67
Na2O	2.61	2.63	2.52	1.59	2.46	4.05	2.71	2.65
K2O	0.98	0.97	0.67	0.27	0.94	0.78	1.36	1.46
P2O5	0.283	0.275	0.277	0.160	0.284	0.218	0.351	0.392
Total	100.00	100.00	100.00	100.00	100.00	100.00	100.00	100.00
Mg#	0.366	0.366	0.400	0.572	0.379	0.368	0.363	0.341

Table 1b XRF trace element analyses of samples from the Jawhar Formation. Analyses in ppm.

Element (ppm)	SS2	SS3	SS5	SS21	SS22	SS7	SS23	SS25
Ni	44	41	53	66	45	31	47	42
Cr	55	54	76	388	54	35	60	60
Sc	34	33	33	33	33	16	29	28
V	435	427	424	297	420	220	375	405
Ba	223	220	236	73	237	265	283	291
Rb	24	21	9	11	18	13	38	44
Sr	245	245	264	122	253	317	244	224
Zr	199	194	193	123	197	158	251	276
Y	34	34	33	24	33	24	38	42
Nb	14.5	13.6	14.1	7.2	14.4	11.5	18.1	20.2
Ga	25	24	23	21	23	27	26	26
Cu	182	160	138	44	171	134	195	223
Zn	127	126	123	82	128	80	134	137
Pb	4	4	4	4	5	4	10	7
La	21	22	23	14	21	18	29	32
Ce	53	55	51	32	54	41	69	78
Th	2	2	3	2	2	4	5	7
Nd	32	29	27	20	30	23	39	43

Table 1c Trace and rare earth element ICPMS analyses of samples from the Jawhar Formation. Analyses in ppm.

Elements (ppm)	SS2	SS3	SS5	SS21	SS22	SS7	SS23	SS25
La	22.03	21.53	22.15	15.03	22.55	19.57	29.52	34.07
Ce	49.50	48.33	49.11	31.92	49.77	42.13	64.39	73.77
Pr	6.76	6.58	6.64	4.18	6.71	5.50	8.54	9.70
Nd	29.74	29.10	29.17	18.01	29.34	23.45	36.93	41.31
Sm	7.80	7.73	7.52	4.65	7.48	5.76	9.11	10.25
Eu	2.53	2.50	2.45	1.57	2.41	2.02	2.76	2.89
Gd	8.24	8.06	7.73	5.11	7.76	5.78	9.34	10.29
Tb	1.34	1.33	1.28	0.85	1.26	0.92	1.50	1.65
Dy	7.83	7.73	7.39	5.18	7.46	5.41	8.80	9.70
Ho	1.49	1.48	1.40	1.04	1.41	1.02	1.69	1.82
Er	3.84	3.72	3.55	2.59	3.55	2.61	4.23	4.59
Tm	0.53	0.51	0.48	0.36	0.48	0.36	0.58	0.63
Yb	3.03	2.98	2.80	2.16	2.79	2.06	3.30	3.61
Lu	0.46	0.44	0.42	0.33	0.42	0.31	0.50	0.55
Ba	216	214	233	72	226	258	271	282
Th	3.35	3.27	3.07	2.88	3.09	4.27	5.96	7.57
Nb	14.43	14.20	15.02	8.16	15.25	12.20	19.48	21.93
Y	36.52	35.64	33.97	25.10	33.97	25.15	40.48	44.23
Hf	5.49	5.42	5.36	3.39	5.39	4.38	6.93	7.64
Ta	1.01	0.99	1.02	0.58	1.04	0.86	1.34	1.55
U	0.70	0.70	0.66	0.55	0.64	0.95	1.30	1.63
Pb	3.14	3.13	3.07	2.34	3.25	3.27	6.94	5.57
Rb	23.8	21.3	11.0	10.3	18.7	12.8	38.6	43.9
Cs	0.15	0.23	0.41	0.49	0.27	0.17	0.55	0.65
Sr	256	258	278	129	262	327	255	236
Sc	37.1	37.4	36.8	37.9	36.6	17.6	31.7	31.8
Zr	193	190	188	119	192	153	246	274

Table 2a XRF major element analyses of samples from the Igatpuri Formation. Analyses in wt%.

Oxides (wt%)	SS26	SS27	SS28	SS29	SS211	SS14	SS13
SiO2	51.10	48.76	50.50	50.33	49.21	53.11	49.70
TiO2	2.830	2.723	2.195	1.888	2.009	3.059	2.897
Al2O3	14.16	15.92	14.77	14.19	14.11	13.21	15.94
FeO*	13.34	13.27	12.43	11.88	12.71	14.25	13.57
MnO	0.199	0.170	0.165	0.157	0.187	0.149	0.207
MgO	4.77	5.25	6.41	7.57	8.00	3.89	3.87
CaO	9.80	9.68	9.64	10.63	10.90	8.52	9.91
Na2O	2.72	2.95	2.81	2.38	2.07	2.55	2.88
K2O	0.80	1.00	0.87	0.80	0.64	0.95	0.72
P2O5	0.292	0.279	0.211	0.181	0.181	0.316	0.305
Total	100.00	100.00	100.00	100.00	100.00	100.00	100.00
Mg#	0.389	0.413	0.479	0.532	0.53	0.327	0.337

Oxides (wt%)	SS16	SS11
SiO2	50.60	50.55
TiO2	2.784	3.149
Al2O3	16.37	13.96
FeO*	12.49	14.66
MnO	0.148	0.201
MgO	3.89	3.81
CaO	9.42	9.27
Na2O	2.91	2.71
K2O	1.10	1.36
P2O5	0.290	0.323
Total	100.00	100.00
Mg#	0.357	0.317

Table 2b XRF trace element analyses of samples from the Igatpuri Formation. Analyses in ppm.

Elements (ppm)	SS26	SS27	SS28	SS29	SS211	SS14	SS13
Ni	45	94	65	74	135	33	34
Cr	57	135	63	324	160	35	38
Sc	30	26	28	32	33	30	28
V	382	331	346	341	361	347	350
Ba	275	283	183	195	131	315	272
Rb	14	21	21	19	19	24	16
Sr	275	270	227	232	210	228	343
Zr	206	194	167	134	120	211	205
Y	33	33	28	25	25	35	33
Nb	15.5	12.1	9.1	8.5	6.6	14.7	13.5
Ga	24	26	24	20	21	18	26
Cu	124	183	42	28	110	130	133
Zn	121	117	102	90	99	124	122
Pb	5	5	4	4	1	4	6
La	25	21	15	15	11	24	27
Ce	62	45	38	33	24	54	54
Th	5	2	2	2	4	4	3
Nd	32	28	23	19	16	29	29

Table 2b (contd.)

Elements (ppm)	SS16	SS11
Ni	34	35
Cr	35	39
Sc	28	29
V	340	378
Ba	256	272
Rb	48	45
Sr	316	252
Zr	193	216
Y	32	36
Nb	13.4	15.1
Ga	25	24
Cu	117	131
Zn	116	130
Pb	5	5
La	23	25
Ce	57	57
Th	4	4
Nd	31	33

Table 2c Trace and rare earth element ICPMS analyses of samples from the Jawhar Formation. Analyses in ppm.

Elements (ppm)	SS26	SS27	SS28	SS29	SS211	SS14	SS13
La	26.43	20.64	16.15	15.24	-	26.88	23.21
Ce	56.70	45.08	35.79	32.87	-	56.48	50.60
Pr	7.36	6.11	4.84	4.36	-	7.31	6.73
Nd	31.25	26.72	21.40	18.87	-	31.54	29.01
Sm	7.76	7.03	5.92	5.02	-	7.91	7.34
Eu	2.38	2.34	1.90	1.66	-	2.42	2.37
Gd	7.95	7.49	6.29	5.28	-	8.17	7.75
Tb	1.28	1.22	1.04	0.90	-	1.33	1.25
Dy	7.59	7.34	6.20	5.38	-	7.81	7.37
Ho	1.42	1.41	1.20	1.05	-	1.52	1.44
Er	3.67	3.56	3.09	2.70	-	3.82	3.64
Tm	0.51	0.49	0.42	0.37	-	0.52	0.50
Yb	2.95	2.87	2.44	2.17	-	3.01	2.90
Lu	0.45	0.43	0.37	0.33	-	0.46	0.44
Ba	267	273	173	185	-	309	265
Th	4.95	2.29	2.68	2.38	-	4.78	4.47
Nb	16.41	12.68	9.04	8.85	-	15.47	14.61
Y	35.22	34.28	29.63	25.65	-	36.28	34.80
Hf	5.71	5.24	4.55	3.68	-	5.75	5.53
Ta	1.14	0.85	0.63	0.61	-	1.05	0.99
U	0.99	0.42	0.50	0.47	-	1.00	0.93
Pb	4.50	3.23	2.16	2.07	-	3.30	3.38
Rb	15.1	20.3	20.8	18.6	-	25.5	16.2
Cs	0.66	0.17	0.28	0.16	-	0.78	0.30
Sr	292	281	234	240	-	242	360
Sc	34.9	29.1	32.1	36.6	-	34.2	32.2
Zr	204	188	160	128	-	208	199

Table 2c (contd.)

Elements (ppm)	SS16	SS11
La	22.72	25.49
Ce	49.56	55.68
Pr	6.52	7.37
Nd	27.81	31.86
Sm	7.17	8.12
Eu	2.33	2.50
Gd	7.47	8.39
Tb	1.20	1.37
Dy	7.20	8.32
Ho	1.37	1.55
Er	3.52	4.05
Tm	0.48	0.55
Yb	2.77	3.22
Lu	0.43	0.49
Ba	246	264
Th	4.34	4.88
Nb	13.90	15.86
Y	33.64	38.83
Hf	5.23	5.93
Ta	0.97	1.09
U	0.84	1.04
Pb	3.27	3.37
Rb	48.2	45.0
Cs	0.70	0.72
Sr	332	269
Sc	32.0	35.5
Zr	188	214

VITA

MELROY R. BORGES

October 1, 1975	Born, Mumbai, India
May 1997	BSc. St. Xavier's College, University of Mumbai
1998-1999	Instructor, Gemological Institute of India, Mumbai
May 1999	MSc. St. Xavier's College, University of Mumbai
1999-2001	Teaching Assistant, University of Michigan, Ann Arbor, Research Assistant, University of Michigan, Ann Arbor
August 2001	MS. University of Michigan, Ann Arbor
2004-2005	Teaching Assistant, Florida International University, Miami

AWARDS

2000	Turner Research Award, University of Michigan, Ann Arbor
2002-2005	Presidential Fellowship, FIU, Miami
2007	Dissertation Year Fellowship, FIU, Miami

PUBLICATIONS

Borges, M.; Sen, G.; Hart, G.; Wolff, J. (2008), Application of single crystal Sr isotope diffusion modeling to determine timescales of flood basalt eruptions, EGU General Assembly 2008 (invited), Abstract EGU2008-A-00864.

Borges M R, Sen G, Hart G L, Wolff J A (2007), Sr Isotope Zoning in Plagioclase Phenocrysts from Giant Plagioclase Basalts: Mixing Processes in the Oldest Deccan Formations, Eos Trans. AGU, 88(52), Fall Meet. Suppl., Abstract V11B-0589.

Borges M R, Sen G, Hart G L, Wolff J A (2006), Crystal Zoning in Deccan Giant Plagioclase Basalts: Implications for a Short Duration of Deccan Trap Eruption, Eos Trans. AGU, 87(52), Fall Meet. Suppl., Abstract V51B-1677.

Gautam Sen, Melroy Borges, and Bruce D. Marsh, A case for short duration of Deccan Trap eruption Eos, Transactions, American Geophysical Union (May 2006), 87(20):197, 200

Hall, C.M., Kesler, S.E., Russell, N., Piñero, E., Sanchez C., R., Perez R., M., Moreira, J. and Borges, M., 2004, Age and tectonic setting of the Camagüey volcanic-intrusive arc, Cuba: Late Cretaceous extension and uplift in the western Caribbean: Journal of Geology, v. 112, p. 521-542.

Borges M, Zhang Y, Essene E., 2002, New calibrations of Garnet-Clinopyroxene thermobarometers.; Eos Trans. AGU, 83(47), Fall Meet. Suppl., Abstract V51B-1252.